Title

Quantitative Assessment of Myocardial Microstructural Remodeling Using Diffusion Tensor Magnetic Resonance Imaging

Author

Kung, Geoffrey

Publication Date

2013

Peer reviewed|Thesis/dissertation

UNIVERSITY OF CALIFORNIA

Los Angeles

Quantitative Assessment of Myocardial Microstructural Remodeling Using Diffusion Tensor Magnetic Resonance Imaging

A dissertation submitted in partial satisfaction of the

requirements for the degree Doctor of Philosophy

in Biomedical Engineering

by

Geoffrey Lloyd Kung

2013

ABSTRACT OF THE DISSERTATION

Quantitative Assessment of Myocardial

Microstructural Remodeling Using

Diffusion Tensor Magnetic Resonance Imaging

by

Geoffrey Lloyd Kung

Doctor of Philosophy in Biomedical Engineering

University of California, Los Angeles, 2013

Professor Daniel B. Ennis, Chair

The complex, but highly organized arrangement of myocytes within the left ventricle (LV) underlies the anisotropic mechanical and electrical function of the heart. Whole heart surveys of microstructural remodeling are critical to our basic science understanding of cardiac pathophysiology. Recently, diffusion tensor magnetic resonance imaging (DT-MRI) has emerged as a means for quantifying global and regional microstructural remodeling.

Previous observations of myocardial microstructure have predominantly relied on histological methods, which are tedious and difficult to spatially register in three-dimensions (3D). DT-MRI enables the 3D evaluation of whole heart microstructure. Each diffusion tensor can be decomposed into a system of eigenvectors and eigenvalues. The eigenvectors of the diffusion tensor contain the diffusion orientation information within the tissue microstructure and have established correspondence with the myofiber (primary eigenvector) and myolaminar sheet

orientations (secondary and tertiary eigenvectors). Meanwhile, the eigenvalues quantify the magnitude of diffusion along each eigenvector and characterize the overall shape of diffusion. DT invariants (e.g. trace, fractional anisotropy, or mode), which are functions of the eigenvalues alone, saliently characterize specific attributes of tensor shape and can be used to evaluate specific attributes of microstructural remodeling.

Chapter 1 of this dissertation provides an understanding of myocardial microstructure in health and disease. Chapter 2 provides an understanding of DT-MRI, and its capabilities in evaluating soft tissue microstructure. In Chapter 3 we used an ovine model to establish the correspondence between both the secondary and tertiary eigenvectors of the local diffusion tensor and the dual sheet orientations observed in local histology. In Chapter 4 we quantified microstructural remodeling in a porcine model of myocardial infarction and its border zone using DT-MRI and revealed that the border zone significantly remodeled compared to both infarct and remote myocardium, providing a unique microstructural environment. In Chapter 5 we revealed significant microstructural remodeling in a rabbit mode of pacing induced heart failure using DT-MRI within transmural regions as well as transmural heterogeneity of microstructure within both normal and heart failure myocardium. Chapters 6 and 7 describe the conclusions of this work and provide an outlook for continued research based on this work's achievements.

The dissertation of Geoffrey Lloyd Kung is approved.

Alan Garfinkel

William S. Klug

Benjamin M. Ellingson

Hrayr S. Karagueuzian

Daniel B. Ennis, Committee Chair

University of California, Los Angeles

2013

Dedication

This dissertation is dedicated to my loving and supportive family, Margaret, Shyang-Lai and Jimmy.

TABLE OF CONTENTS

ACKNOWLEDGEMENTS

This dissertation was funded in part by the American Heart Association Western States Affiliate Predoctoral Fellowship, the NIH, the Department of Biomedical Engineering, and the Department of Radiological Sciences.

I would like to thank my committee chair and advisor, Dr. Daniel B. Ennis, for his invaluable guidance during the PhD process. I would also like to thank the committee members for their generous contributions of time, guidance, and constructive criticism.

I would like to acknowledge my fellow lab members, the UCLA Department of Radiological Sciences and Department of Biomedical Engineering.

VITA

2005 BS Mechanical Engineering and Applied Mechanics, University of Pennsylvania, Philadelphia, PA

2009 MS Biomedical Engineering, University of California, Los Angeles, CA

PUBLICATIONS

Kung GL, Ouadah S, Hsieh YC, Gahm JK, Garfinkel A, Chen PS, Ennis DB. *Myocardial Microstructural Remodeling in Pacing Induced Heart Failure Measured by Diffusion Tensor MRI*. Journal of Magnetic Resonance Imaging. [In Submission].

Kung GL, Vaseghi M, Gahm JK, Shevtsov J, Garfinkel A, Shivkumar K, Ennis DB. *Microstructural Border Zone Remodeling in the Post-Infarct Porcine Heart Measured by Diffusion Tensor MRI and T1-Weighted Late Gadolinium Enhanced MRI*. Journal of Magnetic Resonance Imaging. [In Submission].

Gahm JK, **Kung GL**, Ennis DB. *Weighted component-based tensor distance applied to graph-based segmentation of cardiac DT-MRI*. Proc. International Symposium on Biomedical Imaging: From Nano to Macro (ISBI). 2013, San Francisco, CA, pp. 504-507.

Gahm JK, Wisniewski N, Kindlmann G, **Kung GL**, Klug WS, Garfinkel A, Ennis DB. Lin*ear invariant tensor interpolation applied to cardiac diffusion tensor MRI*. Medical Image Computing and Computer-Assisted Intervention (MICCAI) 2012, Part II. LNCS, vol. 7511, pp. 494–501.

Moriarty JM, **Kung GL**, Ramos Y, Moghaddam AN, Ennis DB, Finn JP. *Injection of gadolinium contrast through pediatric central venous catheters: a safety study*. Pediatric Radiology. 2012; 42(9): 1064-9.

Kung GL, Nguyen TC, Itoh A, Skare S, Ingels Jr. NB, Miller DC, Ennis DB. *The presence of two local myocardial sheet populations confirmed by diffusion tensor MRI and histological Validation.* Journal of Magnetic Resonance Imaging. 2011; 34: 1080-91.

PRESENTATIONS

Kung GL, Ouadah S, Hsieh YC, Garfinkel A, Chen PS, Ennis DB. *Transmural Heterogeneity of Myocardial Microstructure in Pacing Induced Heart Failure Measured by Diffusion Tensor MRI.* Society for Cardiovascular Magnetic Resonance, Annual Scientific Sessions. 2013, San Francisco, CA.

Kung GL, Ajijola OM, Tung R, Vaseghi M, Gahm JK, Zhou W, Mahajan A, Garfinkel A, Shivkumar K, Ennis DB. *Microstructural Remodeling in the Porcine Infarct Border Zone Measured by Diffusion Tensor and Late Gadolinium Enhancement MRI.* American Heart Association Scientific Sessions, Annual Meeting, 2012, Los Angeles, CA.

Kung GL, Hsieh YC, Gahm JK, Garfinkel A, Chen PS, Ennis DB. *Microstructural Remodeling in Pacing Induced Heart Failure Measured by Diffusion Tensor MRI.* Biomedical Engineering Society, Annual Meeting, 2012, Atlanta, GA.

Kung GL, Vaseghi M, Gahm JK, Shevtsov J, Garfinkel A, Shivkumar K, Ennis DB. *Microstructural Border Zone Remodling in the Post-infarct Porcine Heart Measured by Diffusion Tensor MRI and Late Gadolinium Enhancement MRI*. Cardiac Physiome Society, Annual Workshop. 2012, San Diego, CA.

Kung GL, Ajijola OM, Gahm JK, Ramirez RJ, Zhou W, Mahajan A, Garfinkel A, Shivkumar K, Ennis DB. *Microstructural Remodling in the Post-infarct Porcine Heart Measured by Diffusion Tensor MRI and T1-Weighted Late Gadolinium Enhancement MRI.* Society for Cardiovascular Magnetic Resonance, Annual Scientific Sessions. 2012, Orlando, FL.

Moriarty JM, **Kung GL**, Ramos Y, Moghaddam AN, Ennis DB, Finn JP. *Safety of Gd infusion via pediatric central venous catheters for CEMRA: a pressure-flow study using a clinical electronic injector*. Magnetic Resonance Angiography Working Group, Annual Workshop. 2011, Banff, Canada.

Kung GL, Nguyen TC, Itoh A, Skare S, Ingels Jr. NB, Miller DC, Ennis DB. *Diffusion Tensor MRI Mapping of Two Local Myocardial Sheet Orientations with Histological Validation.* Biomedical Engineering Society, Annual Meeting, 2010, Austin, TX.

CHAPTER 1

Myocardial Microstructure

Dissertation Motivation

Histology remains the gold standard in characterizing myocardial microstructure and can be used, for example, to measure myofiber angle, myolaminar sheet angle, myocyte size (length and diameter, and fibrosis levels (collagen volume fraction). However, these methods are hampered by their inability to survey entire hearts in a sufficiently registered manner and are inordinately time consuming to perform for whole hearts or populations of hearts. More recently, however, diffusion tensor magnetic resonance imaging (DT-MRI) methods have been developed, which enable the non-destructive evaluation of whole heart microstructure. DT-MRI methods quantify the self-diffusion tensor of water as water molecules undergo Brownian diffusion within the tissue microstructure. Edelman et al.[1] were one of the first groups to show early evidence of the use of diffusion weighted MRI for in vivo cardiac applications; however, the challenges of the in vivo environment (e.g. long acquisition times coupled with cardiac and respiratory motion) presents an obstacle to the progression of DT-MRI's use for in vivo cardiac microstructural assessment. Hence, substantially more cardiac DT-MRI work has been focused on the evaluation of microstructure in ex vivo preparations and these methods are the focus in this work too.

The diffusion tensor is estimated within each image voxel and contains information about the size, shape and orientation of diffusion. The diffusion tensor can be decomposed into an eigensystem of three eigenvectors and three eigenvalues. It has been shown that the diffusion eigenvectors can accurately map myofiber and myolaminar orientations[2-9]. Previously, however, no studies have mapped the dual local sheet orientations that are often seen in histology. In

Chapter 3 we define the correspondence between the two observed sheet populations in histology and the eigenvectors of the diffusion tensor. Being able to accurately map the dual local sheet orientations throughout the entire heart will enhance the understanding of the local mechanics of systolic wall thickening as well as the role of electrical conduction along sheet directions.

In addition to the eigenvectors, the eigenvalues also provide valuable insight to tissue microstructure. The eigenvalues of the diffusion tensor provide a basis for comparing components of tensor size and shape and we have established this as a tool for quantifying differences in regional microstructure[10]. The eigenvalues can be mathematically manipulated into DT invariants, which provide salient and independent measures that describe the overall shape of diffusion. Specifically, tensor trace measures mean diffusivity; fractional anisotropy (FA) measures the magnitude of the diffusive anisotropy; and tensor mode characterizes the type of anisotropy (linear, planar, or orthotropic) in the diffusion tensor.

DT-MRI methods provide unique information for quantifying microstructural remodeling of a diseased heart and these measures likely correlate well to histological measures. An increase in trace within microstructure likely results from a decrease in the barriers per unit volume that restrict diffusion, which could be a consequence of apoptosis, necrosis, myocyte hypertrophy, or myocyte lengthening, or changes in intracellular and extracellular composition, which are primary consequences of HF[11-13]. Such comparisons have already been made in the brain and demonstrated a correlation between an increase in trace with a decrease in cell density[14]. A decrease in FA within the microstructure likely result from two remodeling phenomena: 1) a decrease in cellularity and the replacement of myocytes with fibrosis, which is composed of a homogeneous and porous extracellular collagen network or; 2) an increase in myofiber disarray where disorganization of fiber orientation provides a more isotropic environment for the

diffusion of water. Fibrosis replacement is a well-known consequence of infarction and observations of fiber disarray in infarcted myocardium have previously been observed[15-17]. Finally, a decrease in mode within myocardial microstructure may also result from the increase in myofiber disarray as the diffusion of water shifts from more linearly anisotropic in normal myocardium to more planar anisotropic in remodeled myocardium. Conversely, an increase in mode may result from myolaminar sheet disorganization as diffusion shifts from planar anisotropic to linear anisotropic behavior in remodeled myocardium. These tools are used in Chapters 4 and 5 to evaluate microstructural remodeling in porcine infarcts and borderzone and in a model of pacing induced heart failure.

DT-MRI has a clear advantage in the characterization of myocardial microstructure that are otherwise unavailable via histology. Whole heart surveys of healthy microstructure and microstructural remodeling are critical to augmenting our basic science understanding of the consequences of cardiovascular disease (CVD) and are needed to seed advanced computational models of electrophysiology. Additionally, understanding the microstructural remodeling process can elucidate new approaches in the development of therapies to prevent or attenuate the progression of such diseases.

Global Myocardial Characteristics

The functional purpose of the heart is to pump blood throughout the body via the circulatory system. The human heart is comprised of four chambers: 1) the right atrium, which receives deoxygenated blood returning from the rest of the body; 2) the right ventricle, which receives blood from the right atrium and pumps the deoxygenated blood to the lungs; 3) the left atrium, which receives oxygenated blood back from the lungs; and 4) the left ventricle (LV), which

receives blood from the left atrium and pumps the oxygenated blood back to the rest of the body. Because the LV needs to pump blood to the entire body, it contains the most muscle mass out of all four chambers. Thus, the understanding of any electrical or mechanical function or dysfunction of the LV is critical and remains a paramount topic of continued research.

Microstructure of the LV and Function

The myocardium, which is the muscular tissue of the heart, is comprised of three main components: 1) myocytes, which are muscle cells and the main contractile unit in the heart; 2) the cardiac interstitium comprised of a collagenous scaffold, which provides the mechanical and architectural support for the myocardium; and 3) the vascular network, which provides the necessary blood and oxygen to the myocytes to perform work.

The human heart contains several billion myocytes, which provide the main mechanical and electrical mechanisms for contraction. Although myocytes only represent about one-third of the total number of cells in the myocardium, they represent 67-75% of the total myocardial volume[18, 19]. The myocytes themselves are long cylindrical structures with a length of approximately 100 μm and a diameter of 25 μm. The myocyte can be further broken down into its underlying contractile unit, the sarcomere. Hundreds of adjacent sarcomeres, each of which have a length of 2 μm and diameter of 1 μm, provide the overall structure of the myocyte and take up about 50-60% of the myocyte volume. The sarcomere is comprised of bundles of myofibrils, consisting of organized myosin and actin filaments aligned along the long axis of the myocyte. The contractions of the actin and myosin filaments and subsequent contractions of the sarcomeres provide the mechanism for the contraction of the entire myocyte. In addition to sarcomeres, the myocyte also contains primary organelles of nuclei, taking up 5% of the myocyte

volume, with the majority of myocytes being multi-nucleated; mitochondria, taking up 20-30% of the myocyte volume and providing the energy necessary for contraction; and the sarcoplasmic reticulum, which plays a role in the electrical activation necessary for contraction and takes up most of the remaining volume of the myocyte.

Myocytes are further organized in a complex and highly structured arrangement that optimize the efficiency of the mechanical and electrical function of the heart. Myocytes are aligned lengthwise to form so-called "myofibers" which are arranged in a transmural, helical pattern. Within the LV, the helical orientation of myofibers are arranged with myofibers arranged in a left-handed helical pitch at approximately -45° with respect to the local circumferential axis at the subepicardium, circumferentially oriented myofibers at the midwall, and myofibers arranged in a right-handed helical pitch at approximately +45° with respect to the local circumferential axis at subendocardium as depicted in Figure 1. This myofiber alignment facilitates electrical conductivity along the myocyte axis creating a highway of electrical propagation throughout the myocardium.

Figure 1: Depiction of the transmural helical pattern of myofibers in a formalin fixed porcine heart in an image taken by Anderson, et al[20]. Layers of the myocardium are removed at increasing depths traveling from the base of the heart to the apex to show the gradual change in myofiber orientation from the epicardium (shown at the basal level) to the endocardium (shown at the apical level).

The myofibers are further organized into two-to-four cell thick layers to form so-called myolaminar sheets[21]. The extracellular collagen matrix maintains the organization of myolaminar sheets with cleavage planes separating adjacent sheets and allowing for movement of adjacent sheets during contraction and relaxation. Recently, it has been shown that this myolaminar organization is the main mechanism for systolic wall thickening[22, 23]. The myocyte itself only increases in diameter by ~8% during contraction and thus cannot provide the upwards of 40% increase in LV wall thickness that is seen during systolic contraction[22, 24]. Thus, it is believed that interlaminar transverse shear of adjacent myolaminar sheets along their cleavage planes and sheet extension act as the main mechanisms of systolic wall thickening[21-24]. Furthermore, myolaminar orientation has recently been shown to yield a bimodal distribution of distinctly positive and negative values of sheet angles that cluster around a +45° range and a -45° range relative to the local cardiac coordinate system[2, 3, 8, 9, 25, 26]. This bimodal sheet structure facilitates "accordion-like" interlaminar transverse shear[25]. The myolaminar arrangement of myocytes may also play a role in the electrical behavior of the heart. Electrical conduction in the heart propagates anisotropically with the greatest conductance along the myofiber axis. However, while it was previously believed that electrical conductivity was isotropic in directions transverse to the myocyte axis, recently it has been shown that electrical conductance acts in an

orthotropic manner with the greatest propagation velocity in the myolaminar sheet direction and the slowest propogation in the sheet normal direction[27, 28].

The cardiac interstitium houses the extracellular matrix of the myocardium, which is primarily composed of a fibrillar collagen network serving as the connective tissue between myocytes. The interstitium also contains various cells, such as fibroblasts and plasma cells, as well as glycosaminoglycans and glycoproteins that play lesser roles like synthesizing collagen, facilitating substrate exchange between myocytes and capillaries, and serving as a defense mechanism against foreign substances.

The primary function of the extracellular collagen matrix is to act as the scaffolding for the organized structure of myocytes and to evenly distribute the forces experienced in the myocardium during contraction and relaxation. The collagen matrix consists of several components serving different structural functions. The epimysial collagen matrix envelops the entire myocardium on the outside borders of the epicardium and endocardium and serves as the outer skeleton for the myocardium. The perimysial collagen matrix extends from the epimysium and creates a highly branched network to form weaves of collagen fibers surrounding bundles of myofibers and also creates strands of collagen fibers connecting adjacent myofiber bundles. The weaves and strands of perimysial collagen maintain the myolaminar sheet structure of the heart and help prevent misalignment and provide the tensile strength for the myocardium to withstand the forces exerted during contraction and relaxation[29]. Finally, the endomysial collagen matrix consists of fibers surrounding individual myocytes and capillaries, thus maintaining the alignment of myocytes in myofibers. Endomysial collagen also consists of struts adjoining myocytes to one another and to adjacent capillaries in order to provide stiffness and help prevent slippage between adjacent myocytes and capillaries.

Cardiac Remodeling

Cardiac remodeling is a physiologic or pathologic condition that includes, but is not limited to, cellular and interstitial changes, which lead to changes in size, shape, and function of the heart[30]. The two most common cardiovascular diseases (CVD) which cause cardiac remodeling are heart failure, which affects 5.1 million Americans, and myocardial infarction (MI), which affects 7.6 million Americans[31], annually. While global changes as a consequence of cardiac remodeling, such as ventricular hypertrophy or LV chamber dilation, are well described, changes in myocardial microstructure at or near the cellular level are incompletely understood. In heart failure, the main components of microstructural remodeling include myocyte elongation, myocyte hypertrophy, and overall cell loss[11-13], all of which play a role in altering contractile function[30]. In MI, microstructural remodeling is characterized by myocyte hypertrophy remote from the infarct and replacement of viable myocytes with fibrotic scar tissue in and around the infarct zone leading to impaired contractile function and an increased incidence of arrhythmia due to altered electrophysiological pathways[32].

Structural Remodeling in Heart Failure

Heart failure (HF) is a leading cause of death in the United States affecting 5.1 million Americans in 2013 with a 50% mortality rate within 5 years of onset of HF[31]. HF can be triggered by various causes including myocardial infarction and other ischemic heart diseases, hypertension, valvular heart disease, and various cardiomyopathies. The causes of HF stem from damaged or hemodynamically overloaded myocardium leading to impaired contractile function and insufficient blood flow out of the LV. The impaired mechanical function as a result of

structural remodeling is also associated with an impairment of electrical function as HF can also lead to an increased incidence of arrhythmia[33, 34].

In heart failure, the left ventricular myocardium undergoes many forms of remodeling characterized by changes in size, shape, and function ranging from a global level to a microstructural and sub-cellular level. The stages of global LV remodeling are depicted in Figure 2. Initially, the LV will remodel from normal to the acute stage of HF with a slight increase in chamber diameter as the LV wall experiences increased stress due to elevated pressure or volume. As HF progresses, the LV reaches a chronic compensated stage, also known as compensatory hypertrophy, where the chamber diameter and wall thickness increase in unison resulting in increased LV mass in order to normalize the wall stresses during contraction stemming from the increased pressure demands. Finally, end stage HF results in a chronic de-compensated LV where chamber dilation continues with a decrease in wall thickness as wall stresses become overwhelming and often results in death.

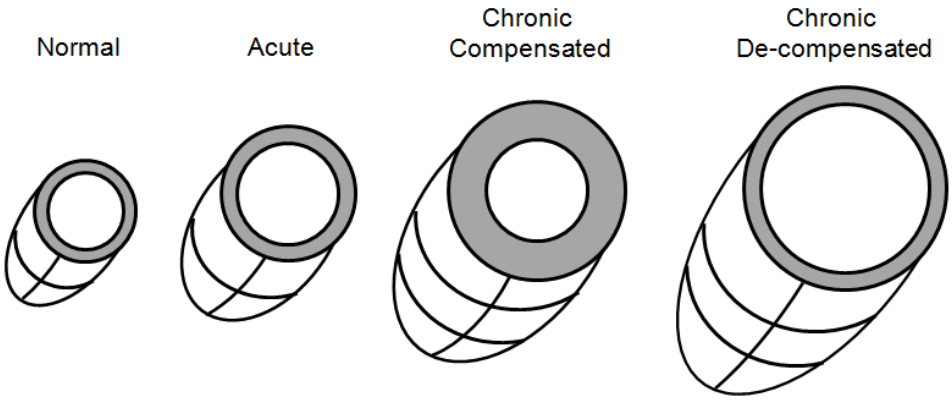

Figure 2: Stages of global left ventricular remodeling during heart failure.

On a microstructural level, HF can alter the complex organization of myocytes as well as the overall composition of myocardium, both of which contribute to the disruption of the mechanical

and electrical functions of the heart. On the cellular level, the progression of HF can cause premature myocyte death (necrosis) resulting in a loss of up to 40% of the heart's original myocytes[11]. Necrosis can be localized in cases such as MI or more diffuse in cases such as cardiomyopathy. Programmed myocyte death (apoptosis) has also been observed in HF while not occurring under normal conditions[35]. The myocyte itself also remodels by increasing in length and radius (hypertrophy) as depicted in Figure 3. It has been reported that HF leads to a 33% increase in length and an 11% increase in myocyte diameter, leading to an increase in myocyte length-to-diameter ratio[11, 12, 36]. In addition, the myocytes undergo intracellular remodeling characterized by increases in the number of myofibrils and mitochondria as well as enlargement of the mitochondria and nuclei in early stages of HF[37]. As HF progresses to later stages, the enlarged organelles lead to myofibril displacement and abnormal Z-band patterns, which lead to the disruption of sarcomere organization and increased tortuosity of T tubules[37].

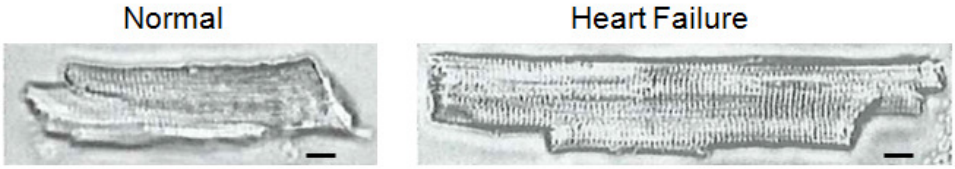

Figure 3: Myocyte remodeling during heart failure as depicted from images taken by Anand, et al[38]. Both the myocyte length (33% increase) and cross-sectional area (23% increase) grow as a consequence of heart failure[11]. Scale bar indicates 10 μm.

Myocyte loss and remodeling is accompanied by remodeling of the extracellular matrix. Depletion of collagen struts has been reported in cases of systolic failure, which has been shown to degrade myocyte alignment and causing "slippage" of adjacent myocytes which may play a role in the de-compensated dilation in HF[39]. The deterioration of collagen struts may also trigger myofiber disarray, which is characterized by the disorganization of myofiber alignment[17].

Alternatively, HF increases the quantity of interstitial collagen, which contributes to fibrosis replacement of viable myocytes. Overall collagen volume fraction levels in the heart have been observed to increase from 3-5% in the normal heart to 8% in HF studies using a volume overloading rapid pacing model of HF[11, 40, 41]. Pressure overloading models of HF have seen higher increases to levels above 15-20% in CVF[18]. The increase in collagen can be seen in histological samples of Masson's trichrome stained myocardium from both normal and pacing induced HF myocardium from a canine model depicted in Figure 4, with viable myocytes stained in red and collagen representing fibrosis stained in blue[41]. Although studies have reported observations of distinct microstructural remodeling on a cellular and interstitial level in human and animal models, conflicting reports are still prominent and the mechanisms and exact characterization of microstructural remodeling in HF is still not completely understood.

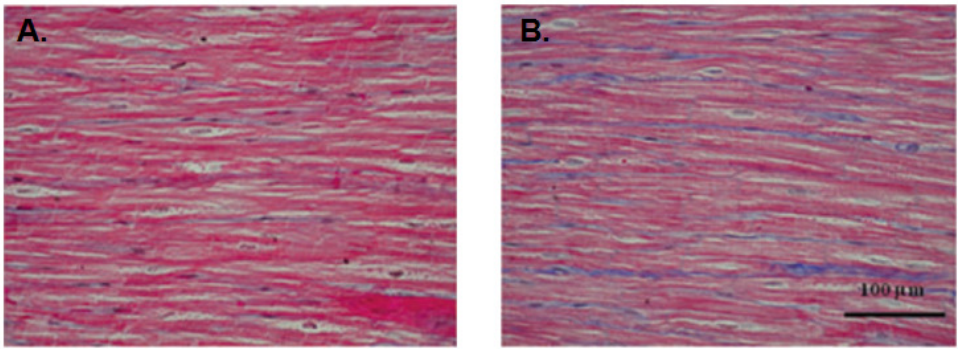

Figure 4: Histological samples of Masson's trichrome stained (A) normal myocardium and (B) HF myocardium as depicted in images taken by Lin, et al[41]. Viable myocytes are stained in red with collagen stained in blue.

Structural Remodeling in Myocardial Infarction

Myocardial infarction (MI) is a leading cause of death in the United States affecting 7.6 million Americans as of 2013 with a 15% mortality rate on every incidence[31]. MI is caused by a

restriction of blood supply (ischemia) to a part of the myocardium and with the subsequent lack of sufficient oxygen, the ischemic part of the muscle can become damaged or die altogether. Myocardial infarction impairs the regional mechanical and electrical function of the heart leading to the deterioration of contractile function.

Myocardial infarction, like heart failure, causes LV myocardium to remodel on a global and microstructural level. Due to loss of muscle mass, wall thinning and ventricular dilatation can occur locally around the infarct region. As a result, hypertrophy can subsequently occur in areas remote from the infarct due to the increased wall stress and loading requirements in the non-infarcted areas. If MI ultimately leads to HF, then the LV may follow the similar progression of global remodeling from acute, to compensated, to de-compensated stages.

On a microstructural level, MI is most notably characterized by myocyte necrosis in the ischemic region leading to fibrosis replacement via collagen scar formation. The scarred region also disrupts the myofiber organization leading to fiber disarray[15, 42]. The collagen scar can be dense in the ischemic region blocking electrical conduction in the infarct zone and re-routing conduction to pathways around the infarct. On the other hand, collagen scar formation can also be patchy with pockets of viable myocytes existing throughout the infarct. Figure 5 depicts short axis late gadolinium enhanced magnetic resonance images of ex vivo porcine hearts exhibiting dense (Figure 5A) and patchy (Figure 5B) infarcts, where the collagen scar associated with the infarct region is highlighted by the enhanced signal intensity in the myocardium due to gadolinium concentrating within the scar. In particular, it is thought that this patchy type of scar formation can create tortuous pathways of viable myocardium in the infarct region, facilitating slow electrical conduction or reentry phenomena, which can trigger fatal arrhythmias[43-45].

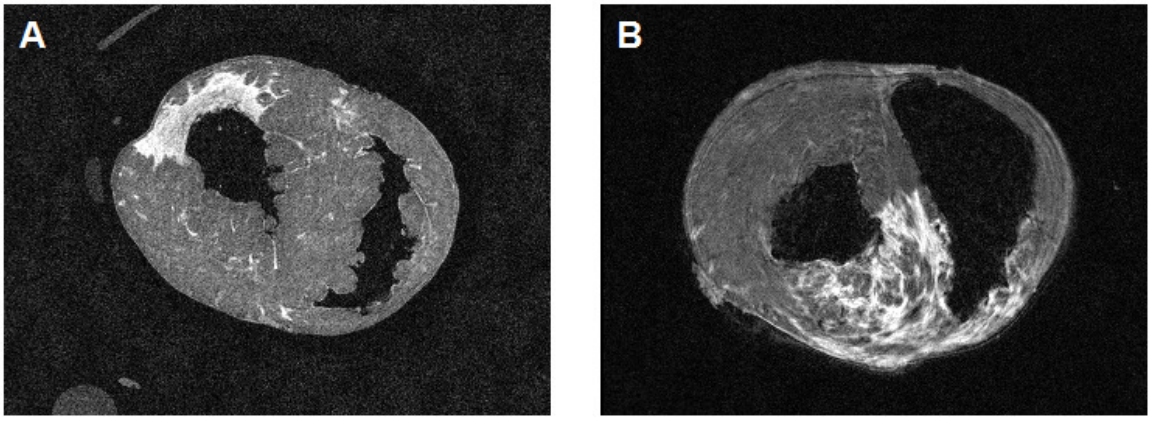

Figure 5: Late gadolinium enhanced short axis MRI slices of ex vivo porcine hearts exhibiting (A) dense and (B) patchy scar regions.

In addition to the remodeling that occurs within the infarct scar region, myocardium within the infarct border zone and myocardium remote from the infarct has been known to remodel as well. The border zone encompasses the myocardium surrounding the well-defined scar region and is characterized by a mix of viable myocytes and smaller strings of fibrosis. If infarcted myocardium becomes reperfused, myocytes within the infarct border zone have been observed to swell and become edematous as the intracellular osmolarity increases during reperfusion[46]. Microvascular obstruction can also result in reperfused tissue due to increased volume of endothelial cells in combination with edematous myocytes leading to occlusion of the capillary lumen[47]. This phenomenon may result in a decrease in overall myocardial capillary density and luminal surface area that has been observed as a consequence of MI[48]. Myocyte lengthening and hypertrophy has also been observed in the border zone and myocardium remote from the infarct in order to compensate for the weakened contractility due to the loss of muscle mass in the infarct region[48]. However, remote myocardium is not known to experience any changes in collagen volume fraction[49].

CHAPTER 2

Introduction to Diffusion Tensor Magnetic Resonance Imaging

Introduction to Magnetic Resonance Imaging

Magnetic Resonance Imaging (MRI) is a medical imaging technique used to generate images of internal structures of the body. MRI is known for its exceptional ability to provide soft tissue contrast, especially in the brain, liver, lungs, and heart. The fundamental process of MRI consists of the application of a strong magnetic field onto an object to manipulate the magnetic moment of hydrogen protons within that object to create an MR signal. The magnetic moment of hydrogen protons originates from the spin and charge of the hydrogen nuclei which creates detectable magnetic moment.

The acquisition of an MR image is briefly described herein and involves: 1) the presence of an equilibrium state of magnetic spins; 2) the disruption of these magnetic spins by an external force; 3) the detection of the signal generated by the disrupted spins relaxing back into their equilibrium state; and 4) the reconstruction of the detected signal to form an image. In the presence of an external magnetic field of an MRI scanner, hydrogen protons, or magnetic spins, align with the direction of the external magnetic field. To generate an MR signal, these spins are excited using a radio frequency pulse to disrupt the spins' equilibrium state. The MR signal is then detected in the time domain and spatially localized by the use of magnetic field gradients. Through the use of low pass filtering and phase sensitive detection, the signal detection can be converted from the time domain to the spatial frequency domain. The inverse Fourier transform then converts the signal from the spatial frequency domain to the image domain to generate the MR image.

Diffusion Weighted Magnetic Resonance Imaging

Diffusion based magnetic resonance imaging techniques rely on the measurement of the signal attenuation in an MRI experiment resulting from excited spins undergoing random translational (Brownian) motion within the imaging volume. In biological tissues, the excited spins are hydrogen protons from water molecules as the human body is composed of 70% water. The measurement of diffusion of other metabolites besides water can be achieved using MR spectroscopy; however such methods are outside the scope of this thesis. In freely diffusing water, the movement of water molecules is perfectly random and only agitated by thermal energy. In biological tissues, water molecules interact with many microstructural tissue components such as cell membranes, intracellular organelles, and components of the extracellular matrix, thus the diffusion of water is restricted. Within a typical imaging voxel (ranging from sub mm^3 to several mm^3), the signal attenuation due to diffusion reflects the displacement distribution of water molecules and can provide insight to the geometric organization of microstructure. Without the presence of bulk flow, water molecules will typically travel on the order of 5-15 μm in ~1 second within biological tissue microstructure under typical diffusion MRI experimental parameters[50]. It is important to note that bulk fluid flow, most commonly blood flow, can corrupt diffusion based MRI experiments under typical conditions as the MRI signal cannot differentiate the movement of spins due to diffusion from the movement of spins due to bulk flow.

In diffusion weighted MRI (DWI), molecular diffusion attenuates the MRI signal at a given imaging voxel such that as the rate of diffusion increases, the signal intensity of the imaging

voxel decreases. Stejskal and Tanner derived the equation to solve for the diffusion coefficient of water within an imaging voxel based off the MRI signal attenuation, which is shown here[51]:

$$S = S_0 e^{-bD} \quad (1)$$

Where S is the diffusion weighted signal generated by playing a diffusion gradient pulse, S_0 is the non-diffusion weighted signal generated by a similar MR experiment without a diffusion gradient pulse, b is the b-value which is a scalar that describes the amount of diffusion weighting dependent on the shape and spacing of the diffusion gradient pulse, and D is the estimated diffusion coefficient of the imaging voxel. The D from Eqn. 1 is also synonymous with the apparent diffusion coefficient (ADC) of the imaging voxel representing the bulk mean diffusivity and ADC will be used in lieu of D from here on. The b-value is dependent upon the parameters of the diffusion gradient that is played in the DWI experiment. With perfectly rectangular diffusion gradient pulses, the b-value is defined by:

$$b = \gamma^2 G^2 \delta^2 (\Delta - \frac{\delta}{3}) \quad (2)$$

Where γ is the gyromagnetic ratio, G is the diffusion gradient amplitude, δ is diffusion gradient duration, and Δ is the diffusion gradient separation time. The parameters of a DWI experiment can be more easily understood from the DWI pulse sequence. The typical DWI experiment utilizes a pulsed-gradient spin echo sequence as depicted below in Figure 1:

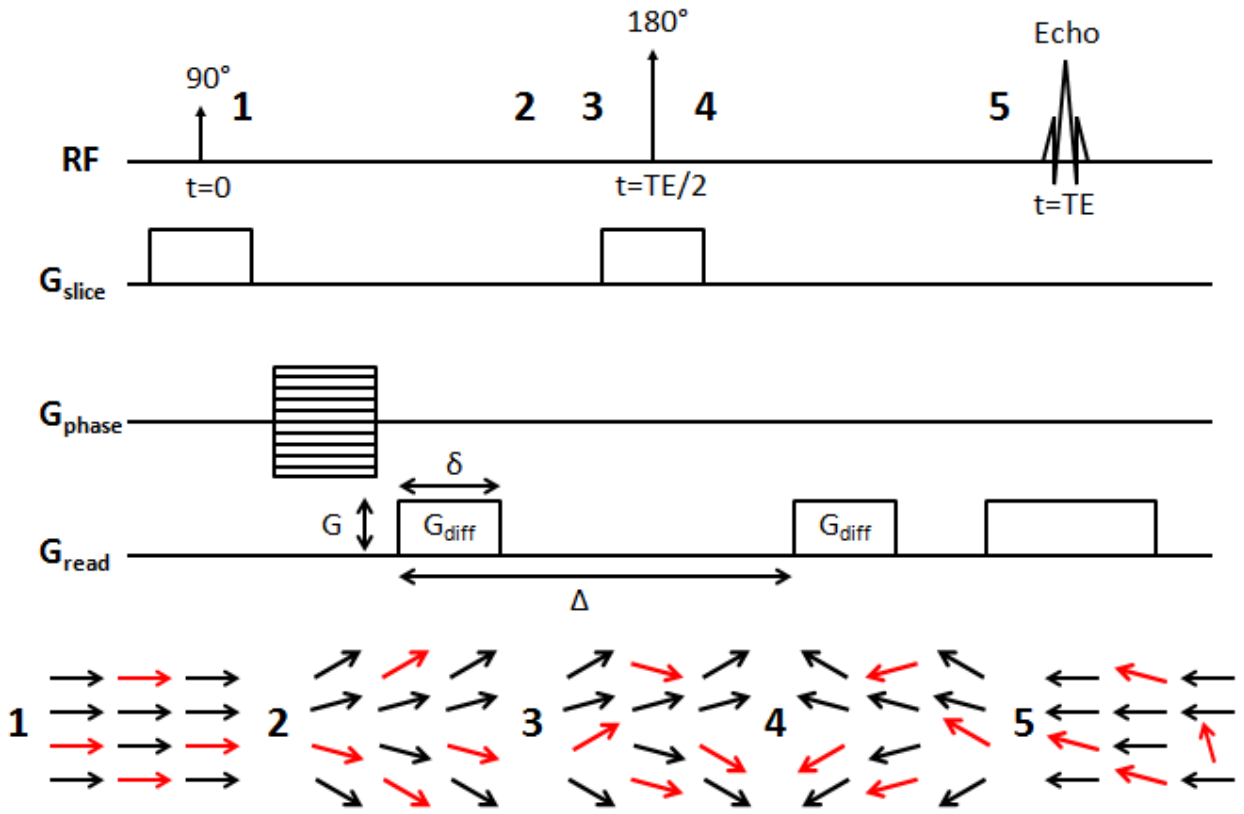

Figure 1: Pulsed-gradient spin echo sequence used in DWI. Two diffusion gradient pulses are played on either side of the 180° refocusing pulse along the readout gradient direction in order to introduce a net phase shift. The diffusion gradient pulses can be played along any combination of the three gradient directions. An example of stationary (black arrows) and diffusing (red arrows) spins within an imaging voxel is shown at different points of the pulse sequence. RF = radiofrequency pulse, G_{slice} = slice-select gradient, G_{phase} = phase-encoding gradient, G_{read} = readout gradient, G_{diff} = diffusion gradient pulse, t = acquisition time, TE = echo time, G = diffusion gradient amplitude, δ = diffusion gradient duration, Δ = diffusion gradient separation time.

This sequence is identical to a classic spin echo MR sequence but has two additional gradient pulses, labeled G_{diff}, which are played on opposite sides of the 180° refocusing RF pulse. Note

that although these diffusion gradient pulses are shown on the G_{read} axis, they can be played using any combination of the slice select, phase, or readout directions. An example of the evolution of excited spins within an imaging voxel is also depicted below the pulse sequence. At position (1) excited spins (labeled as black and red arrows) are rotated onto the transverse plane from the initial 90° excitation pulse. The spins then experience a phase shift as a consequence of the first diffusion gradient pulse played at position (2). Due to diffusion, the spins in red are spatially mixed from their original position as time is allowed to pass, whereas the spins in black may remain stationary as shown in position due to a physical barrier in this theoretical depiction (3). The 180° refocusing pulse is then applied, reversing the phase shift from the first diffusion gradient pulse as shown in position (4). A second diffusion gradient pulse is played after the refocusing pulse to phase shift stationary spins back to their original positions from position (1). However, spins that have been displaced by diffusion will experience a net phase shift that results in an attenuation of the MR signal as seen in position (5). As displacement of spins due to diffusion increases, the net phase dispersion will also increase, thus lowering the signal intensity of the imaging voxel of interest.

In order to calculate the ADC, another spin echo MR experiment with identical parameters as the DWI sequence needs to be performed, but without the diffusion gradient pulses. Without the phase shift from the diffusion gradients, the signal attenuation due to diffused spins will be greatly mitigated, and the signal intensity will be stronger than the intensity measured from the DWI sequence and depend upon the conventional spin echo contrast. Thus, ADC is solved by measuring the signal intensity from the diffusion weighted experiment (S), the signal intensity from the non-diffusion weighted experiment (S_0), and the known b-value. ADC measurements have been used mainly in applications of diagnosing diseases in the brain. Specifically, changes

in ADC have been used as an early indicator of acute ischemic stroke[52], characterizing various types of white matter edema[53], and determining the severity of brain tumors[54, 55].

Diffusion Tensor Magnetic Resonance Imaging

DWI can only provide information on the bulk mean diffusivity within an imaging voxel along the direction of the applied diffusion gradient and provides no information about orientation of diffusion or characterization of the microstructural architecture. This may be sufficient in homogeneous tissues like the liver, where diffusion is isotropic (insensitive to spatial direction), or diseases in the brain affecting overall diffusivity; however in more complex structures like the white matter in the brain or myocardium, fiber architecture and other complex geometries create a more anisotropic environment for diffusion. Thus, diffusion tensor MRI (DT-MRI) techniques have evolved to account for more heterogeneous biological tissues. In a DWI experiment, diffusion is described using a scalar representing the apparent diffusion coefficient. In DT-MRI, diffusion is instead described by a diffusion tensor, **D**, which represents a symmetric positive-definite 3x3 matrix containing 6 unique elements and fully describes diffusion along three dimensional axes and the correlation between the three dimensions[56]:

$$\boldsymbol{D} = \begin{bmatrix} D_{xx} & D_{xy} & D_{xz} \\ D_{yx} & D_{yy} & D_{yz} \\ D_{yz} & D_{zy} & D_{zz} \end{bmatrix} \tag{3}$$

A DT-MRI experiment requires at least seven separate experiments to provide enough information to estimate the six unique elements of the diffusion tensor: at least six diffusion weighted experiments with distinct non-collinear and non-coplanar diffusion gradient directions and at least one non-diffusion weighted experiment. The DT-MRI pulse sequence is identical to a DWI experiment shown in Figure 1, but with additional diffusion gradient pulses played along

distinct directions. In order to achieve ≥ 6 non-collinear, non-coplanar diffusion gradient directions, the diffusion gradient pulses must be played simultaneously with varying magnitudes on multiple gradient axes as playing the pulses on a single axis can only provide three distinct diffusion gradient directions. Because of the greater number of experiments involved in DT-MRI, the scan times for such studies can be prohibitively long – on the order of minutes to hours depending on the resolution and number of diffusion gradient directions. Thus, DT-MRI is primarily used to study the brain, where motion is typically minimal, or on ex vivo tissues.

In order to solve for the six unique elements of the diffusion tensor, Eqn. 1 is modified to incorporate the diffusion tensor and each of the unique diffusion gradient directions:

$$S_j = S_0 e^{-b_j \vec{g}_j \cdot \boldsymbol{D} \vec{g}_j} \tag{4}$$

Where S_j and b_j represent the attenuated signal and b-value for the j^{th} experiment and $\vec{g}_j$ represents the directional diffusion gradient encoding unit vector for the j^{th} experiment. The term $\vec{g}_j \cdot \boldsymbol{D} \vec{g}_j$ represents the projection of diffusion tensor along the direction defined by $\vec{g}_j$. Eqn. 4 can be written as a system of linear equations in order to solve for the six unknowns of the diffusion tensor via linear or non-linear regression.

More than six unique diffusion directions and one non-diffusion weighted experiment are commonly acquired to over-determine and improve accuracy of the diffusion tensor. As the number of unique diffusion gradient directions increases, the amount of sampling direction bias decreases as three-dimensional space becomes more uniformly sampled. Additionally, as the number of non-diffusion weighted experiments increases, the more accurate the S_0 will be as non-diffusion weighted signal averaging will reduce the effects of random noise. There are many approaches in optimizing the diffusion gradient scheme for six or greater directions. Jones, et al. described a minimum electrostatic force requirement of pairs of charges placed on

the surface of a unit sphere such that the diffusion gradient directions are defined by the vectors intersecting the center of the sphere between charged pairs[57]. Similar to a minimum force requirement, minimum Coulombic energy requirements between the total interactions of charges on a unit sphere have also been implemented in diffusion gradient schemes[58]. Additionally, gradient directions defined by tessellation of regular polyhedral have been used to optimize diffusion gradient schemes with examples depicted in Figure 2[58].

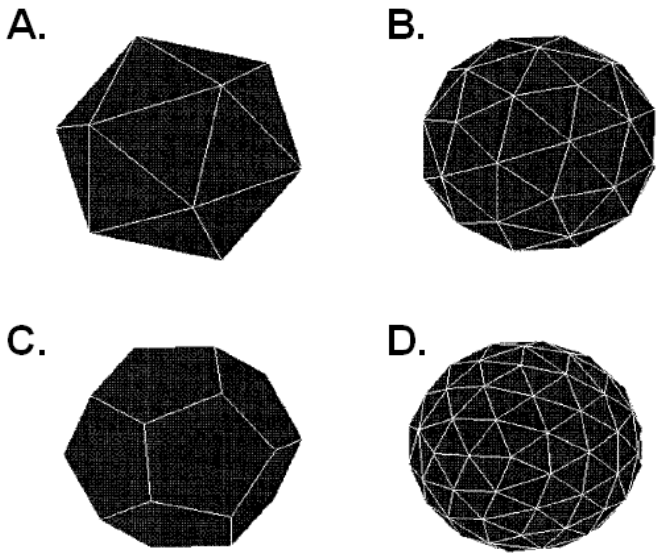

Figure 2: Diffusion gradient schemes governed by regular polyhedral with increasing number of diffusion gradient directions from A through D defined by intersecting vertices with the center of the polyhedral.

Eigensystem of the Diffusion Tensor

It is difficult to qualitatively and quantitatively extract local diffusion information from the diffusion tensor in its tensor form. However, the diffusion tensor can be decomposed into its

eigensystem from which scalar and vector information can be easily extracted. The eigensystem of the diffusion tensor is defined by:

$$\boldsymbol{DE_i} = \boldsymbol{\lambda_i E_i} \ (i = 1, 2, \text{or } 3) \tag{5}$$

Where E_i and λ_i represent the eigenvectors and eigenvalues of the diffusion tensor respectively. The eigenvectors describe the three principle axes of diffusion and eigenvalues describe the magnitude of diffusion in the three eigenvector directions. The diffusion eigensystem can be visualized as an ellipsoid as depicted in Figure 3, with the eigenvectors and eigenvalues being associated with the three primary axes of the ellipsoid[59, 60]. This ellipsoid representation compactly describes the orientation and shape information of local diffusion.

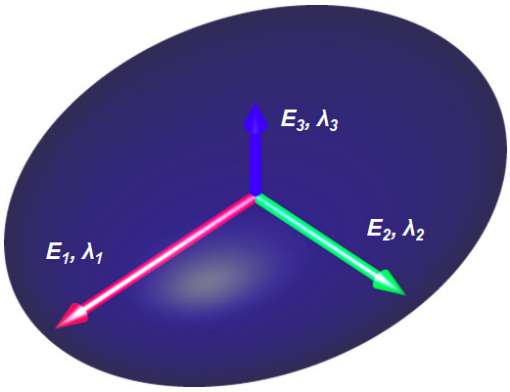

Figure 3: Representation of the diffusion eigensystem as an ellipsoid with E_1 and λ_1 representing the orientation and length of the primary axis of diffusion; E_2 and λ_2 representing the orientation and length of the secondary axis of diffusion; and E_3 and λ_3 representing the orientation and length of the tertiary axis of diffusion.

The eigenvectors of the diffusion tensor have been shown to accurately map orientation information of microstructural architecture. It has been well documented that the diffusion tensor's primary eigenvector aligns with axonal fiber-tracts within the brain and can be used to

perform tractography and connectivity to map the fiber trajectories[61-64]. In the myocardium, the diffusion eigenvectors have been shown to coincide with local myofiber and myolaminar orientations, with the primary eigenvector aligning with the myofiber direction, the secondary eigenvector aligning with the myolaminar sheet cross-fiber direction, and the tertiary eigenvector aligning with the sheet normal direction[2-8]. While the eigenvectors contain the orientation information of local diffusion, the eigenvalues contain the shape and size information of local diffusion and provide a basis for quantifying differences in local microstructure.

Diffusion Tensor Invariants

The eigenvalues of the diffusion tensor can be mathematically manipulated into diffusion tensor invariants to more succinctly describe the size and shape characteristics of local diffusion and provide information about the composition of local microstructure. Invariants are scalars calculated from the diffusion tensor and are particularly useful because they are independent of the tensor's coordinate system. The three eigenvalues provide three degrees of freedom to define the aspects tensor size and shape, thus three tensor invariants are needed to quantify the complete tensor shape. The three tensor invariants that are the most useful in characterizing the myocardium are tensor trace, fractional anisotropy, and tensor mode.

Tensor trace describes the overall diffusion tensor magnitude and is also proportional to the apparent diffusion coefficient (ADC) or bulk mean diffusivity and it is defined by the sum of the diffusion tensor eigenvalues:

$$Trace = \lambda_1 + \lambda_2 + \lambda_3 \quad (6)$$

Trace is measured in units of diffusivity and relates to the overall size of the diffusion profile, with a lower trace resulting in a smaller profile and slower diffusion due to diffusive barriers. A

higher trace results in a larger diffusive profile as water is diffusing rapidly with fewer barriers to diffusion. While trace provides the size information of local diffusion, it provides no specific shape information.

The fractional anisotropy (FA) of the diffusion tensor quantifies the degree of anisotropy or directional dependence within local diffusion. The FA is related to the ratio of the diffusion tensor's eigenvalues as such:

$$FA = \sqrt{\frac{\frac{3}{2}\left[(\lambda_1-\bar{\lambda})^2+(\lambda_2-\bar{\lambda})^2+(\lambda_3-\bar{\lambda})\right]}{\lambda_1{}^2+\lambda_2{}^2+\lambda_3{}^2}} \tag{7}$$

$$\bar{\lambda} = \frac{\lambda_1+\lambda_2+\lambda_3}{3} \tag{8}$$

FA is a unit-less measure and ranges in value from 0 to 1. If all of the eigenvalues are equal in magnitude then FA will equate to 0 representing completely isotropic diffusion, or equally distributed diffusion in all directions and a spherical diffusion profile. If one or two of the eigenvalues are significantly larger than the other(s), then FA will approach a value of 1 representing diffusion profile that is highly directionally dependent.

The tensor mode quantifies the type of diffusion anisotropy. Mode is also related to the ratio of the eigenvalues and is calculated as such:

$$Mode = \frac{\lambda_1\lambda_2\lambda_3}{norm(\widetilde{\boldsymbol{D}})^3} \tag{9}$$

$$\widetilde{\boldsymbol{D}} = \boldsymbol{D} - \frac{1}{3}trace(\boldsymbol{D})\boldsymbol{I} \tag{10}$$

$$norm(\widetilde{\boldsymbol{D}}) = \sqrt{trace(\widetilde{\boldsymbol{D}}\widetilde{\boldsymbol{D}}^T)} \tag{11}$$

Mode is also unit-less and ranges in value from -1 to 1. If the primary eigenvalue is large and secondary and tertiary eigenvalues are equally small, mode will approach 1 representing linear-anisotropy with a rod-like diffusion profile. If the primary and secondary eigenvalues are equal in magnitude with a significantly smaller tertiary eigenvalue, mode will approach -1 representing planar-anisotropy with a disc or pancake-like diffusion profile. Finally, if all three eigenvalues are equally spaced apart in magnitude, the mode will be zero representing orthotropic anisotropy with a book-like diffusion profile.

Diffusion Tensor Visualization

The visualization of the diffusion profiles can be aided by the use of glyphs, which are three dimensional surfaces that describe the diffusion tensor shape. Diffusion ellipsoids are a class of these so-called glyphs, however, they are restricted in the amount of detail they can provide due to shading ambiguity and lack of features. For example, ellipsoids lack the degrees of freedom to accurately and uniquely represent the planar-anisotropic, linear-anisotropic, and orthotropic diffusion profiles described by varying tensor modes. Recently, superquadric glyphs have come to the forefront in the visualization of the diffusion tensor, specifically in myocardium[65, 66]. Superquadric glyphs utilize distinct edge rendering defined by the superquadric shape function, accounting for the degree and type of anisotropy from a diffusion tensor[66].

Just like ellipsoids, the eigenvectors of the diffusion tensor determine the orientation of superquadric glyphs and the eigenvalues determine the size and shape of the glyphs. Furthermore, diffusion tensor invariants can also fully define the shape (via FA and mode) and size (via trace) of superquadric glyphs. Because FA describes the degree of anisotropy and mode describes the type of anisotropy, it is more practical to visualize the shape of the diffusion profile

with superquadric glyphs using both FA and mode together as depicted in Figure 4A. Meanwhile, tensor trace simply defines the size of the superquadric glyph as depicted in Figure 4B.

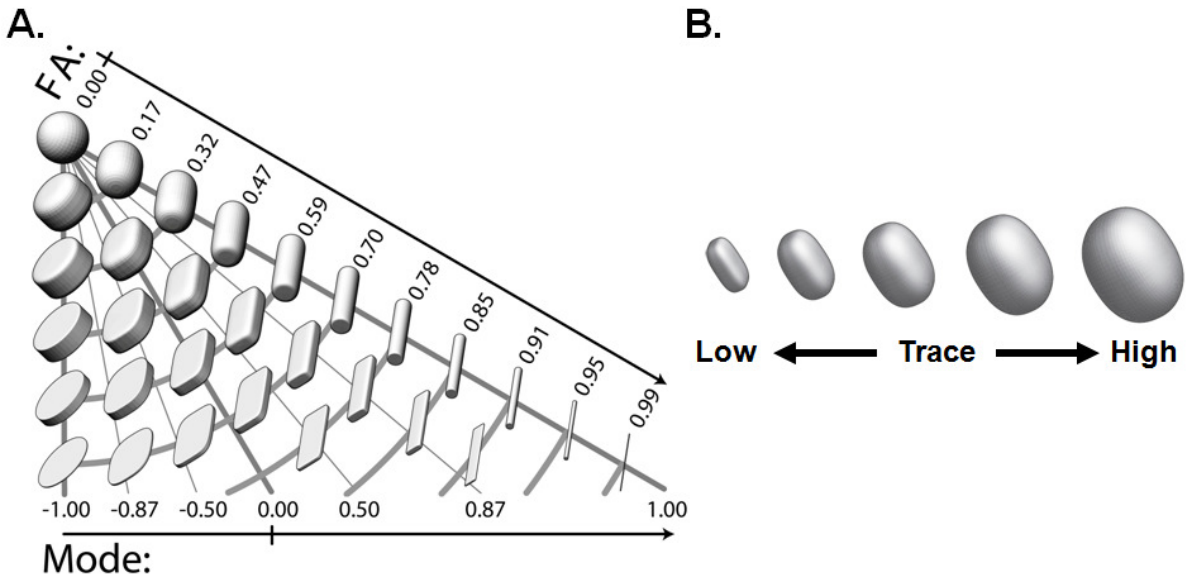

Figure 4: The space of diffusion tensor shape spanned by (A) FA, mode, and (B) trace rendered with superquadric glyphs.

Due to the enhanced edge features, superquadric glyphs provide much better visualization of diffusion profiles in unique microstructural features such as fibers (linear anisotropy – high FA, high mode) and myolaminar sheets (orthotropic anisotropy – mode near zero). Thus, superquadric glyphs provide greater distinction among spatially varying tensor data as well as greater distinction when comparing different groups of specimens.

Dissertation Objectives

The ***overall objectives*** of this dissertation are to: 1) Establish the correspondence between histological estimates of the dual local myolaminar sheet orientations and the 2nd and 3rd

eigenvector directions from DT-MRI for the first time; and 2) Use LGE based segmentations with registered DT-MRI to quantify microstructural remodeling in within myocardial infarcts and the surrounding border zone for the first time; and 3) quantify microstructural remodeling in heart failure using DT-MRI for the first time. The objectives are more cogently described by the following specific aims, which correspond to Chapters 3, 4, and 5, respectively:

Specific Aim #1: ***Define the correlation between DT-MRI and histologic estimates of myofiber and myolaminar sheet orientation.*** Recently, biomechanical studies[26] and histological examination[25, 29, 67] have suggested the existence of two orthogonal sheet populations within myocardial microstructure. We ***hypothesize*** that the secondary and tertiary eigenvector DT estimates of the local sheet orientations correspond with each of the two local myolaminar sheet orientations measured with histology.

Specific Aim #2: ***Quantify infarct and border zone microstructural remodeling with DT-MRI in a porcine model of ischemic heart disease.*** Myocardial infarction is currently diagnosed in 7.6 million people in the United States[68]. Late gadolinium enhanced (LGE) MRI is recognized as the gold standard for MRI based myocardial infarct mapping [69-71]. However, it is unclear if variations in LGE signal intensity correspond to microstructural remodeling. We used high resolution *ex vivo* LGE MRI of post-infarct porcine hearts to identify remote, infarct, and infarct border zone (BZ) regions of myocardium and to quantify microstructural remodeling in the BZ and infarct regions using DT-MRI. We ***hypothesize*** that the tensor trace will significantly increase and FA and mode will significantly decrease within BZ and show larger changes within infarct relative to remote myocardium.

Although previous studies have studied microstructural remodeling in post-infarct myocardium using DT-MRI[15, 16, 72-74], methods of infarct and border zone segmentation have

only used visual inspection to grossly divide radial segments into infarct, border, or remote regions within short-axis T2-weighted (non-diffusion weighted) images from the DT-MRI experiment. The results reported herein are the first to use LGE MRI to create accurate segmentations of infarct and BZ on a voxel by voxel basis in order to quantify microstructural remodeling using registered DT-MRI.

Specific Aim #3: ***Quantify global and regional microstructural remodeling with DT-MRI and histology in an animal model of heart failure.*** Heart failure (HF) currently affects 5.1 million people in the United States[68]. No DT-MRI studies, however, have examined microstructural remodeling in HF. Volume overloading via rapid pacing is one of the most commonly used animal models of HF in research studies due to its ease of implementation. Previous histological studies of pacing induced HF have observed little change in fibrosis replacement (8% in HF vs. 5% in normal)[75] of myocardium, but significant increases in myocyte length (33%) and cross sectional area (23%)[11-13] as well as transmural gradients of increasing myocyte size from epicardium to endocardium[76, 77].

Although, tensor invariants provide insight to the tissue's microstructural remodeling and have been validated as biomarkers for cell density in the brain and fibrosis replacement in the heart, more detailed implications of microstructural remodeling in myocardium have scantly been studied. Additionally, the classic Stejskal-Tanner equation of the diffusion weighted signal is limited in its assumption of a single compartment of diffusion within each imaging voxel. However, myocardial tissue has two main compartments of diffusion: the intracellular space and extracellular space. We sought to gain additional insight to the observed changes in the diffusion weighted signal by employing previous diffusion based MRI studies, which defined mathematical two-compartment models of restricted diffusion[78, 79]. Specifically, the Kärger

model[79] mathematically describes two-compartment diffusion for long cylinders packed in space to mimic intracellular and extracellular diffusion in living tissue, and provides insight to specific microstructural properties such as cell size, membrane permeability, cellular volume fraction, and intra- and extracellular diffusivity[80-82] and their contribution to altering the observed diffusion weighted signal.

The objectives of this aim were: 1) to quantify transmural-specific microstructural remodeling in pacing induced, chronic compensated HF using DT-MRI; 2) to quantify microstructural differences across transmural regions within normal myocardium and within chronic compensated HF myocardium using DT-MRI; and 3) to use the Kärger model of two-compartment diffusion to implicate a specific form of microstructural remodeling in chronic compensated HF that is consistent with the measured diffusion tensor data. Using a rabbit model of pacing-induced HF we ***hypothesize*** that left ventricular myocardial microstructure will remodel in a transmural specific fashion as evident by changes in DT invariants (trace, FA, and mode) when compared to normal myocardium. We also ***hypothesize*** alterations in transmural gradients of microstructural characteristics in HF myocardium when compared to normal myocardium.

CHAPTER 3

The Presence of Two Local Myocardial Sheet Populations Confirmed by Diffusion Tensor MRI and Histological Validation[1]

INTRODUCTION

The complex, but highly organized arrangement of myocytes within the left ventricle (LV) underlies the anisotropic mechanical[21-23, 83] and electrical[27, 28] function of the heart. Myocytes form so called "myofibers" and are arranged in a transmural helical pattern. Myocyte organization is further characterized by a lengthwise branching network and two-to-four cell thick layers, which form myolaminar sheets within an extracellular collagen matrix[21, 22, 25].

Previous observations of the sheet structure have primarily relied on histological methods such as electron microscopy[21, 22], confocal microscopy[29, 67], or optical microscopy[25, 26]. Such methods for quantifying both myofiber and myolaminar geometry are exceedingly tedious, especially for whole heart surveys[21] and don't lend themselves to spatially registered measurements for entire hearts.

More recently, however, diffusion tensor magnetic resonance imaging (DT-MRI) methods have been developed, which enable the non-destructive evaluation of soft tissue microstructure. DT-MRI methods quantify the self-diffusion tensor of water as water undergoes Brownian diffusion within the tissue microstructure. The diffusion tensor is estimated within each image voxel and can be decomposed into an eigensystem of three eigenvectors and three eigenvalues. The primary eigenvector (E_1), which is associated with the largest (primary) diffusion eigenvalue (λ_1), defines the direction of maximum diffusion and has been shown to correspond to the

[1] This work has previously been published in the Journal of Magnetic Resonance Imaging.

myofiber long-axis using quantitative histological methods[2-7]. The secondary (E_2) and tertiary (E_3) eigenvectors similarly correspond to cross-fiber direction (within the sheet and orthogonal to the myofiber long-axis) and the sheet-normal direction[2, 3, 84]. The ability of DT-MRI to quantify myolaminar geometry has previously been validated using non-standard histological methods[84].

The original description of the myolaminar sheet structure illustrated a single sheet population. More recently, however, biomechanical studies[26] and histological examination[25, 29, 67], have suggested the existence of a second sheet population. The two sheet populations are thought to be mutually orthogonal (or nearly so) and to co-exist within small, histologically observable tissue volumes. In fact, the established histological method of measuring myolaminar orientation[25] is often subjective due to the frequent presence of two observable sheet orientations. Whereas DT-MRI estimates of the two local sheet populations can be ranked according to their respective eigenvalues (λ_2 or λ_3), histological estimates of sheet orientation provide no means for distinguishing between the two apparent populations.

The objective of this study was to establish the correspondence between the two histologically observable myolaminar orientations (sheet angles, β) and DT-MRI measurements for the first time. We hypothesize that the secondary and tertiary eigenvectors of a voxel's diffusion tensor correspond to each of the two local myolaminar sheet orientations observed in histology. We also hypothesize that due to preparation artifacts, histology may obscure the second sheet population when in fact two local sheet populations always exist.

Establishing DT-MRI measurements as an adequate alternative to quantitative histology is advantageous because it avoids tedious and subjective histological methods and provides quantitative measures of tissue microstructure with perfect three-dimensional registration.

Using perfusion fixed sheep hearts, we will show that secondary and tertiary eigenvector estimates of the local sheet orientations correspond with histological measurements of the two sheet orientations in the same location of the same heart. The correlation of the primary eigenvector's local fiber orientation with histological fiber measurements will also be shown for completeness. Additionally, we will show that differences in diffusion tensor characteristics between histological locations showing one local sheet population and locations showing two local sheet populations are statistically insignificant, indicating that all myocardial tissue may be comprised of two local sheet orientations.

MATERIALS AND METHODS

Ovine Heart Tissue Preparation

All animals used in this study received humane treatment according to local institutional and federal guidelines. The animals used in this study are a subset of those previously used as a control group in a study of chronic mitral regurgitation[85, 86]. Additional detail about the experimental procedures is available[85, 86] and the salient details are briefly reported herein. Sheep in the control group underwent left thoracotomy for the transmural implantation of miniature tantalum markers in the antero-basal (ANT) and lateral-equatorial (LAT) wall, which were used for previous studies of cardiac kinematics and for anatomical registration purposes herein. At the end of the twelve-week study the animals were euthanized with an injected bolus of potassium chloride (80mEq) while under sedation with inhalational isoflurane[86]. Subsequent to euthanasia the left ventricular pressure was adjusted to match the in vivo measured end-diastolic pressure by means of controlled exsanguination. The coronary ostia were cannulated with balloon catheters and 300mL of buffered glutaraldehyde (5%) was infused to fix the

myocardium. The heart was then excised by cutting the great cardiac vessels, grossly exsanguinated and rinsed with saline, then stored in 10% formalin for later histological processing. Six adult male sheep hearts (N=6) from the original control group were examined with both "gold standard" histological methods and DT-MRI and formed the study cohort for this report.

Diffusion tensor magnetic resonance imaging and image processing

The formalin fixed left ventricular myocardium was prepared for DT-MRI by placing the tissue in a custom built plastic container with o-ring seals and both a luer-lock supply and vent cap through which a susceptibility matched fluid (Fomblin Y-LVAC 6-06, Solvay Solexis, West Deptford, NJ) was injected into the container, immersing the heart. The heart was held in place within the container using open-cell foam and oriented to grossly align with the long axis of the container and subsequently the MRI scanner.

A two-dimensional, slice-interleaved, diffusion weighted, twice-refocused spin echo, echo-planar pulse sequence was used to acquire diffusion tensor data in the fixed hearts using a 1.5T GE Signa Excite scanner and an 8-channel head coil. The following pulse sequence parameters were used: TE/TR=84ms/4800ms, *b*-value=1500s/mm^2, 55 non-colinear and non-coplanar encoding directions[87], nine non-diffusion weighted image volumes, echo train length of 4 (i.e. 32 shots), 4 averages, and ±62.5kHz bandwidth. The in-plane imaging resolution was 1mm x 1mm x 3mm obtained by using a 128x128 encoding matrix, 40 interleaved slices and a 128mm x 128mm x 120cm imaging volume. The median SNR was calculated for each heart and the mean ± standard deviation of the medians for all hearts was 32±3. The total imaging time for each volume was 10.2 minutes, for a total imaging time of 10.2 hours per heart. After scanning the

heart was returned to 10% formalin until the time of histological processing.

Diffusion tensors were reconstructed from the diffusion weighted images using linear regression. The diffusion eigensystem and the three orthogonal tensor invariants (norm, fractional anisotropy, and mode)[10] were calculated for each imaging voxel's diffusion tensor. Diffusion tensor invariants provide a basis for comparing components of tensor shape between different regions and are a tool for quantifying differences in regional microstructure. Tensor norm measures the magnitude of the isotropic component of the tensor, fractional anisotropy (FA) measures the magnitude of the anisotropic component of the tensor, and tensor mode defines the kind-of-anisotropy (e.g. planar anisotropic, orthotropic, or linear anisotropic)[10]. All computations were performed using Matlab (The Mathworks, Nattick, MA).

In order to measure fiber and sheet orientation from the DT-MRI data, a local coordinate system was defined within each myocardial voxel. The right-handed "cardiac" Cartesian coordinate system used by Harrington et al.[25] and others provides a local set of orthogonal axes consisting of a circumferential axis (X_1) pointing counter-clockwise when viewed from base to apex in an axial DT-MRI slice and, for example, tangent to the epicardial surface; a longitudinal axis (X_2) pointing from the apex toward the base and through the aorto-mitral meatus; and a radial axis (X_3) pointing from endocardium to epicardium. This local coordinate system was defined for every voxel occupied by myocardial tissue as depicted by Figure 1. The high myocardial contrast-to-noise ratio provided by the high image SNR and the use of Fomblin embedding solution for DT-MRI permits facile delineation of myocardium from background. Myocardium was segmented from non-myocardium within each short axis imaging plane by manually segmenting the high quality non-diffusion weighted images in ImageJ (National Institute of Health, Bethesda, MD). Non-myocardial voxels with high signal intensities, such as

fat and post-surgical adhesions, were manually segmented as non-myocardium on a voxel by voxel basis to ensure smooth epicardial and endocardial boundaries. Furthermore, the sites selected for analysis were not immediately adjacent to either papillary muscle. The relatively smooth ovine endocardium further facilitated border delineation.

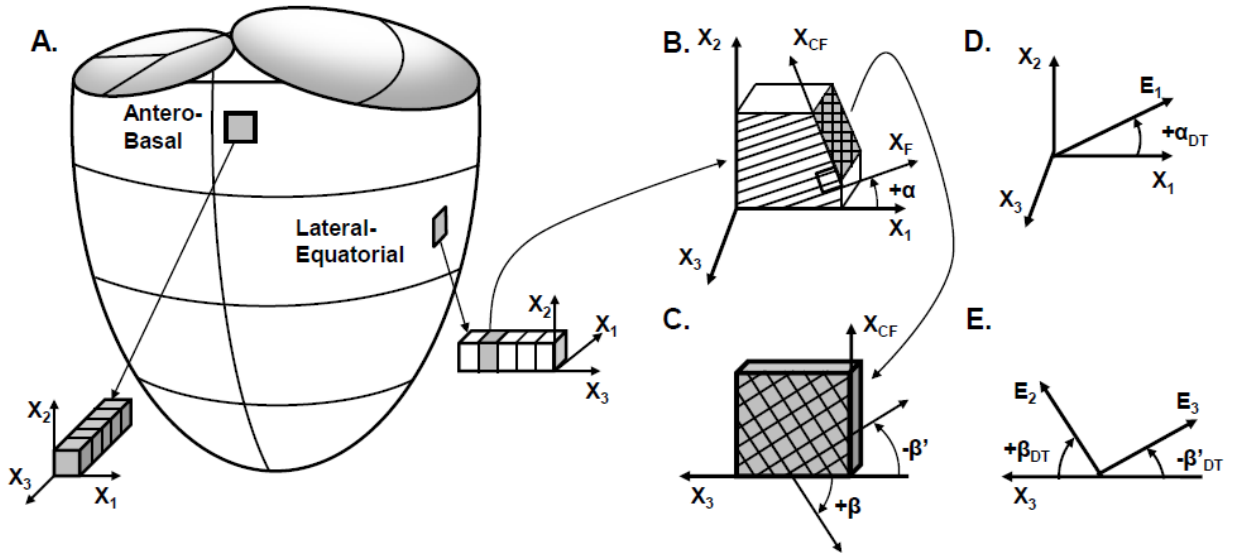

Figure 1: Myocardial fiber and sheet angles were measured using quantitative histological methods within transmural tissue blocks from the antero-basal or lateral-equatorial wall (A). The local cardiac coordinate system and local fiber angle is depicted in (B), wherein the local circumferential axis (X_1), longitudinal axis (X_2), radial axis (X_3), fiber axis (X_F) and cross-fiber axis (X_{CF}) are defined and used to quantify the local fiber angle (α). An *en face* view of the X_3-X_{CF} plane in (C) allows depiction of the two sheet angles (β and β'). Fiber and sheet angles were also measured using DT-MRI. The DT-MRI fiber angle (α_{DT}) was defined using the primary eigenvector (E_1) and local circumferential axis (X_1) in (D). The DT-MRI measured sheet angles (β_{DT} and β'_{DT}) were defined using the secondary (E_2) and tertiary eigenvectors (E_3) and the local radial axis (X_3) in (E).

The local longitudinal direction, X_2, was identical for every voxel of each heart. The local X_1 and X_3 vectors were constrained to lie in the plane normal to X_2, thus X_1 and X_3 did not necessarily lie in the short-axis imaging plane. X_1 and X_3 were derived from periodic cubic b-splines and twenty control points fitted to the epicardial and endocardial contours of the short-axis slice containing the ANT or LAT region of interest for each individual heart (Figure 2A). Linear weighting of the control point values provided a means to generate four additional intramural contours. The local b-spline tangent direction was used to define the X_1 direction constrained to lie within the plane normal to X_2. The local X_3 direction was defined as the cross-product of the local X_1 and X_2 and pointed in the endocardial-to-epicardial direction (Figure 2B).

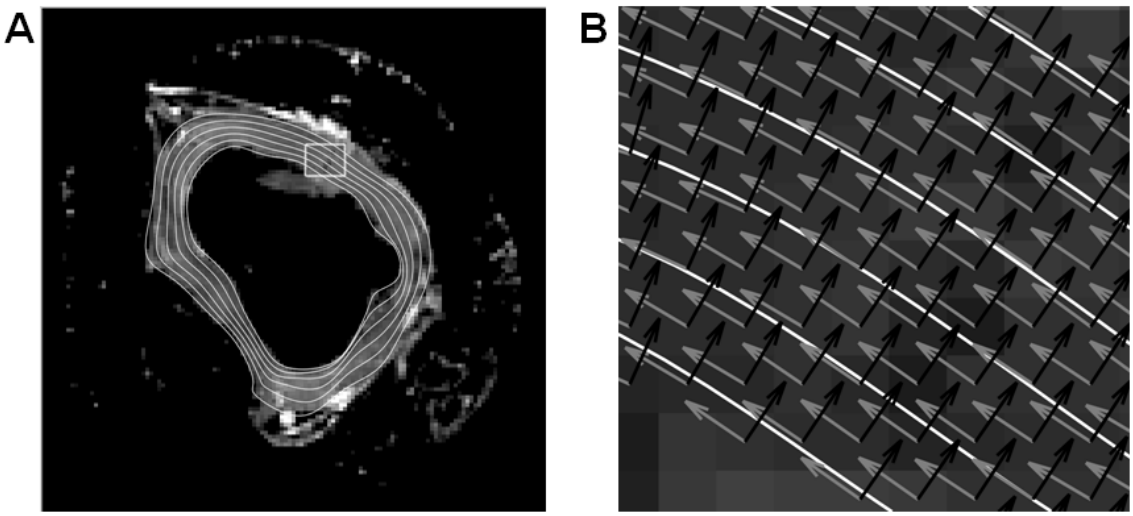

Figure 2: (A) Epicardial and endocardial contours (white) were derived from b-spline polynomials fitted to segmented images of individual LV short-axis slices and is shown overlaid on the corresponding non-diffusion weighted axial MR image. The intramural contours were derived by weighting the b-spline weights at each control point and these contours were subsequently used to define local circumferential (X_1, gray) and radial (X_3, black) vectors (B), which is a zoomed-in view from the box in (A).

Within the local, cardiac coordinate system, the local fiber angle (α_{DT}) was measured using the angle subtended by the primary eigenvector (E_1) and the vector defining the local X_1 for each voxel in Matlab using Equation [1]:

$$\alpha_{DT} = \tan^{-1}\left(\frac{\|X_1 \times E_1\|}{X_1 \bullet E_1}\right) \qquad [1]$$

Fiber angles were defined on the interval of [-90°,+90°] with a negative α_{DT} defined by a clockwise rotation from X_1 to E_1 about the positive X_3 direction and a positive α_{DT} defined by a counter-clockwise rotation from X_1 to E_1 about the positive X_3 direction (Figure 1D).

The two local sheet angles (β_{DT} and β'_{DT}) were measured using the angle subtended by E_2 and the local X_3 (β_{DT}) and the angle subtended by E_3 and the local X_3 (β'_{DT}) using Equation [1] replacing X_1 with X_3 and replacing E_1 with E_2 and E_3 respectively. β_{DT} or β'_{DT} was negative if the angle was defined by a counterclockwise rotation from X_3 to E_2 or E_3 when viewing the positive X_3-axis pointing from right to left (endocardium on the right) and positive if the angle was defined by a clockwise rotation from X_3 to E_2 or E_3 when viewing the positive X_3-axis pointing from right to left (Figure 1E). The sheet angles were defined within the interval of [-90°, +90°]. α_{DT}, β_{DT} and β'_{DT} were calculated within every myocardial voxel throughout the myocardium.

Histological preparation and image processing

Subsequent to DT-MRI the sheep hearts were prepared for histological measurement using the method of Harrington et al.[25] and Ennis et al.[88], which is briefly summarized herein. From each heart, two transmural blocks of tissue approximately 1cm in length along the X_2 (longitudinal direction pointing from the apex toward the base and through the aorto-mitral

meatus) and X_1 (circumferential direction perpendicular to X_2 in the epicardial tangent plane) directions were excised – one from the antero-basal wall and the other from the lateral-equatorial wall immediately adjacent to the regions wherein the sets of tantalum markers were implanted ([86]).

Each transmural block of tissue was sliced into 1mm-thick transmural sections parallel to the X_1-X_2 plane using a set of parallel ganged razor blades. This provided a series of 6-9 slices from epicardium to endocardium depending on the wall thickness at each heart's ANT or LAT region. The transmural depth, measured in percent wall depth (WD), of each slice was determined by the number of slices obtained from each tissue block. Measurements were made from the epicardial aspect of each section and the first slice of each block defined the 0% WD corresponding to the epicardium. The WD for the Nth slice for a block of tissue with a total of M slices was defined as: %WD=100(N-1/M).

Each transmural slice was placed on a note card and affixed using cyanoacrylate, with the positive X_1-axis coinciding with the horizontal edge of the slice and pointing to the right, positive X_2-axis coinciding with the vertical edge of the slice and pointing up and positive X_3 facing out of the note card towards the observer (Figure 3A). The resulting transmural samples were digitally photographed in this orientation to ensure a consistent local coordinate system for each measurement of histological fiber angle.

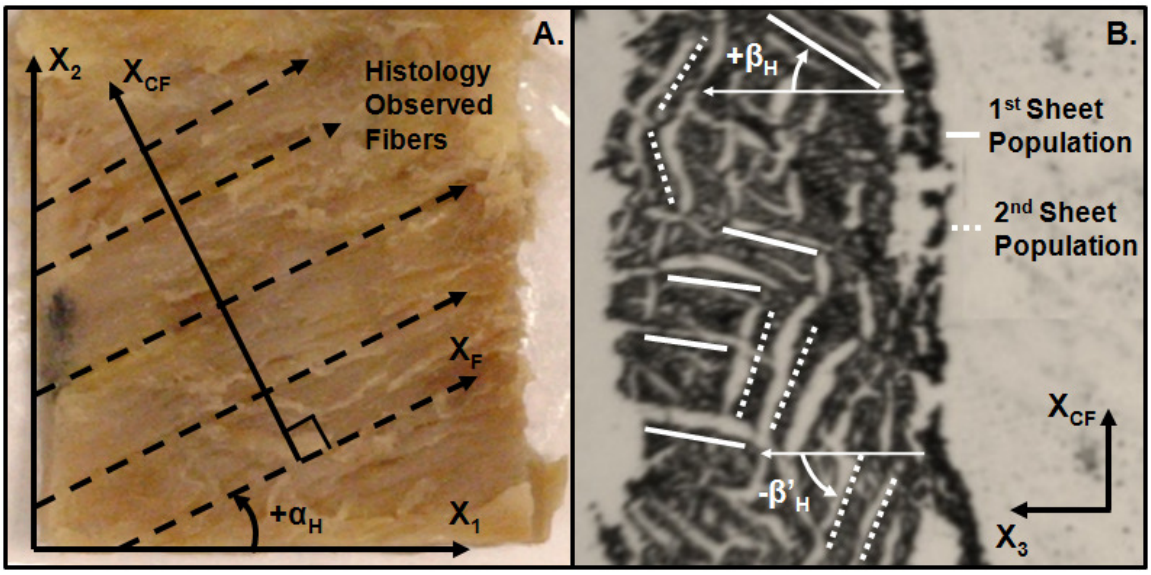

Figure 3: (A) Histological photo of observed fibers and depiction of histological fiber angle (α_H) measured between local X_1 and X_F. Each dashed vector is a representative measure made by the observer. The local X_2 and X_{CF} axes are also shown. The local X_3 direction (not shown) points out of the page toward the observer. (B) Histological photo of two observable sheet populations and depiction of histological sheet angles (β_H and β'_H) measured with respect to the local X_3 direction. The local X_{CF} also shown, X_F (not shown) points out of the page toward the observer.

The same local coordinate system used to measure DT-MRI angles was used to make histological measurements. A local fiber axis (X_F) defined by the observed fiber direction within a transmural tissue section and a local cross fiber axis (X_{CF}) defined by the direction normal to X_F within the tissue section were also identified to facilitate histological measurement (Figures 1B and 3A). Using custom image-processing software written in Matlab, the local X_1 direction was identified from the bottom edge of the tissue block, then five or more vectors evenly distributed across the image and oriented along the local myofiber axis (X_F) were drawn (Figures 1B and 3A). A single X_{CF} was manually identified in each photo as the vector normal to the

average of the drawn X_F vectors. The histological myofiber angle (α_H) within each transmural section was defined by the average angle subtended by the drawn X_F vectors and the local X_1 within each digital image (Figures 1B and 3A). Fiber angles were defined on the interval of [-90°, +90°] with a negative α_H defined by a clockwise rotation from X_1 to the observed X_F about the positive X_3 direction and a positive α_H defined by a counterclockwise rotation about the positive X_3 direction.

After photographing each transmural tissue section, the section was cut along the cross-fiber axis (X_{CF}) in the X_1-X_2 plane for direct visualization of the myolaminar sheets (Figures 1B-C and 3). This resulted in a 2-3mm wide (in the X_{CF} direction) strip of 1mm thick (in the X_3 direction) tissue bound to the note card. The note card was bent perpendicular to the plane of the tissue, placed in a shallow plastic mold (Tissue-Tek, Cryomold Intermediate, Miles, Elkhart, IN), filled with Optimal Cutting Temperature (OCT) compound (Tissue-Tek, Sakura Finetek, Torrance, CA), and frozen at -80°C for later microscopic evaluation of the sheet angles. At the time of microscopic evaluation the OCT embedded tissue was cut into 8-10μm thick sections (1-3 sections per transmural tissue sample) with a microtome, transferred to a glass slide, and photographed at 25x using a microscope with an attached digital camera (Figure 3B). Every histological digital image had the same orientation of the positive X_3-axis (pointing right-to-left) and the X_{CF}-axis (pointing bottom-to-top) and captured a 1mm wide (along X_3) by 10mm tall (along X_{CF})section of tissue (Figure 4). This assured similarity in tissue sample size for the determination of local sheet orientation between histological (1mm x 10mm samples from photos) and DT-MRI (1mm x 1mm x 3mm voxel resolution) measurements of sheet orientation. In our experience the tissue volume that was observed in histology was sufficiently large enough, such that any increase in size would not have changed the histological grade for the sample being

observed.

One or two histologically observed myolaminar sheet population angles (β_H and β'_H) were determined from the observable cleavage planes within the microtome tissue sections. The observable cleavage planes are gaps between myolaminar sheets that run in the same direction as the sheets that surround them[25]. β_H was defined as the average angle subtended by the most dominant set of observable cleavage planes and X_3 from all the microtome sections per transmural site (Figure 3B). To ensure β_H is characteristic of each histological site, five cleavage planes evenly distributed throughout the image were measured and averaged to produce the β_H measurement. Whenever possible, β'_H was defined as the average angle subtended by a second set of five evenly distributed observable cleavage planes and X_3 (Figure 3B). The requirement for making a β'_H measurement was observing at least 5 cleavage planes in an obviously different direction than β_H. The sheet angles were defined within the interval of [-90°, +90°]. β_H or β'_H was negative if the angle was defined by a counterclockwise rotation from X_3 to the cleavage plane about X_F and positive if the angle was defined by a clockwise rotation from X_3 to the cleavage plane about X_F.

If only β_H was observed at a transmural site for a given microtome-cut section, that location was given a histology grade-1. If both β_H and β'_H were observed, then that location was given a histology grade-2. If no discernable sheet population was observable, then no measurement was recorded at that transmural site and the location was given a histology grade-0. Examples of each histological grade are depicted in Figure 4.

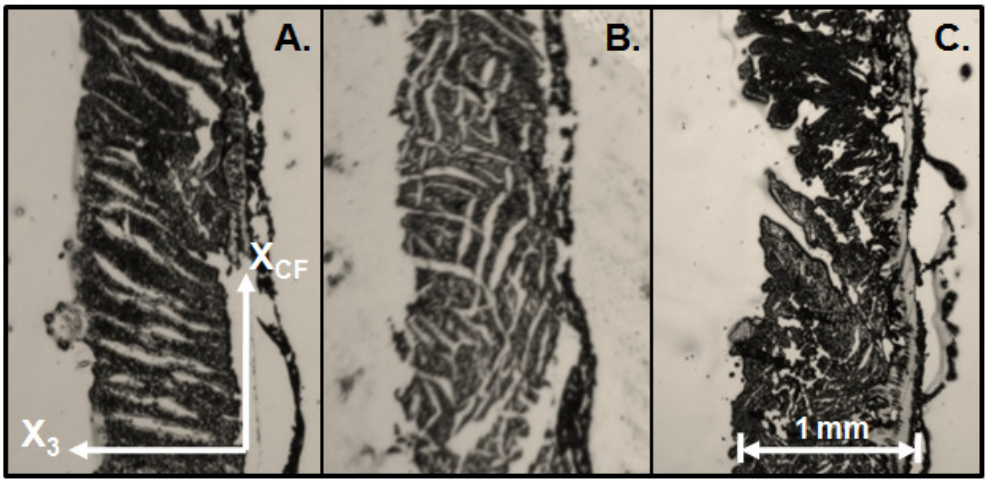

Figure 4: Histological photos of frozen microtome-cut sections showing sheet orientations perpendicular to fiber axis from representative samples of a range of appearances. (A) Corresponds to histology grade-1 (one distinct population of sheets); (B) corresponds to histology grade-2 (two distinct populations of sheets); (C) corresponds to histology grade-0 (no quantifiable sheet orientation).

If separate microtome sections from the same transmural site of the same heart showed inconsistencies between histology grades, then precedence was given to the microtome section(s) with the highest grade and the other(s) was unused for measurement (Figure 5).

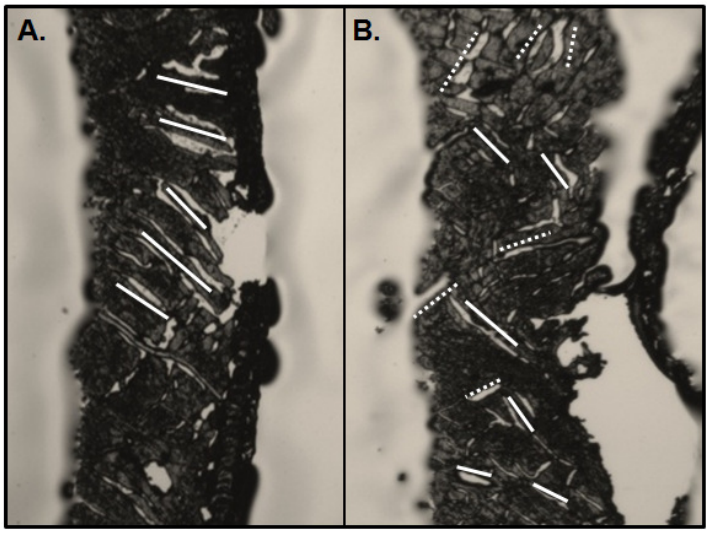

Figure 5: Histological photos of two microtome-cut frozen sections in the same transmural region of the same heart yielding (A) grade-1 and (B) grade-2 scores exhibiting the inconsistencies of histology measurements within the same histological site. In this specific case, the microtome section with the higher grade (B) was used for measurement and the lower grade microtome section (A) was unused.

Registering DT-MRI and histological measurements

In order to register DT-MRI and histology measurements, the axial slices selected for ANT and LAT DT-MRI measurements were chosen from the slice wherein the ANT and LAT tantalum markers were visible as small susceptibility voids. Regions of interest (ROIs) were created in the short axis DT-MRI images defined by two radial lines that spanned the entire transmural myocardial section; the signals from the tantalum markers were visible points along the edge of the ROI. The epicardial and endocardial boundaries served as the other two borders of the ROI. Within an ROI, all α_{DT}'s from DT-MRI voxels within ±5%WD of the corresponding histological WD were averaged to yield a single α_{DT} estimate corresponding to each transmural site measured by histology. The same method was used to yield a single β_{DT} and β'_{DT} estimate at each transmural site corresponding to histology. %WD from epicardium-to-endocardium was measured at every voxel in the ROI by calculating the distance from the voxel of interest to the nearest epicardial voxel, then dividing that distance by the total distance between the nearest epicardial and nearest endocardial voxels. Therefore, 0%WD corresponds to the epicardium and 100%WD to the endocardium. A total of N=80 estimates of α_{DT}, β_{DT}, and β'_{DT} were gathered corresponding to the 80 transmural sections of tissue obtained from histology.

This method established a one-to-one correspondence of α_{DT} to α_H. An apparent difference between α_{DT} and α_H may arise because α_{DT} is a direct measure of the angle between $E_1(=X_F)$ and X_1, while α_H is a measure of the apparent projection of the fibers (X_F) onto the X_1-X_2 plane. Therefore, we measured the angle difference between these two possible measures of myofiber angle in the DT-MRI data to account for this possible error.

For sites with a histological grade-2 score, β_{DT} and β'_{DT} were matched to β_H and β'_H. There exists, however, two possible pairings between DT-MRI and histological data in grade-2 cases: $\beta_{DT}\leftrightarrow\beta_H$ and $\beta'_{DT}\leftrightarrow\beta'_H$ or $\beta'_{DT}\leftrightarrow\beta_H$ and $\beta_{DT}\leftrightarrow\beta'_H$. β_{DT} and β'_{DT} are naturally rank ordered by their corresponding eigenvalues, but β_H and β'_H cannot be similarly, objectively ranked. The correspondence between β_{DT} and β'_{DT} to β_H and β'_H was, therefore determined by which pairing yielded the minimum square root of the sum of the squares of the differences between histology and DT-MRI pairings resulting in "best matches" defined by Equation [2].

$$\begin{aligned} &\text{If} \quad \sqrt{(\beta_H-\beta_{DT})^2+(\beta'_H-\beta'_{DT})^2} < \sqrt{(\beta_H-\beta'_{DT})^2+(\beta'_H-\beta_{DT})^2}\,, \\ &\text{Then} \quad \beta_{DT}\leftrightarrow\beta_H \text{ and } \beta'_{DT}\leftrightarrow\beta'_H \\ &\text{Else} \quad \beta_{DT}\leftrightarrow\beta'_H \text{ and } \beta'_{DT}\leftrightarrow\beta_H \end{aligned} \qquad [2]$$

Subsequently, the β_H and β'_H measurements were given an alternate designation based on the DT-MRI correspondence. $\beta_{H\text{-}E2}$ was designated to histological sheet angles that were paired with β_{DT} (thus associating with E_2) and $\beta_{H\text{-}E3}$ was designated to histological sheet angles that were paired with β'_{DT} (thus associating with E_3).

In grade-1 cases, only β_H was measured and β'_H was undefined. β_H was then matched with the DT-MRI measure (β_{DT} or β'_{DT}) that yielded the smaller difference. Transmural sites yielding

histology grade-0 were not evaluated for DT-MRI-histology comparison due to ambiguity in histological measurements.

During the registration process, DT-MRI sheet angle measurements may fall beyond the [-90°, 90°] range due to the phase-wrapping of DT-MRI measurements. Phase-wrapping allows angles separated by 180° to represent the same sheet orientation since sheets are not vectors and do not have a lead direction. Histological sheet angle measurements were always confined to [-90°, 90°] but in cases where the differences between DT-MRI and histology sheet angles exceed 90°, the differences can be reduced if β_{DT} and β'_{DT} are allowed to fall outside the [-90°, 90°] range.

Tensor invariants and eigenvalues within the ANT and LAT ROIs for each heart were given correspondence to a histologically defined %WD in the same manner as α and β registration to yield a single mean at each transmural wall depth for each invariant.

Statistical Analysis

Bland-Altman plots, including the measurement biases and 95% confidence intervals, were constructed to measure the agreement between α_{DT} and α_H as well as β_{DT} and β_H For myolaminar sheet orientations, additional Bland-Altman plots were constructed using the best match data for grade-1 histological sites and data for grade-2 sites. Mean differences were also calculated from the differences in the DT-MRI and histology measured pairs. Results are reported as mean ± one standard deviation. We also quantified the mean variance of each of the α_H, α_{DT}, β_H, β_{DT} and β'_{DT} measures within each transmural site in order to quantify the precision of those measurements.

A histogram was constructed to compare histologically measured and DT-MRI measured sheet angles at grade-1 and grade-2 locations. Histograms differentiating grade-1 and grade-2 locations were also constructed to compare the tensor invariants and eigenvalues between the two grades. The invariant and eigenvalue measures were bootstrapped 1000 times with replacement and the 95% confidence intervals of the bootstrapped means of each parameter were compared for grade-1 and grade-2 data. Bootstrapping was used because of the generally non-Gaussian distribution of the data.

RESULTS

Histological Grade

A total of 80 transmural sections were obtained for histology from the ANT and LAT regions of six hearts (6-9 sections per region per heart). Two sections had indiscernible fiber directions leading to no measurement of α_H and thus no measurement of β_H or β'_H, resulting in 78 corresponding estimates of α_{DT} and α_H. From these 78 transmural sites, 37 sites (47%) were scored histological grade-1 (only β_H observed), 38 sites (49%) were grade-2 (β_H and β'_H observed) and 3 sites (4%) were grade-0.

Myofiber Angle (α_{DT} versus α_H)

A paired comparison of α_{DT} and α_H (N=78 sites) yielded a mean difference and standard deviation of 1°±16°, which represents the systematic error between registering the two measures (Figure 6). Myofiber angle means had a mean SD of 6°±5° for histological measurements and 7°±8° for DT-MRI measurements. Additionally, the average angle difference between α_{DT}

measured from E_1 and X_1 and the angle measured from the projection of E_1 onto the X_1-X_2 plane and X_1 was 1°±10° for all myocardial voxels within the ROIs used in DT-MRI measurements.

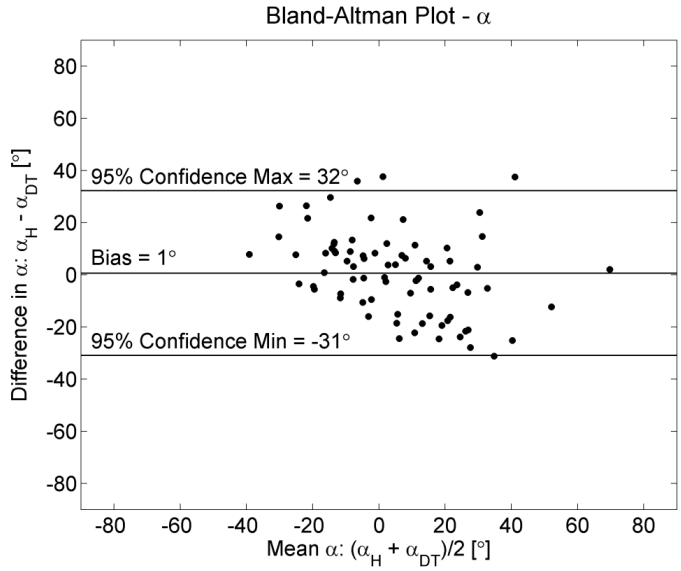

Figure 6: The measurement agreement between histology (α_H) and DT-MRI (α_{DT}) derived measures of fiber orientation is demonstrated with a Bland-Altman plot comparing seventy-eight measures of fiber orientation in six sheep hearts. Histology measures were positively biased by 1° with 95% confidence intervals of +32°/-31°. These results are in excellent agreement with previously reported comparisons of histologic and DT-MRI methods for quantifying fiber orientation[5, 6].

Myolaminar Sheet Angles (β_H and β'_H versus β_{DT} and β'_{DT})

In the 37 histology grade-1 cases, the mean difference between β_H and β_{DT} or β'_{DT} was 4°±29° (Figure 7A). β_{DT} was the best match in 14 cases (38%) resulting in a $\beta_{H\text{-}E2}$-β_{DT} mean difference of 20°±25° and β'_{DT} was the best match in 23 cases (64%) resulting in a $\beta_{H\text{-}E3}$-β'_{DT} mean difference of -6°±27°.

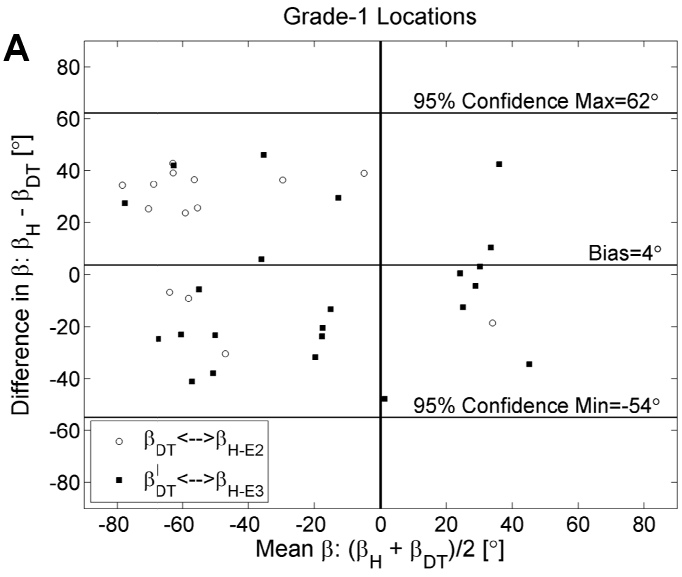
A
Grade-1 Locations
95% Confidence Max=62°
Bias=4°
95% Confidence Min=-54°
Difference in β: β_H - β_DT [°]
Mean β: (β_H + β_DT)/2 [°]
β_DT<-->β_H-E2
β'_DT<-->β_H-E3

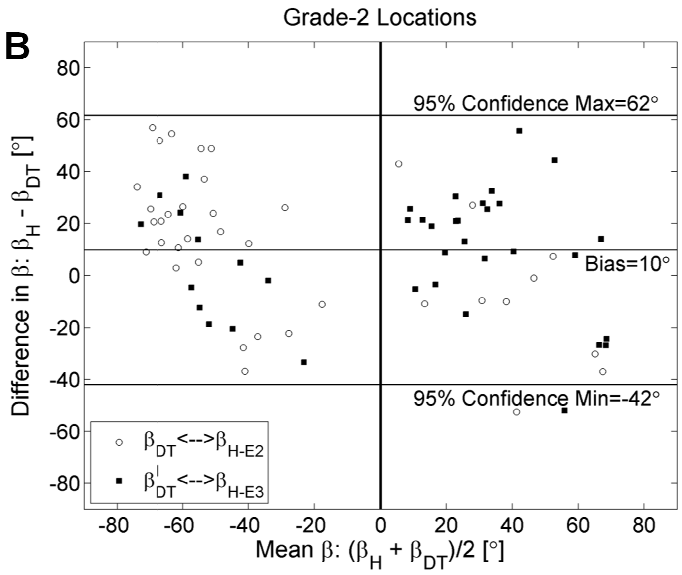
B
Grade-2 Locations
95% Confidence Max=62°
Bias=10°
95% Confidence Min=-42°
Difference in β: β_H - β_DT [°]
Mean β: (β_H + β_DT)/2 [°]
β_DT<-->β_H-E2
β'_DT<-->β_H-E3

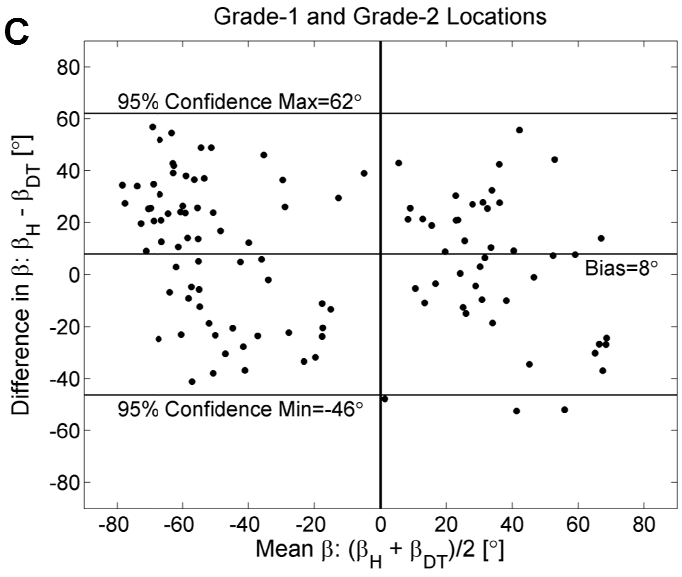

Figure 7: The measurement agreement between histology (β_H) and DT-MRI (β_{DT}) derived measures of sheet orientation is demonstrated with a Bland-Altman plot comparing 75 measures of sheet orientation in six sheep hearts when (A) histology yielded a grade-1 results (N=37); (B) histology yielded grade-2 results (N=76); and (C) grade-1 and grade-2 results combined. Results in (A) and (B) are grouped into pairings that correspond to E_2 (β_{DT} and its histological best match) and E_3 (β'_{DT} and its best histological match). A vertical line is shown at $(\beta_H + \beta_{DT})/2=0$ to emphasize the tendency for β-groups to be predominantly clustered into negative and positive groups.

β_H and β'_H were recorded at the 38 grade-2 histological sites leading to 76 "best matches" of DT-MRI sheet angles (β_{DT} or β'_{DT}) to histological sheet angles (β_H and β'_H). When using the best match of pairings between both DT-MRI measures (β_{DT} and β'_{DT}) and both histology measures (β_H and β'_H) at these sites, the mean difference and standard deviation was 10°±26° and is summarized in Figure 7B. The mean difference between $\beta_{DT} \leftrightarrow \beta_{H\text{-}E2}$ was 11°±29° and between $\beta'_{DT} \leftrightarrow \beta_{H\text{-}E3}$ was 8°±24°.

Combining all myolaminae orientation measurements (β_H, β'_H, β_{DT} and β'_{DT}) from both grade-1 and grade-2 cases yields a mean difference between DT-MRI and histology measures of 8°±27° (Figure 7C) and demonstrates a distinct bimodal distribution of distinctly positive and distinctly negative sheet angles as depicted in a histogram of all sheet angles in Figure 8A. Table 1 summarizes the results when grouping sheet angles from grade-1 and grade-2 sites into positive and negative groups. The differences in positive and negative sheet angle means are 84° for histology and 91° for DT-MRI.

Table 1. Mean histology and DT-MRI measured and combined sheet angles differentiated by positive and negative sheet angle value.

	Histology	DT-MRI
+β Mean	36°±18°	36°±24°
-β Mean	-48°±16°	-55°±28°

The spatial distribution of grade-1 and grade-2 histology shows no preference of either grade as a function of percent wall depth as depicted in 20% WD increments in Figure 8B. The largest discrepancy of grade difference occurs in the 80-100% WD range in which grade-1 is observed in 36% of histology cases while grade-2 is observed in 64% of histology cases.

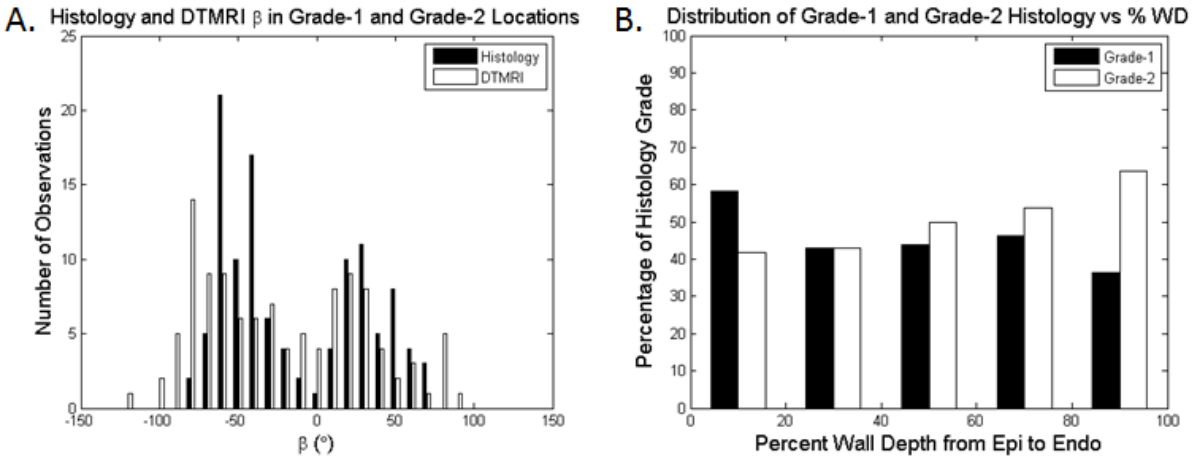

Figure 8: (A) The histogram of all histologically measured sheet angles (black) and DT-MRI measured sheet angles (white) at histological grade-1 and grade-2 sites combined shows the

bimodal nature of myolaminar orientation. The means of grouping sheet angles into negative and positive groups for DT-MRI and histology measurements is summarized in Table 1. (B) The percentage of occurrences of grade-1 and grade-2 histology versus percent wall depth in 20% increments depicting an even distribution of both grades regardless of transmural location.

We examined the variances of the myolaminae orientation means at each transmural site in order to observe the precision of those measurements. Myolaminar sheet angle means had a mean SD of 11°±4° for histological measurements and 21°±22° for β_{DT} and a mean SD of 24°±24° for β'_{DT}.

Diffusion Tensor Invariants and Eigenvalues

Diffusion tensor invariant and eigenvalue means corresponding to histological transmural sites show no significant differences when comparing grade-1 sites with grade-2 sites for ANT and LAT regions of all hearts (Figure 9). The overall means for tensor norm, FA and eigenvalues and the median tensor mode for all transmural sites and 95% confidence intervals for the bootstrapped statistic are summarized in Table 2. The median of tensor mode for all sites was used rather than the mean due to its non-normal distribution. Overlaps in the bootstrapped 95% confidence interval between grade-1 and grade-2 tensor invariant and eigenvalue data indicate no statistically significant differences in the underlying microstructural diffusive properties between grade-1 and grade-2 histological sites. Additionally, the lack of overlap between 95% confidence intervals for grade-1 between λ_2 and λ_3 and for grade-2 between λ_2 and λ_3 indicates a significant difference between λ_2 and λ_3 for both grades.

Table 2. Tensor invariant and eigenvalue data at grade-1 and grade-2 histological locations. The means ± one standard deviation (norm and FA) and median ± one standard deviation (mode) are listed as well as the 95% confidence interval for the means (norm, FA and eigenvalues) and median (mode) drawn from 1000 iterations of bootstrapping. Median was used for tensor mode statistics due to its non-normal distribution.

	Mean or Median ± SD		**Bootstrapped 95% CI**	
Parameter	**Grade-1**	**Grade-2**	**Grade-1**	**Grade-2**
Norm (mm²/s)	1.27e-3±0.17e-3	1.28e-3±0.14e-3	[1.22e-3;1.32e-3]	[1.24e-3;1.33e-3]
FA	0.33±0.09	0.34±0.08	[0.30;0.36]	[0.32;0.37]
Mode	0.57±0.35	0.53±0.49	[0.35;0.78]	[0.27;0.66]
λ_1 (mm²/s)	0.95e-3±0.13e-3	0.98e-3±0.11e-3	[0.92e-3;0.10e-3]	[0.95e-3;0.10e-3]
λ_2 (mm²/s)	0.64e-3±0.11e-3	0.67e-3±0.10e-3	[0.61e-3;0.68e-3]	[0.63e-3;0.70e-3]
λ_3 (mm²/s)	0.50e-3±0.09e-3	0.49e-3±0.09e-3	[0.48e-3;0.53e-3]	[0.46e-3;0.51e-3]

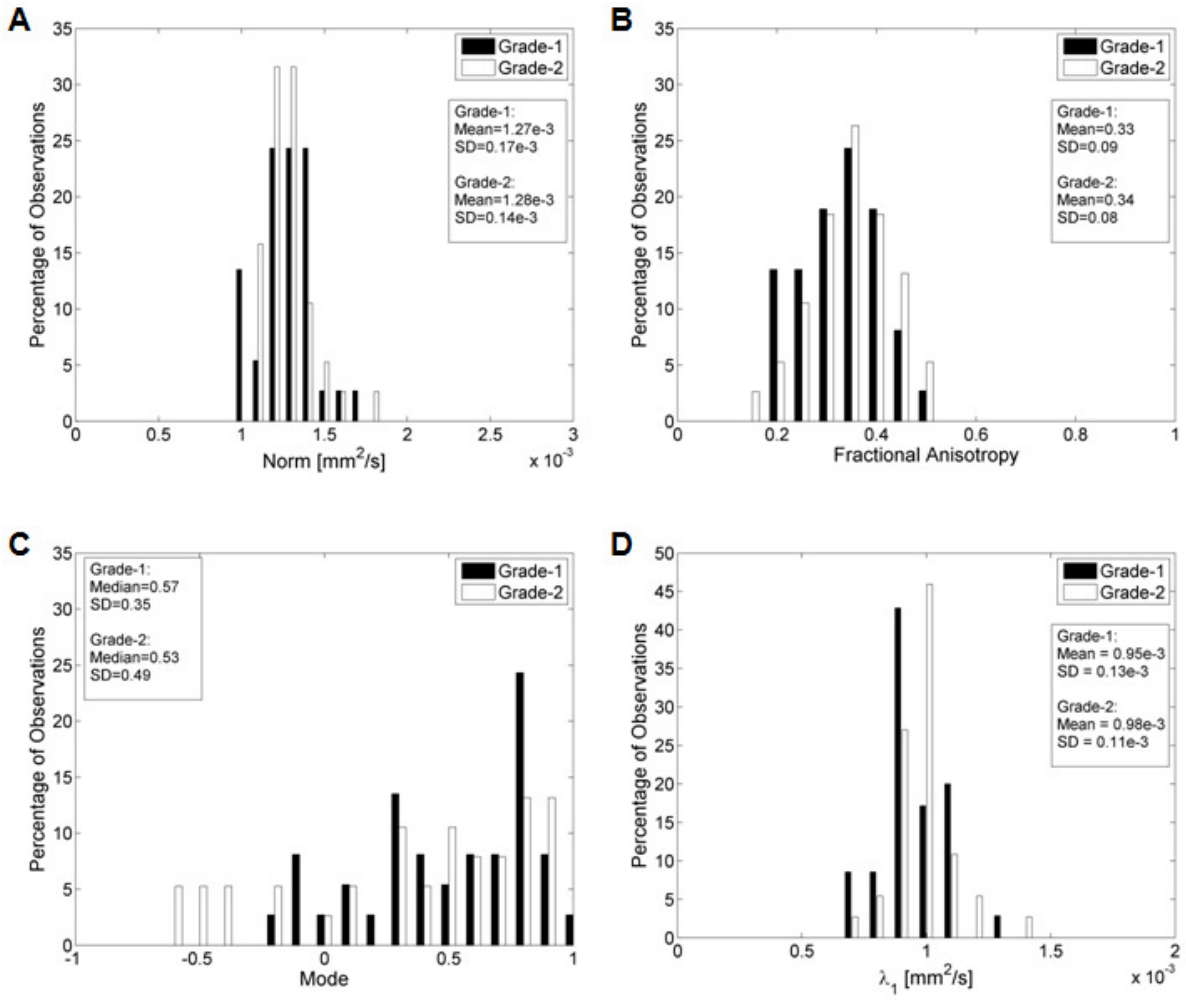

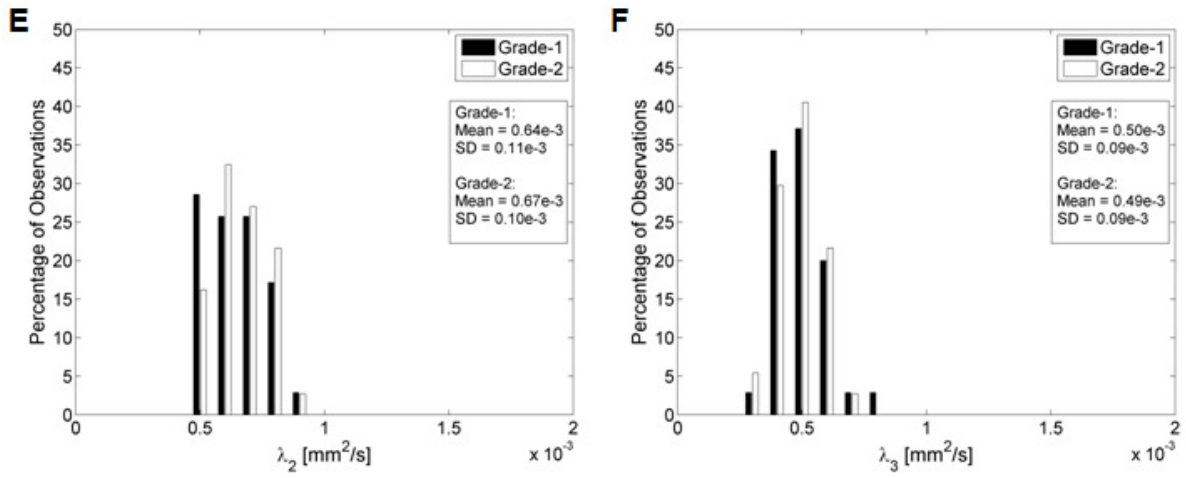

Figure 9: Histograms of diffusion tensor invariants that describe the (A) magnitude of isotropy (tensor norm); (B) the magnitude of anisotropy (fractional anisotropy); (C) the kind of anisotropy (tensor mode); (D) λ_1; (E) λ_2; and (F) λ_3 for tissue sections with histological grade-1 (black) or grade-2 (white) scores. There were no statistical differences between the grade-1 and grade-2 tensor invariants or eigenvalues indicating that the diffusive microstructure of the tissue is not significantly different, despite a different appearance with histology.

We also measured the standard deviations of the tensor invariants and eigenvalues for the voxels associated with each histologically defined transmural site in order to assess the variability of the measured data. The tensor norm, fractional anisotropy and tensor mode within each transmural site yielded mean SDs of 0.12e-3±0.09e-3 mm^2/s, 0.05±0.02 and 0.26±0.17 respectively. λ_1, λ_2 and λ_3 mean SDs of 0.09e-3±0.05e-3 mm^2/s, 0.07e-3±0.05e-3 mm^2/s and 0.07e-3±0.05e-3 mm^2/s respectively.

DISCUSSION

Myolaminae Orientation

Tseng et al.[84] are the only other group to have previously published a comparison of DT-MRI eigenvectors and sheet orientations measured in tissue. However, in that study, only angle differences between E_2 and a single local cleavage plane orientation from inked prints of cut faces in short axis, long axis and parallel to the epicardial tangent plane directions were measured. They did not report sheet orientation or sheet angle relative to any coordinate system. Thus, this study is the first to make a direct comparison of local sheet angles between histological and DT-MRI measurements.

Note that while the difference between means of positive and negative DT measured sheet angles is 91° as expected from measures derived from orthogonal eigenvectors, the difference between the means of positive and negative histology measured sheet angles is 84° for which there is no constraint. This supports the idea that the two sheet populations are nearly orthogonal in the end diastolic state. This bimodal and orthogonal distribution of myolaminae orientations observed in both DT-MRI and histology also compares well to previous studies wherein measured sheet orientation angles tend to cluster around a +45° range and a -45° range[2, 3, 25, 26]. Helm et al.[2, 3] used tertiary eigenvectors to define the sheet normal orientation and identified dominant myolaminae orientations at +45° and -63° in canine LVs. Harrington et al.[25] observed histologically measured myolaminae sheet orientations belonging to +45° near epicardial and endocardial regions and -45° in the midwall in ovine LVs. Pope et al.[29] also observed two orthogonal local myolaminae orientations in the rat LV using confocal microscopy. Finally, Hooks et al.[27] histologically observed dominant negative sheet populations with small “pockets”

of orthogonal positive sheet orientations in porcine LVs. Our work further confirms the presence of two sheet populations in myocardium.

The even distribution of histology grade as a function of percent wall depth implies no preference of one or two observable sheet populations based on transmural location. Myocardial sheets permit faster diffusion along the sheet direction (E_2) direction than the sheet normal direction (E_3) and slower than the fiber direction (E_1 or X_F). This has the consequence of leading to significant differences in diffusivity between λ_1, λ_2, and λ_3 such that $\lambda_1 > \lambda_2 > \lambda_3$. In the case of myocardium with two sheet populations that are orthogonal (or nearly so), the expectation would be that λ_2 (grade-1) > λ_2 (grade-2) and λ_3 (grade-1) < λ_3 (grade-2) because there would exist an additional path for the free diffusion of water along the E_3 direction and additional barriers along the E_2 direction. This increase in λ_2 and decrease in λ_3 for the grade-1 tissue relative to grade-2 tissue would cause tensor norm to increase (more freely diffusive), FA to increase (more anisotropic), and tensor mode to decrease (more planar anisotropic). However, there were no statistically significant differences between tensor invariants or eigenvalues in the grade-1 and grade-2 data, which indicate that the underlying microstructural diffusive properties of the tissue are very similar. There was, however, a significant difference between λ_2 and λ_3, which indicates significantly unequal diffusivities in the E_2 and E_3 directions. It is possible that histological sections wherein only one-sheet population is evident actually contain two sheet populations, but the second population is not always visible under histological examination. This is supported by inconsistent histology grades within multiple microtome-cut slices of the same transmural site, which was observed in 10 of the 59 (17%) transmural locations where multiple microtome cut sections were examined for myolaminae orientation by histology. Furthermore, in five transmural sites (8%), histology was scored grade-1 in one microtome-cut section and

grade-2 in another microtome-cut section (Figure 5). The cause of this phenomenon is not yet known. One possible explanation could arise from subtle differences in the microtome processing that result in cleavage planes from one particular sheet population opening more easily than cleavage planes from the other sheet population. This problem is avoided in DT-MRI as sheet orientation can be non-destructively evaluated on whole hearts without any histological preparation (cutting, slicing, freezing, sectioning, etc.).

Previous studies have explained the function of myolaminar sheets in cardiac mechanics. Legrice et al.[21, 23] explain interlaminar transverse shear of adjacent myolaminar sheets along their cleavage planes as the main mechanism of systolic wall thickening. Arts et al.[26] hypothesize that two sheet orientations do not occur simultaneously at a given transmural location but rather in patches and suggests that shear would split the tissue if both populations occurred in the same local region. This may be consistent with our findings as our imaging resolution is well above the size of the individual myolaminae. Harrington et al.[25] expands on transverse shear mechanics using their results of positive sheet populations in epicardial and endocardial regions and negative sheet populations in midwall regions to explain "accordion-like" systolic wall thickening. In their model, interlaminar transverse shear would alternate directions transmurally and minimize shear displacement of the epicardium relative to the endocardium. This "accordion-like" wall thickening mechanism can also apply to our more locally refined positive and negative sheet orientations. However, instead of alternating shear displacements from epicardium to midwall to endocardium; our model suggests locally alternating shear displacements at every transmural location in accordance to the two distinct sheet populations occurring throughout the entire LV myocardium.

Limitations with Myolaminae Orientation

This study assumes that E_2 and E_3 lie in the X_{CF}-X_3 plane thus allowing for an accurate correspondence to histological measurements, which is reasonable given the excellent agreement between α_{DT} (derived from E_1) and α_H. If E_2 and E_3 do not lie in the X_{CF}-X_3, β_{DT} and β'_{DT} would not directly correspond to the angles subtended by the cleavage planes observed in histology and the local X_3 axis within X_{CF}-X_3 plane. Instead, the β_{DT} and β'_{DT} measurements would correspond to the projection of cleavage planes onto the E_2-E_3 plane. This is not a significant limitation if the difference in β_{DT} and β'_{DT} is close to 90° meaning E_2 and E_3 lie close to the X_{CF}-X_3 plane and the 91° difference in the means of negative and positive DT measured sheet angles as reported earlier certainly supports this. Additionally, the small angle difference of 1°±10° between angles subtended by E_1 and X_1 and angles subtended by the projection of E_1 onto the X_1-X_2 plane and X_1 indicates that E_1 lies nearly on the X_1-X_2 plane at the observed locations. Because E_1 is normal to the E_2-E_3 plane and X_F is normal to the X_{CF}-X_3 plane, it is safe to assume that E_2 and E_3 do lie nearly in the X_{CF}-X_3 plane.

This study uses the mean of all DT-MRI measured myolaminae orientations from voxels within a specific transmural wall depth range of a specific ROI and correlates them to a single histological site, but does not account for the variance of sheet angles within these voxels. If voxels have a high variance within a specific region, then representing that region with a single estimate may not be effective in comparison to the mean of the corresponding histologically obtained sheet angle. This was not an issue within histology as variance of histological measurements within a particular histological site was small and did not yield a standard deviation over 25°. However, β_{DT} estimates yielded a mean SD of 21°±22° and β'_{DT} estimates yielded a mean SD of 24°±24°. Further improvements in SNR and spatial resolution should

reduce the SDs. The only tensor invariant that showed a large SD within mean measurements at transmural sites was the tensor mode, which yielded a mean SD of 0.26±0.17. The DT-MRI measured sheet angle and tensor mode means within these sites were still used for comparison to histological measures.

Our study compares histological and DT-MRI measurements in ANT and LAT regions of the LV and from these observations we infer that two local sheet populations may exist throughout the entire myocardium. Without performing a more extensive study of the entire myocardium we cannot prove the existence of two local sheet orientations at all myocardial locations. However, due to the tedious nature of taking histological measures, performing a whole heart histological study of fiber and sheet orientations is infeasible with current techniques.

The observer's subjectivity could change the mean or the variance in β_H. A change in the variance (assuming a symmetric distribution) will not have a significant effect because only the mean β_H is used for subsequent analysis. An increase in the mean β_H, however, would increase the bias measurement between β_H and β_{DT}/β'_{DT}. The subjectivity of the histological measurements may be reduced through the use of reliable, automated image processing methods, which may further improve the agreement between histological and DT-MRI data.

In conclusion we have shown DT-MRI measurements using secondary and tertiary eigenvectors correspond to each of the two local myolaminar sheet orientations observed in histology. Additionally, we have shown that two local sheet populations may exist throughout the LV myocardium and the histological observation of only one local sheet population may be due to preparation artifact.

CHAPTER 4

Microstructural Border Zone Remodeling in the Post-Infarct Porcine Heart Measured by Diffusion Tensor MRI and T1-Weighted Late Gadolinium Enhanced MRI[2]

INTRODUCTION:

Myocardial fibrosis as a consequence of post-infarct remodeling disrupts normal electrical wave front propagation, which contributes to the initiation of fatal ventricular arrhythmias[33, 44, 45]. In particular, the infarct border zone (BZ) facilitates slow conduction, reentry phenomena, and is implicated in arrhythmogenesis[43, 44, 89, 90]. Furthermore, anisotropic tissue conduction at epicardial border zones has been shown to influence occurrence of reentry[91].

T1-weighted late gadolinium enhanced (LGE) magnetic resonance imaging (MRI) is recognized as the gold standard for non-invasive myocardial infarct mapping[69-71]. In LGE MRI the slow washout time of Gd-DTPA in the extracellular space gives rise to hyper-enhanced signal intensity (SI) within the infarct[92]. The BZ is characterized by a mixture of replacement fibrosis and viable myocytes (which may hypertrophy) within the tissue and, as a consequence of partial volume effects, yields an intermediate SI in LGE MRI[43, 69].

LGE MRI indirectly indicates the presence of microstructural remodeling, especially in the infarct and BZ, but the extent of microstructural remodeling within the LGE identified BZ has not been characterized. Diffusion tensor MRI (DT-MRI) quantifies the self-diffusion tensor of water undergoing Brownian diffusion within each imaging voxel, which enables the direct quantitative evaluation of microstructural remodeling. Microstructural remodeling is frequently

[2] This work has been previously published in the Journal of Magnetic Resonance Imaging.

reported using tensor invariants, which saliently characterize important shape attributes of microstructural diffusion and are established as a tool for quantifying differences in regional microstructure[10]. Complementary information is found in the eigenvectors, which accord with the myofiber and myolaminae orientations[9].

A particularly useful set of microstructural remodeling components (tensor invariants) consists of: 1) *trace,* which measures the overall magnitude of isotropic diffusion and increases with decreasing tissue cellularity[14]; 2) *fractional anisotropy* (FA), which quantifies the magnitude of anisotropic diffusion and decreases with increasing fibrosis[72]; and 3) *tensor mode,* which gauges the kind of tissue anisotropy with mode values near zero indicating orthotropic diffusion indicative of sheet-like structures.

The objective of this study was to quantify microstructural remodeling in the BZ and infarct of a porcine left circumflex artery (LCx) balloon occlusion and reperfusion chronic infarct model using DT-MRI. This objective required developing the statistically appropriate methods for characterizing significant microstructural remodeling. We hypothesized that microstructural remodeling (changes in trace, FA and mode) within the BZ and infarct will constitute a significantly different microstructural environment.

MATERIALS AND METHODS:

Porcine Heart Preparation

Animal handling and care followed the recommendations of the National Institutes of Health Guide for the Care and Use of Laboratory Animals and the University of California, Los Angeles Institutional Animal Care and Use Committee. Animal protocols were approved by the University of California, Los Angeles Chancellor's Animal Research Committee.

Seven adult female Yorkshire pigs (40-55 kg) (N=7) underwent closed chest myocardial infarction via balloon occlusion of the LCx. Following a 12 hour fasting period, the animals were intramuscularly injected with 1.4 mg/kg Telazol, and then intubated. General anesthesia was maintained with inhaled 2.5% isoflurane. An obtuse marginal branch of the circumflex artery was occluded for 150 minutes with an angioplasty balloon via the retrograde aortic approach using an AL1 sheath from the right femoral artery. Evolving infarction was confirmed via ST segment elevation as assessed by continuous electrocardiogram monitoring.

After 6-8-weeks, the animals were intubated and placed under general anesthesia as above. Gd-DTPA was injected (0.1mmol/kg) and allowed to circulate for 15 minutes before euthanizing with a lethal dose of KCl directly into the heart. Normal adult female Yorkshire pigs (35-50 kg) (N=7) served as the control group undergoing identical sacrifice method without infarct induction.

After sacrifice, each heart was excised by cutting the great cardiac vessels, rinsed with saline and suspended in a saline filled container. With the heart suspended in saline, a high viscosity silicone rubber injection compound (Ready-Press Polyvinylsiloxane, Microsonic Inc., Ambridge, PA) was injected first through the pulmonary vein to fill the left ventricle and left atrium then through the superior vena cava to fill the right ventricle and right atrium, in order to maintain an approximate end diastolic cardiac anatomy[9]. The heart was then removed from saline and placed in a 1 L plastic cylindrical container filled with a susceptibility matched fluid (Fomblin Y-LVAC 6-06, Solvay Solexis, West Deptford, NJ). The heart was held in place within the container using open-cell foam and oriented to grossly align with the long axis of the container and subsequently the MRI scanner.

Late Gadolinium Enhancement Imaging

Imaging was performed on either a 1.5 Tesla (Avanto, Siemens AG, Munich, Germany) or 3 Tesla (Trio, Siemens AG, Munich, Germany) scanner using an 8-channel or 12-channel head coil respectively. Two hearts from the infarct group and five from the control group were scanned on the 1.5 Tesla scanner, while the other five hearts from the infarct group and two hearts from the control group were scanned on the 3 Tesla scanner.

A 3D gradient echo LGE MRI sequence on the 1.5T scanner was performed using the following pulse sequence parameters: TE/TR = 4.21/8.5 ms, flip angle = 20°, bandwidth = 260 Hz/pixel, 9 averages, and scan time = 2:05 (HH:MM). The imaging resolution was 0.33 mm x 0.33 mm x 0.50 mm (~800 myocytes per voxel) obtained by using a 384 x 384 x 256 encoding matrix and a 128 x 128 x 128 mm imaging volume. A 3D gradient echo LGE MRI sequence on the 3T scanner was performed using the following pulse sequence parameters: TE/TR = 4.24/9.35 ms, flip angle = 18.5°, bandwidth = 260 Hz/pixel, 9 averages, and scan time = 2:18 (HH:MM). The imaging resolution was 0.33 mm x 0.33 mm x 0.33 mm (~550 myocytes per voxel) obtained by using a 384 x 384 x 256 encoding matrix and a 128 x 128 x 85.33 mm imaging volume. All MRI exams began within two hours of sacrifice to ensure Gd-DTPA contrast did not diffuse significantly away from the infarct[69]. The SNR advantage of the 3T field strength was used to obtain thinner slices with SNR comparable to the 1.5T exams.

Diffusion Tensor Magnetic Resonance Imaging

Immediately after LGE imaging, spatially co-registered DT-MRI was performed. A two-dimensional, diffusion weighted, readout-segmented echo-planar pulse sequence[93] was used to acquire diffusion tensor data. The following pulse sequence parameters were used for

experiments performed on the 1.5T scanner: TE/TR = 80 ms/6800 ms, *b*-value = 1000 s/mm^2, 30 non-collinear diffusion gradient encoding directions, one non-diffusion weighted null direction, 15 readout segments, bandwidth = 439 Hz/pixel, and 8-10 averages. The imaging resolution was 1 mm x 1 mm x 3 mm (~45,000 myocytes per voxel) obtained by using a 150 x 150 encoding matrix, 43-44 slices and a 150 x 150 x 129-132 mm imaging volume. Pulse sequence parameters used for experiments performed on the 3T scanner were identical to the ones used on the 1.5 Tesla scanner except for a 76 ms TE. The total imaging time for each diffusion weighted volume was 3.4 minutes, for a total DT-MRI acquisition time of 7:00-8:50 (HH:MM) per heart.

Diffusion tensors were reconstructed from the diffusion weighted images using linear regression and custom Matlab (The Mathworks, Natick, MA) code. Trace, FA, and mode[10] were calculated for each imaging voxel's diffusion tensor. The diffusion tensors were visualized directly with superquadric glyphs, which are 3D surfaces that depict the tensor's shape and orientation and highlight regional organization and remodeling[66].

LGE Segmentation and Registration to DT-MRI

Segmentation – LGE images (Figure 1A) were segmented into remote, BZ, and infarcted myocardium and registered to the diffusion tensor images to enable microstructural remodeling analysis using the following steps. First, LGE images were averaged in the slice direction to match the slice thickness of corresponding DT-MRI data. Myocardial voxels were designated as remote, BZ, or infarct based on SI thresholds of the LGE images for each heart[69, 94, 95]. Regions of interest in remote myocardium (myocardial voxels with low SI) and infarct (myocardial voxels with high SI) were drawn in each heart to calculate the SI mean and standard deviation (SD) in each region for each infarcted heart. In accordance with the method used by Schelbert et

al.[69], segmentation of infarct and remote myocardium was defined using a threshold halfway between the mean SI of remote myocardium and the mean SI of infarcted myocardium on a per heart basis. The BZ was defined as voxels having an SI below this 50% SI level, but greater than two SDs above mean remote myocardium (Figure 1B)[69].

Registration – LGE and DT-MRI studies were performed back-to-back without adjusting the position of the tissue, but small spatial shifts still occurred over the long scan times. Therefore, 3D affine registration was employed between a binary mask created using simple SI thresholds of the myocardium in the LGE images and binary a mask of the myocardium from the DT-MRI data created using a custom tensor segmentation method[96]. The binary LGE masks were down-sampled in the in-plane directions using bicubic interpolation in Matlab to match the resolution of DT-MRI (Figure 1C).

LGE and DT-MRI data were registered first in the through-plane direction by aligning the LV apexes of both binary mask image sets, then registered via rigid translation in the in-plane direction using two dimensional cross-correlations in Matlab (Figure 1D). The registered LGE mask was then applied to the DT-MRI data to label each voxel as remote, BZ or, infarct (Figure 1E).

The DT-MRI segmentation was further refined by excluding infarct labeled voxels when the connected regions of infarct consisted of three or less voxels (Figure 1F), similar to Tao et al[95]. BZ segmentations were also refined by excluding voxels designated as BZ that were greater than three voxels away from infarct labeled regions.

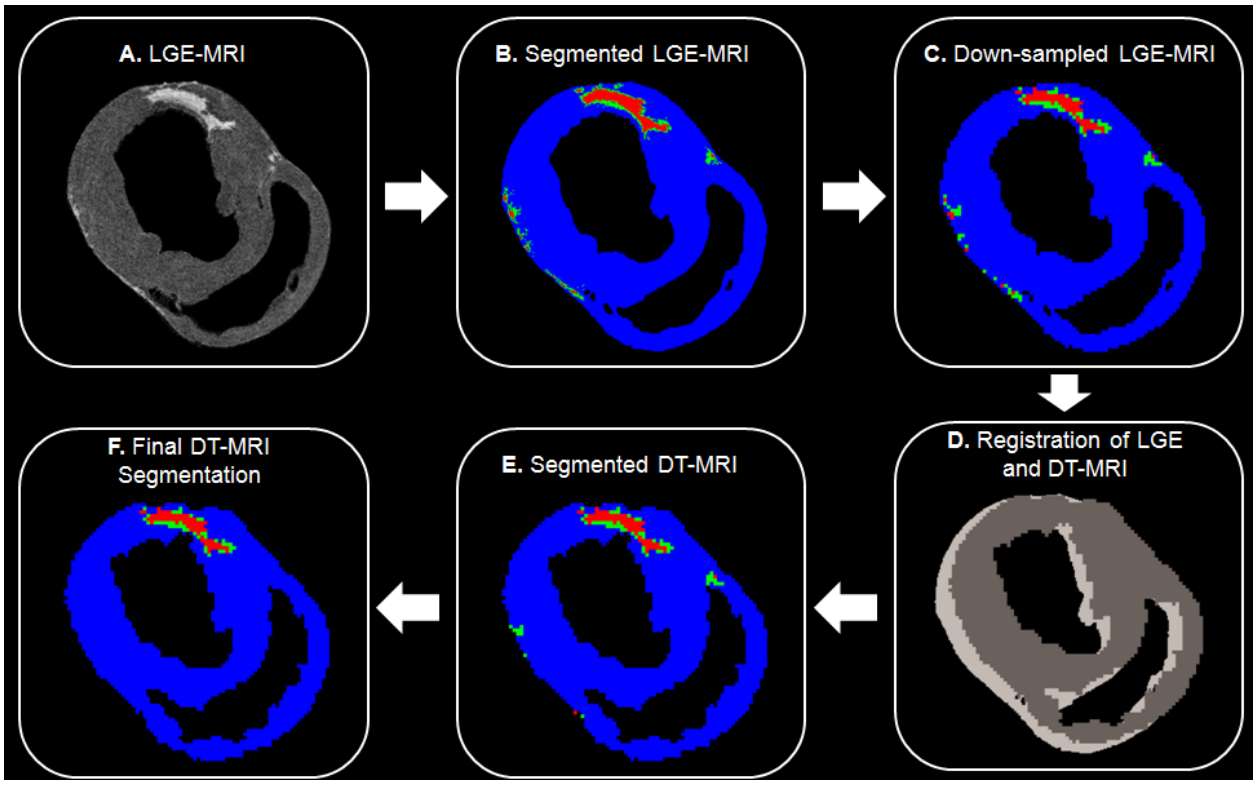

Figure 1: Registration of LGE MRI segmentation to DT-MRI. (A) Initial segmentation is performed on the LGE image. (B) The segmented LGE image (remote – blue, BZ – green, infarct – red) is (C) down-sampled to match DT-MRI resolution then (D) registered to DT-MRI via 2D cross-correlation. (E) The registered LGE segmentation mask is superimposed onto the corresponding myocardial mask of the DT-MRI data. (F) Final DT-MRI segmentation refined by excluding islands of high signal intensity consisting of three or less voxels (9 mm^3) and removing BZ signal intensities greater than three voxels (3 mm) away from infarct.

Statistical Analysis

The use of inferential statistics requires statistically independent samples. The highly organized arrangement of myocytes within normal myocardium, however, results in high spatial correlation of the diffusive properties within local myocardium and consequently to statistically

non-independent local diffusion tensors and tensor invariants. To produce statistically independent data points – trace, FA, and mode were spatially de-correlated in three dimensions within remote, BZ, and infarct regions via decimation by each region's auto-correlation length[97].

The standard formula-based statistical tests (e.g. t-test or ANOVA) require data to be approximately Gaussian in distribution and to have equal variances among populations. The distribution of tensor invariant data, however, is highly non-Gaussian with unequal variances across different populations[9]. Therefore, statistical significance tests were performed using bootstrap methods[97].

In order to compare the distributions of tensor invariants across remote, BZ, and infarcted myocardium, we produced bootstrapped histograms by sampling 1000 times with replacement from the segmented and de-correlated data to define 95% confidence intervals (CIs) within each of 32 histogram bins. A lack of overlap in 95% CIs between segmented regions within a histogram bin indicates a statistically significant difference within the invariant range of that bin. Furthermore, pairwise comparisons of regions within individual hearts were significantly different if the 95%-CIs of the bootstrapped medians did not overlap.

To test whether DT invariants significantly remodeled between remote, BZ, and infarct regions for pooled data from all infarcted hearts, we performed a bootstrap analog to repeated measures ANOVA of the de-correlated data[98]. Remote myocardium in infarcted hearts was also compared to myocardium in normal control hearts using a two-group comparison of the medians of de-correlated data. Bootstrapped repeated measures ANOVA and two-group comparisons were performed using the R programming language (http://www.r-project.org), where $p < 0.05$ was regarded as statistically significant. When reporting image quality and auto-correlation lengths, results are reported as mean±SD.

RESULTS:

Infarcts

Balloon occlusion of the LCx resulted in chronic infarcts that exhibited replacement fibrosis as evidenced by the elevated SI in the LGE images (Figures 1A and 2A). Infarcts regions were predominantly located in the inferior, inferoseptal basal to apical LV wall.

Visualization of Microstructural Remodeling

Figure 2A depicts a short axis LGE slice from an infarcted heart with corresponding DT invariant maps in Figures 2B-D showing an increase in trace (Figure 2B) and decrease in FA (Figure 2C) within the BZ and infarct regions. Figure 3 depicts the space of diffusion tensor shape rendered with superquadric glyphs spanned by FA and mode with median invariant values plotted on this space for normal (black), remote viable (blue), BZ (green), and infarcted (red) myocardium.

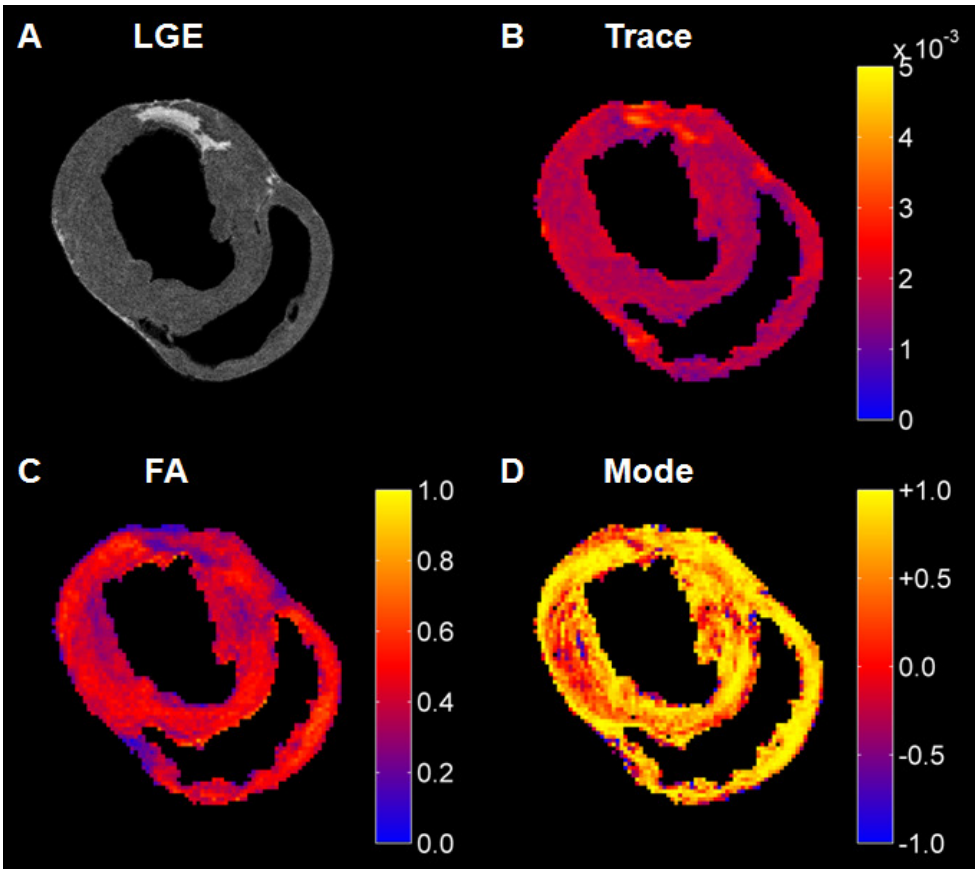

Figure 2: (A) Short axis LGE slice and the corresponding (B) trace, (C) FA and (D) mode maps. Regions of increased trace (B) and decreased FA (C) match similar regions of hyper-intense SI in the corresponding LGE MRI slice (A).

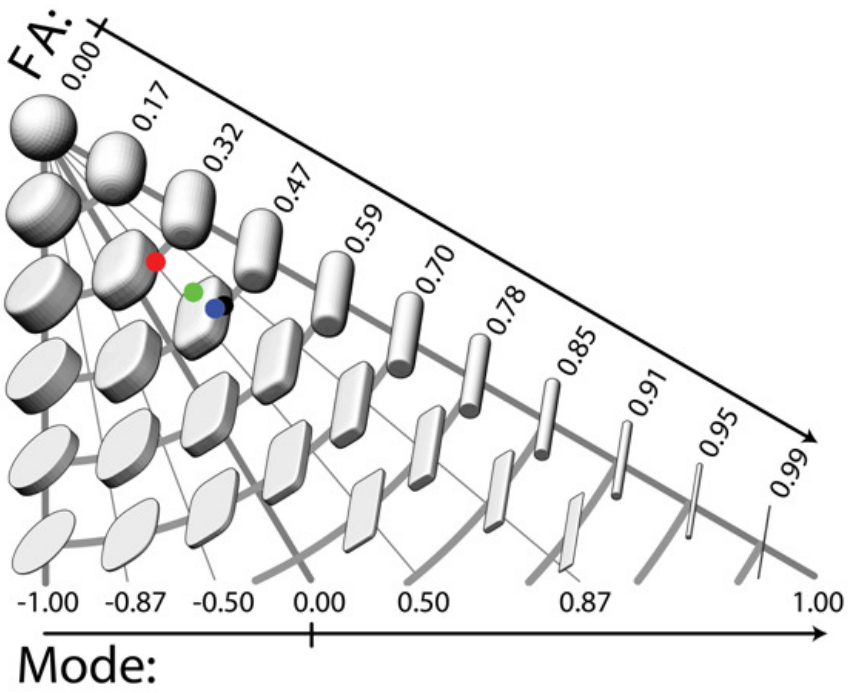

Figure 3: The space of diffusion tensor shape spanned by FA and mode rendered with superquadric glyphs. Median invariant values of all hearts taken from Table 1 are plotted for normal myocardium (black), remote (blue), BZ (green) and infarct (red) regions.

Figure 4A depicts, in three dimensions, diffusion tensor remodeling within a short axis slice, a long axis slice, and the entire infarct highlighted by a transparent isosurface. Each superquadric glyph's long axis aligns with each voxel's primary eigenvector and is color coded by mapping the primary eigenvector's components to red-green-blue colormap. The brightness of the infarct glyphs is increased for contrast. Figure 4B depicts the same short axis slice seen in Figure 4A. Figure 4C depicts the diffusion profile in normal, remote, BZ, and infarcted myocardium by rendering the median microstructural tensors using superquadric glyphs. Superquadric glyphs from the infarct are visibly larger (higher trace) and more isotropic (lower FA) than the glyphs represented by median invariant values from normal and remote

myocardium. Glyphs within the BZ of all infarcted hearts show an intermediate size (intermediate trace) and intermediate isotropy (intermediate FA) compared to the infarct, normal, and remote glyphs.

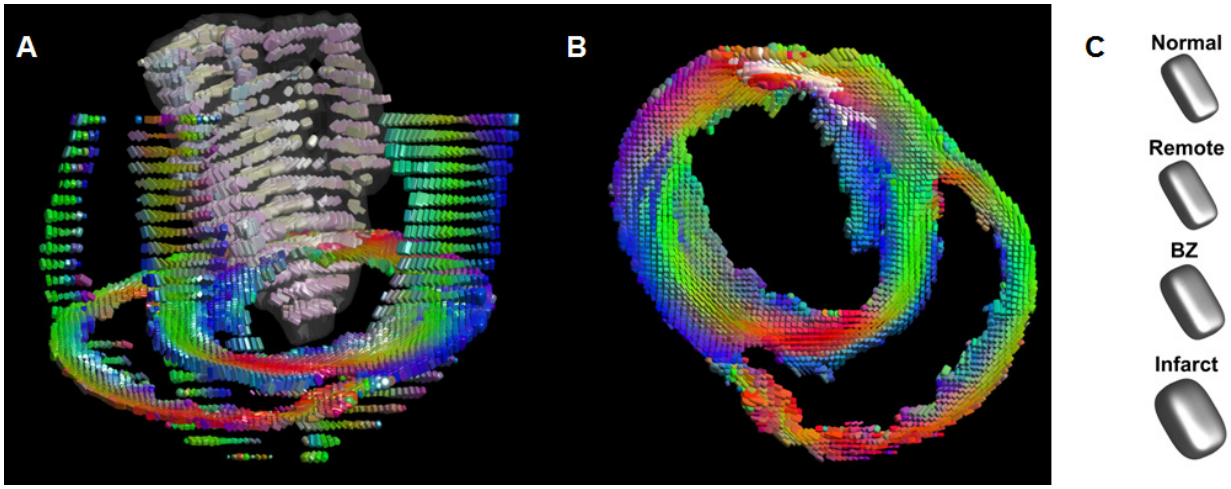

Figure 4: (A) Short axis, long axis and infarct depiction of diffusion shape and orientation rendered with superquadric glyphs. The long axis of each glyph is aligned with the primary eigenvector of the diffusion tensor at each voxel. Glyphs are color coded by the primary eigenvector direction with red grossly aligning with the x-direction, green with the y-direction, and blue with the through plane direction. The brightness of glyphs in the infarct is enhanced for contrast. (B) Same short axis slice as Figure 3A. (C) Glyphs from normal hearts and segmented regions of infarcted hearts using the median values of trace, FA and mode from Table 1.

Quantitative Evaluation of Microstructural Remodeling

LGE based segmentation of the DT-MRI data revealed significant differences in trace and FA data between all pairwise comparisons of remote, BZ, and infarct regions within each infarcted heart. The BZ within each heart is characterized by a significant increase in trace and

significant decreases in both FA and mode relative to remote myocardium. The infarct region within each heart is characterized by an even larger and significant increase in trace and significant decreases in FA and mode.

Table 1: Pooled tensor invariant medians and bootstrapped 95%-CIs of the medians for normal, remote, BZ, and infarcted myocardium. († $p<0.0001$ for bootstrap analog to repeated measures ANOVA, ‡ $p=0.02$ for two-group comparison)

Group/Region	Median Trace (mm^2/s)	95%-CI of Median Trace (mm^2/s)	Median FA	95%-CI of Median FA	Median Mode	95%-CI of Median Mode
Normal	0.00169	[0.00168, 0.00169]	0.470	[0.467, 0.473]	$0.743^{‡}$	[0.736, 0.749]
Remote	$0.00172^{†}$	[0.00172, 0.00173]	$0.464^{†}$	[0.462, 0.466]	$0.666^{‡}$	[0.660, 0.672]
BZ	$0.00194^{†}$	[0.00192, 0.00195]	$0.417^{†}$	[0.412, 0.421]	0.621	[0.603, 0.635]
Infarct	$0.00239^{†}$	[0.00236, 0.00242]	$0.330^{†}$	[0.325, 0.336]	0.515	[0.495, 0.538]

Figure 5 depicts pooled histograms with bootstrapped 95%-CIs of the de-correlated invariant data for each segmented region. DT invariant medians and their bootstrapped 95% CIs for each pooled region (normal, remote, BZ, and infarct) are listed in Table 1. Results from the bootstrapped analog to repeated measures ANOVA revealed significant differences across remote, BZ, and infarct regions for all hearts when comparing trace ($p<0.0001$) and FA ($p<0.0001$), but were not significant for mode ($p=0.47$). In a comparison of normal myocardium from controls and remote myocardium from infarcted hearts, two-group comparisons of the DT invariants did not reveal significant differences between median values of trace ($p=0.18$) and FA ($p=0.51$), but did show a significant decrease in mode ($p=0.02$) from normal to remote myocardium.

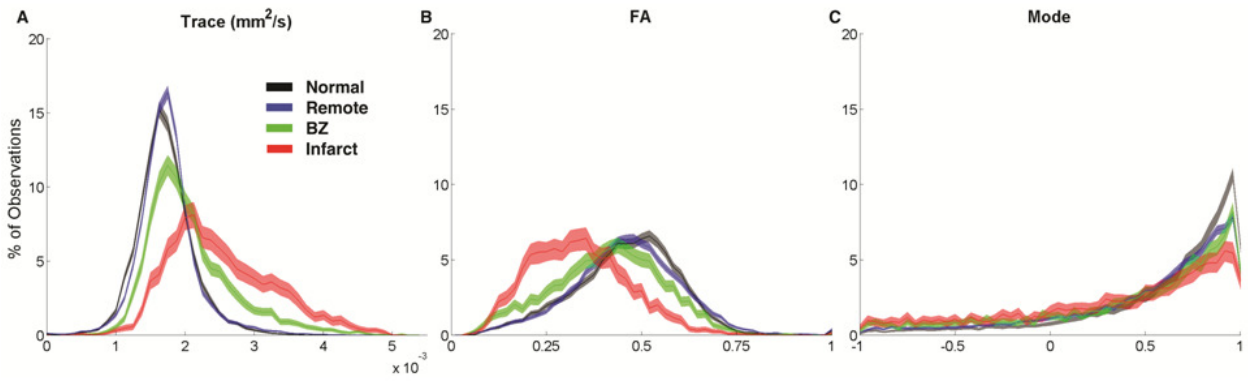

Figure 5: Bootstrapped histograms with 95%-CIs (for each bin) for the segmented regions (normal myocardium – black, remote – blue, BZ – green, and infarct – red) using spatially de-correlated data pooled from all hearts for (A) trace, (B) FA and (C) mode. Non-overlapping regions between histograms reveal significant differences within a given bin. Significant remodeling (increase in the median trace and decrease in median FA) is evident transitioning from remote to BZ to infarct histograms. Mode changes suggest an increase in fiber disarray within BZ and infarct regions.

Image Quality

The mean signal-to-noise ratios (SNR) for the LGE MRI experiments were calculated from each heart by selecting a region of interest in remote/normal myocardium and dividing it by the SD of an ROI of equal area in the background of the same slice for 5 equally spaced slices within each heart. The mean SNRs from the DT-MRI experiments were calculated from the non-diffusion weighted images for each heart in the same manner as the LGE images. The signal-to-noise ratio of the LGE images for all hearts was 10±2. The SNR of the non-diffusion weighted images of the DT-MRI was 59±15. 3D affine registration of LGE and DT-MRI data resulted in

shifting of the LGE data by 0.8±0.9 mm and 1.2±1.5 mm in the x- and y-directions (in-plane) respectively and 0.2±0.5 mm in the z-direction (through-plane).

Data De-correlation

Auto-correlation lengths were 3.0±0.6 voxels (3.0 ±0.6 mm) in the in-plane x- and y-directions and 1.8±0.2 voxels (5.4±0.6 mm) in the through-plane z-direction for normal hearts and remote myocardium in infarcted hearts. Auto-correlation lengths in the BZ were 1.2±0.1 voxels (1.2±0.1 mm) in the x- and y-directions and 1.1±0.2 voxels (3.3±0.6 mm) in the z-direction. Auto-correlation lengths in the infarct region were 1.7±0.2 voxels (1.7±0.2 mm) in the x- and y-directions and 1.2±0.1 voxels (3.6±0.3 mm) in the z-direction.

DISCUSSION:

Replacement fibrosis within an infarct significantly alters the electrophysiological properties of the myocardium, leading to reentrant ventricular arrhythmias. The BZ, consisting of a mixture of viable myocytes and fibrotic scar, facilitates slow conduction or reentry and is believed to serve as the substrate for ventricular tachyarrhythmias[44, 89]. Furthermore, premature ventricular contractions initiating ventricular fibrillation have been shown to elicit from the BZ[99]. Consequently, catheter-based ablation of the BZ is one strategy used to manage ventricular arrhythmias[100] and up to 68% of successful ablation sites reside in the BZ[101]. Thus, accurate characterization of the BZ is important for identifying the location of the arrhythmogenic substrate prior to catheter ablation. Previous work by Ashikaga *et al.* has suggested that the BZ is characterized by abnormal mechanics[102]. Therefore, in conjunction with the findings in this study, the BZ exhibits altered mechanics, electrophysiology, and microstructure.

The increase in BZ trace likely results from the mixture of fibrotic scar and viable myocytes, which increases the extracellular volume and decreases the cellular volume. The larger increase in trace within the infarct region corresponds to the dense fibrotic scar fully replacing viable myocytes in this region and accords with previous studies observing higher rates of diffusion in infarct regions[15, 72].

The observed decreases in FA within the BZ and infarct regions likely results from two remodeling phenomena: 1) the replacement of myocyte architecture with a more isotropic extracellular collagen network due to replacement fibrosis and; 2) an increase in myofiber disarray, which produces an apparent increase in the isotropy of water diffusion. Such observations of fiber disarray in infarcted myocardium have previously been observed[15, 16]. Decreased FA within the infarct from this study confirms observations of lower diffusion anisotropy within infarcted myocardium from previous studies[15, 72]. The observed decrease in the pairwise comparison of tensor mode within the BZ and infarct may result from an increase in fiber disarray as local diffusion shifts away from linear transverse isotropy towards orthotropic diffusion.

Differences in trace and FA between remote myocardium from infarcted hearts and normal myocardium from control hearts were not statistically significant. Previous studies have shown wall thinning and reduced strain[103-105], as well as myocyte lengthening and hypertrophy in remote myocardium when compared to normal controls[38]. However, collagen volume fraction is not significantly different in remote and control myocardium[49], which is consistent with the similar FA in those regions. The observed mode decrease from normal to remote myocardium indicates an increase in sheet-like structure, which may facilitate the previously observed remote compensatory hyperfunction and increased wall thickening[32].

Although previous studies have evaluated microstructural remodeling in post-infarct myocardium using DT-MRI[15, 16, 72, 73], they have used imprecise methods to segment regions into infarct, BZ, and remote regions using short-axis T2-weighted (non-diffusion weighted) images from the DT-MRI experiment. Our study is the first to use LGE MRI to create accurate segmentations of infarct and BZ on a voxel by voxel basis. Previous studies of myocardial remodeling after infarction using DT-MRI have also used t-tests to compare DT parameters between regions, however, due to non-Gaussian data sets, spatially correlated data, and unequal variances between data sets standard methods are not appropriate. By de-correlating the data and using bootstrapping methods this is the first study to correctly quantify statistically significant microstructural remodeling of BZ and infarcted myocardium using DT-MRI. These imaging and statistical methods establish that the BZ and infarct are unique microstructural environments.

Limitations

This study used a combination of LGE and DT-MRI to quantify microstructural remodeling in the post-infarct porcine heart, but histological data is not available to confirm the microstructural remodeling results due to tissue collection for another predetermined study. However, the histological characterization of BZ infarcts has been previously performed in detail. The purpose of this study was to identify MRI footprints of important histological changes. Furthermore, due to resolution constraints, voxels of intermediate SI designating BZ may arise from areas containing an interdigitated mixture of fibrosis and viable myocytes or from adjacent dense infarct and viable myocardium with a single well defined border[69]. The data from this study was not amenable to distinguishing between the two possible origins of intermediate SI and both were defined as BZ, but may have different electrophysiologic

implications. Improvements in DT-MRI resolution and imaging methods may alleviate this ambiguity in BZ segmentation, however, the resolution achieved in this study is similar to those used in previous porcine DT-MRI studies[72, 73].

In conclusion, LGE segmentation of DT-MRI data identifies regions of significant microstructural remodeling in both the BZ and infarct region relative to remote and normal myocardium. The large increase in trace and decrease in FA in the infarct indicates a significant increase in replacement fibrosis and a decrease in cellularity. The intermediate increase in trace and decrease in FA in the BZ suggest a unique intra-voxel mixture of fibrosis and viable myocytes. Hence, the BZ is a unique microstructural environment, which may explain its importance in ventricular arrhythmogenesis.

CHAPTER 5

Myocardial Microstructural Remodeling in Pacing Induced Heart Failure Measured by Diffusion Tensor MRI[3]

INTRODUCTION:

Heart failure (HF) is a leading cause of death in the United States affecting 5.1 million Americans in 2013 with a 50% mortality rate within 5 years of onset of HF[31]. HF is characterized by a deficiency of the contractile function of the heart due, in part, to global anatomical remodeling of the myocardium. A commonly used protocol to study heart failure is to induce HF via rapid pacing of the left ventricle (LV), which leads to volume overload. Pacing induced volume overload is known to lead to the progression of HF through several stages: 1) normal ventricular geometry; 2) acute dilation; 3) chronic compensated concentric hypertrophy; 4) chronic de-compensated eccentric hypertrophy; and finally 5) de-compensated dilation and wall thinning. In addition to global myocardial remodeling, changes in the myocardial microstructure, including its cellular and interstitial components, also contribute the HF. On a microstructural level, the progressive remodeling throughout the various stages of HF includes necrosis[11], myocyte lengthening and hypertrophy[11, 12, 36], and increased collagen volume fraction (CVF) signifying fibrosis replacement[11, 40]. HF is associated with changes in the complex myofiber and myolaminar structure of the heart as myocytes change shape or are replaced by fibrosis, which disrupts mechanical and electrical function and leads to an increased incidence of arrhythmia[33, 34]. The intricacies of three-dimensional (3D) microstructural remodeling in HF, however, remain incompletely understood.

[3] This work has been submitted for publication to the Journal of Magnetic Resonance Imaging.

In addition to pathological microstructural myocardial remodeling, species-specific transmurally heterogeneous myocardial microstructural organization has been observed in normal myocardium. For example, in normal rat myocardium there exists a transmural gradient of increasing myocyte volume and cross-sectional area from the epicardium to the endocardium[76, 106]. This has similarly been observed in ex vivo human hearts, wherein myofiber diameter increases from epicardium to endocardium in normal hearts and a loss of this transmural gradient has been observed in hypertrophic cardiomyopathy[77]. Finally, a progressive decrease in myocyte volume fraction and myolaminar branching has been observed from epicardium to endocardium in normal dog hearts, revealing an opposite transmural gradient of myocyte volume fraction compared to rats and humans[21]. Due, in part, to contradictory interspecies data, myocyte and microstructural spatial variations are still not fully understood.

Previous observations of myocardial microstructure have predominantly relied on histological methods[11, 12, 21, 22, 29, 76, 77, 106], which are exceedingly tedious and difficult to spatially register in three-dimensions (3D). Diffusion tensor magnetic resonance imaging (DT-MRI) enables the direct evaluation of soft tissue microstructure without the need for histological preparation. DT-MRI quantifies the self-diffusion tensor of water undergoing Brownian motion within the tissue microstructure, thereby providing quantitative insight to microstructural organization and remodeling. The diffusion tensor is estimated within each imaging voxel and can be decomposed into an eigensystem of three eigenvectors and three eigenvalues. The primary eigenvector has been shown to align with the local myofiber direction and the secondary and tertiary eigenvectors has been shown to align with local myolaminae cross-fiber and sheet normal directions, respectively[6, 9]. Meanwhile, the eigenvalues contain information about the shape of the local diffusion tensor. The eigenvalue information is frequently reported using

tensor invariants, which saliently characterize important shape attributes of microstructural diffusion and are an established tool for quantifying differences in regional microstructure[10]. A particularly useful set of tensor invariants consists of: 1) *trace,* measured in units of diffusivity (e.g. mm^2/s), which measures the overall magnitude of isotropic diffusion and has been shown to increase with decreasing cell density[14]; 2) *fractional anisotropy (FA)*, a dimensionless measure ranging from [0,1], which quantifies the magnitude of anisotropic diffusion and, for example, decreases with increasing fibrosis replacement[15, 72]; and 3) *tensor mode,* a dimensionless measure ranging from [-1,1], which gauges the type of tissue anisotropy. Mode values near +1 indicate linear anisotropic diffusive structures, values near -1 indicate planar anisotropic diffusive structures, and values near zero indicate orthotropic diffusion and either sheet-like structures.

Although, tensor invariants provide insight to microstructural remodeling and have been validated as biomarkers for cell density in the brain[14] and fibrosis replacement in the heart[72], the specific microstructural changes that contribute to the observed changes in the diffusion tensor invariants of failing hearts remains incompletely understood. Additionally, the classic Stejskal-Tanner equation for the diffusion weighted MRI is limited in its assumption of a single compartment of diffusion within each imaging voxel. However, myocardial tissue has two main compartments of diffusion: the intracellular space and extracellular space. Previous diffusion based MRI studies defined a mathematical two-compartment models of restricted diffusion[78, 79]. Specifically, the Kärger model[79] mathematically describes a two-compartment model of diffusion for long cylinders packed in space to mimic the intracellular and extracellular diffusion in biological tissues. This model can provide insight about specific microstructural properties, including cell size, membrane permeability, cellular volume fraction, and intra- and extracellular

diffusivity[80-82] that impact local diffusion, and was used in this study to interpret the measured diffusion tensor and invariant data.

The objectives of this study were: 1) to quantify transmural microstructural remodeling in pacing induced, chronic compensated HF using DT-MRI; 2) to quantify microstructural differences between the paired transmural regions of normal and chronic compensated HF myocardium using DT-MRI; and 3) to use Kärger's model of two-compartment diffusion to implicate a specific form of microstructural remodeling in chronic compensated HF that is consistent with the measured diffusion tensor data. We hypothesize that pacing induced HF will result in significant microstructural remodeling as observed using DT-MRI invariants.

MATERIALS AND METHODS:

Rabbit Heart Preparation

Animal handling and care followed the recommendations of the National Institutes of Health Guide for the Care and Use of Laboratory Animals and the Institutional Animal Care and Use Committee at the University of California, Los Angeles; Indiana University School of Medicine; and Methodist Research Institute. Surgery protocols used to induce HF were in accordance with the guidelines set by the Indiana University School of Medicine. The University of California, Los Angeles Chancellor's Animal Research Committee approved animal protocols for ex vivo tissue evaluation.

Seven (N=7) 10-12 month old New Zealand white female rabbits (3.5-4.0 kg) underwent rapid ventricular pacing to induce HF. Rabbits were masked with isoflurane and additional anesthesia of ketamine (10 mg/kg) and xylazine (3 mg/kg) was administered intravenously through the ear. After a left lateral thoracotomy, an epicardial pacing lead was placed in the

lateral LV wall and connected to a modified single chamber ventricular pacemaker (Kappa or Enpulse pacemaker, Medtronic, Inc., Minneapolis, MN, USA) for tachycardia pacing. After one week of convalescence, the ventricles were paced at 250 beats per minute (bpm) for three days, 300 bpm for three days, and 350 bpm for 3-4 weeks to induce HF. After sufficient tachycardia pacing, the rabbits were anesthetized with ketamine (10 mg/kg) and xylazine (3 mg/kg), the chest was opened, and the rabbits were euthanized by removal of the heart. Five (N=5) normal weight matched New Zealand white female rabbits served as the control group (CNTL) and underwent identical sacrifice and heart excision procedures without the pacing protocol.

Each heart was excised by cutting the great cardiac vessels, rinsed with saline and suspended with suture by the aortic root in a formalin filled container. This resulted in tissue fixation in an unloaded, approximately end diastolic reference state. After two to three weeks of formalin fixation, a high viscosity silicone rubber injection compound (Ready-Press Polyvinylsiloxane, Microsonic Inc., Ambridge, PA) was first injected through the pulmonary vein to fill the left ventricle and left atrium, and then through the superior vena cava to fill the right ventricle and right atrium in order to maintain an approximate end diastolic cardiac anatomy during imaging[9]. The heart was then placed in a 250 mL plastic cylindrical container filled with a susceptibility-matched fluid (Fomblin Y-LVAC 6-06, Solvay Solexis, West Deptford, NJ). The heart was held in place within the container using open-cell foam and oriented to grossly align with the long axis of the container and subsequently the MRI scanner.

Diffusion Tensor Magnetic Resonance Imaging

A three-dimensional RARE diffusion weighted, fast spin echo pulse sequence was used to acquire diffusion tensor data on a 7 Tesla Bruker Biospin scanner (Bruker, Billerica, MA). The

following pulse sequence parameters were used: TE/TR = 30 ms/500 ms, two-fold RARE acceleration factor, 24 non-collinear diffusion gradient encoding directions, 6 non-diffusion weighted acquisitions, 25 G/cm gradient strength, gradient duration of 3.8 ms, gradient separation of 16.5 ms, resulting in a b-value = 1000 s/mm^2. The imaging resolution was 0.50 mm x 0.50 mm x 0.75 mm (~5,000 myocytes per voxel) obtained by using a 96 x 96 encoding matrix, 72-96 slices and a 48 x 48 x 54-72 mm imaging volume. The total imaging time for each diffusion weighted volume was 28.8 – 38.4 minutes, for a total DT-MRI acquisition time of 14:24-19:12 (HH:MM) per heart.

Diffusion tensors were reconstructed from the diffusion weighted images using linear regression and custom Matlab (The Mathworks, Natick, MA) code. The diffusion eigensystem and the three orthogonal tensor invariants (trace, FA, and mode)[10] were calculated for each imaging voxel's diffusion tensor. The shape of the diffusion profile was also rendered with superquadric glyphs, which are a function of the diffusion tensor's eigenvalues and help visualize the anisotropic nature of local diffusion[66].

Transmural Segmentation

The segmentation of the LV into three transmural regions (epicardium, midwall, and endocardium) was performed using custom Matlab code and is briefly described herein. First, the myocardium was segmented from background from the DT-MRI data using a custom graph-based semi-automatic segmentation method[96]. The right ventricle (RV) free wall was then removed from each short-axis slice while leaving the septal wall intact. Next, papillary muscles were removed from the LV. The percent wall depth was then calculated for each voxel based on the local myocardial wall thickness (i.e. the distance between the epicardial and endocardial

borders) with 0% and 100% defining the epicardial and endocardial borders respectively. To create the epicardium, midwall, and endocardial segments, voxels were divided into three equal zones based on the calculated percent wall depth.

Histological Analysis

Following the DT-MRI studies, 2 mm short axis slices were cut from the apical, mid-ventricular, and basal regions of each heart. The tissue samples were then processed routinely in graded alcohols, cleared in xylene, and embedded in paraffin. The samples were further microtome sectioned into 4 μm thick slices, placed on glass slides, and stained with Masson's trichrome for percent fibrosis analysis using optical imaging. From each of the apical, mid-ventricular, and basal short axis slices, fibrosis was observed from bright field microscopic images captured at 400x magnification. Three different fields of view (FOV) were imaged from each of the endocardial, midwall, and epicardial regions totaling nine digital images for each microtome section and 27 images per heart (3 FOVs x 3 transmural regions x 3 long axis regions). Percent fibrosis was quantified with a superimposed grid using Photoshop (Adobe, San Jose, CA). The number of grid squares containing blue stained tissue, signifying fibrosis, was divided by the total number of grid squares in the image to calculate the percent fibrosis in each FOV.

Kärger Model Sensitivity Analysis

Sensitivity analysis of the diffusion weighted signal to the microstructural properties of the tissue was performed by estimating the ratio of the diffusion weighted signal to the non-diffusion weighted signal (S/S_0) from the Kärger model using Equations 1-3 (see Appendix) and values

from the diffusion weighted imaging experiments (g = 25 G/cm, δ = 3.8 ms). The value of S/S_0 was then plotted as a function of each individual microstructural tissue property (D_i, D_e, κ, r, p_i, and p_e), while keeping the other microstructural tissue properties matched to normal myocardial values from literature ($D_i = 0.5 \times 10^{-3}$ mm^2/s, $D_e = 1.2 \times 10^{-3}$ mm^2/s, κ = 0.013 mm/s, r = 0.01 mm, $p_i = 0.75$, and $p_e = 0.25$) [19, 80, 109]. For example, when studying the sensitivity of the diffusion weighted signal to myocyte radius, S/S_0 was plotted as a function of myocyte radius ranging from 0 to 100 μm while keeping all other microstructural tissue property at their normal literature values.

Statistical Analysis

The use of inferential statistics requires statistically independent samples. The highly organized arrangement of myocytes within myocardium, however, results in high spatial correlation of the diffusive properties within myocardium and consequently to statistically non-independent local diffusion tensors and tensor invariants. To produce statistically independent data points – trace, FA, and mode were spatially de-correlated in three dimensions for each heart via decimation by each heart's auto-correlation length[97].

The standard formula-based statistical tests (e.g. t-test or ANOVA) require data to be approximately Gaussian in distribution and to have equal variances among populations. The distribution of tensor invariant data, however, is not Gaussian and has unequal variances across different populations[9]. Therefore, statistical significance tests were performed using bootstrap methods that are analogous to conventional approaches[97].

In order to visualize the distributions of tensor invariants between CNTL and HF groups as well as across transmural regions within groups, we produced bootstrapped histograms by

sampling 1000 times with replacement from the segmented and de-correlated data to define 95% confidence intervals (CIs) for each bin height. A lack of overlap in 95% CIs between segmented regions within a histogram bin indicates a statistically significant difference within the invariant range of that bin.

HF myocardium was compared to CNTL myocardium within each transmural region (epicardium, midwall, and endocardium) of the LV using a two-group comparison of the medians of the de-correlated data for each heart from both the DT invariant data and the histologic fibrosis data. To test whether DT invariants yielded significant differences across transmural regions within CNTL myocardium and within HF myocardium, we performed a bootstrap analog to repeated measures ANOVA of the de-correlated data from the pooled data sets for all three transmural regions. Values of $p < 0.05$ were regarded as statistically significant. Bootstrapped repeated measures ANOVA and two-group comparisons were performed using the R programming language (http://www.r-project.org).

When reporting image quality, auto-correlation, global LV dimensions, and percent fibrosis, results are reported as mean±SD. Ex vivo LV dimensions measured by DT-MRI were compared using a two-tailed unpaired t-test with $p < 0.05$ regarded as significant.

RESULTS:

Global Remodeling – Table 1 lists LV dimensions from CNTL and HF groups measured from DT-MRI. Interventricular septal (IVS) thickness (p=0.10) was not significantly different between CNTL and HF groups. LV posterior wall (LVPW) thickness (p=0.003) and LV end diastolic diameter (LVEDD) (p=0.002) were significantly larger in the HF group compared to CNTL. LV base to apex length measured from DT-MRI was significantly longer (p=0.002) in

the HF group than in the CNTL group. LV mass, measured by volume of myocardial voxels from DT-MRI multiplied by the density of myocardium (1.053 g/mL)[110], was significantly larger (p=0.0003) in the HF group than in the CNTL group. The global LV dimensional results suggest that chronic compensatory hypertrophy was achieved in the HF group.

Table 1: LV dimensions (mean±SD) measured from CNTL and HF groups from ex vivo DT-MRI (IVS: interventricular septum, LVPW: left ventricular posterior wall, LVEDD: left ventricular end-diastolic diameter)

	IVS (mm)	LVPW (mm)	LVEDD (mm)	Base to Apex (mm)	LV Mass (g)
CNTL	3.7±0.5	4.1±0.3	9.1±1.2	24.3±1.7	4.4±0.2
HF	4.5±1.0	5.3±0.6	11.6±0.9	28.6±1.5	6.4±0.8

Microstructural Remodeling – Figure 1 depicts Masson's trichrome stained myocardial short axis slices (Figures 1A and 1E) and corresponding DT invariant maps from a single representative CNTL heart and single HF heart. A higher trace is qualitatively visible in the HF heart (Figure 1F) when compared to the normal heart (Figure 1B), whereas changes in FA (Figures 1C and 1G) and mode (Figures 1D and 1H) are not qualitatively apparent.

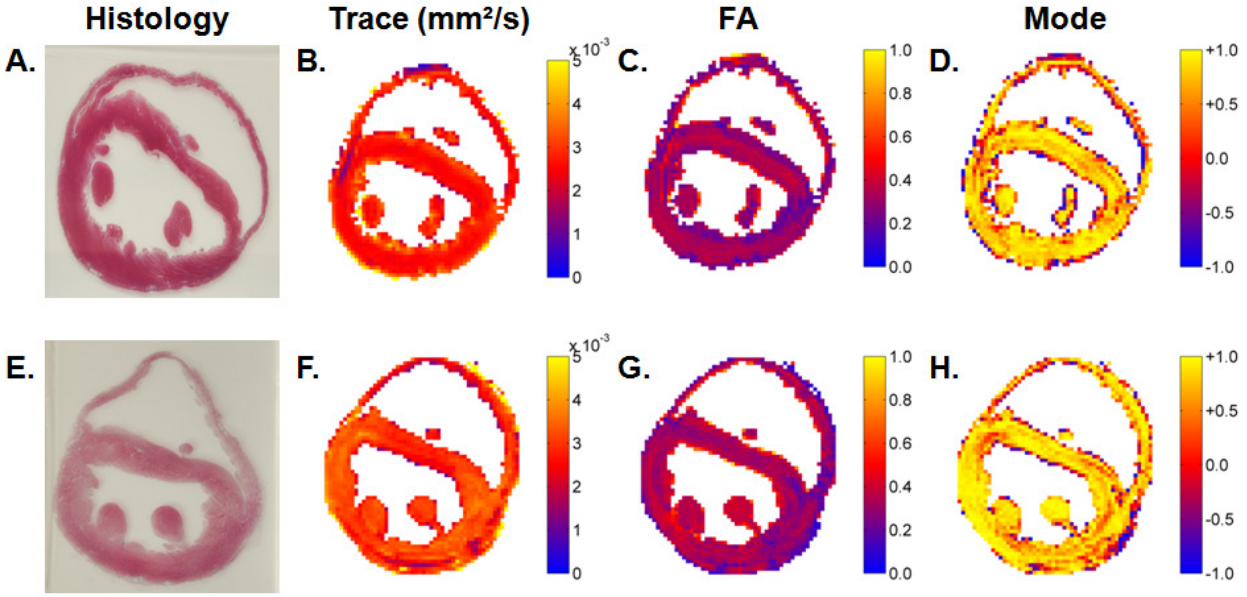

Figure 1: Mid-ventricular short axis trichrome stained histology (A and E) and DT invariant maps trace (B and F), FA (C and G) and mode (D and H) for a single CNTL (A-D) and single HF (E-H) heart.

Diffusion tensor shape rendered with superquadric glyphs is shown in Figure 2 at every myocardial voxel for the corresponding CNTL and HF short axis slices from Figure 1. Glyphs are color coded to represent primary eigenvector direction where red corresponds to the x-direction, green corresponds to the y-direction, and blue corresponds to the z-direction (out-of-plane). Due to an increased trace in the HF heart, glyphs are noticeably larger in the HF short axis slice than the CNTL slice.

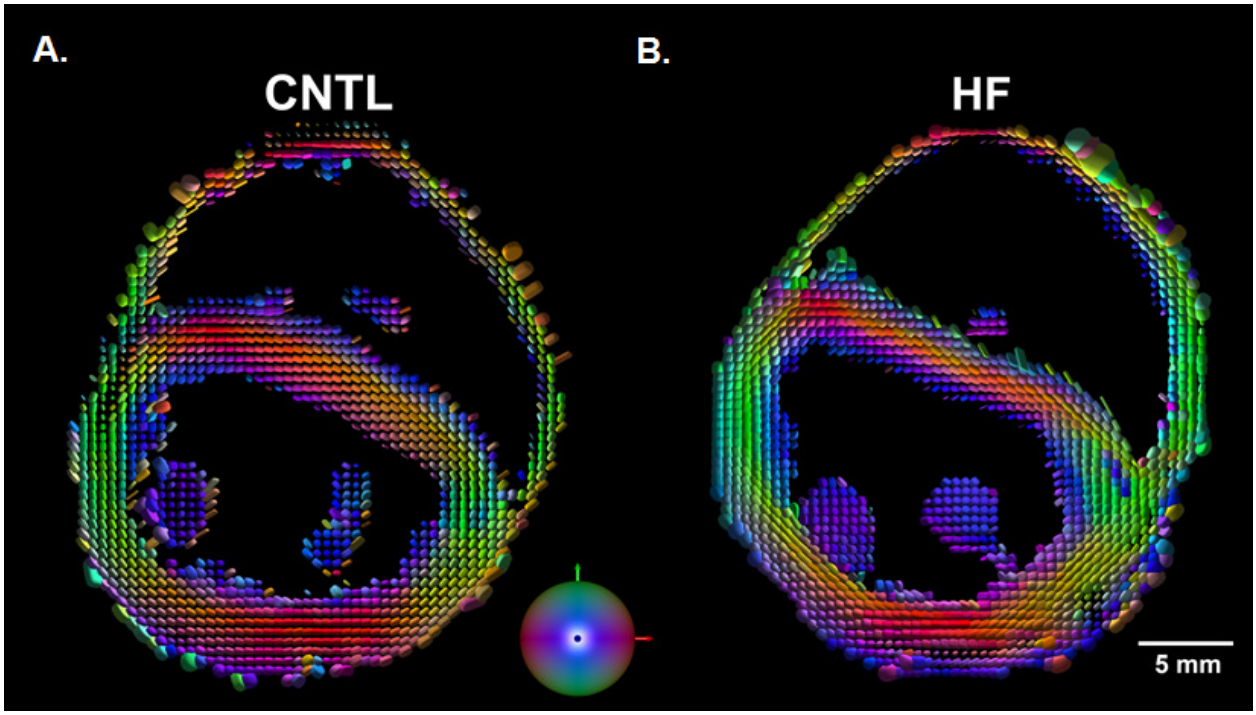

Figure 2: Diffusion tensor shape and direction rendered with superquadric glyphs at every myocardial voxel for the corresponding (A) CNTL and (B) HF short axis slices from Figure 2. Glyphs are color coded to represent primary eigenvector direction where red corresponds to the

x-direction, green corresponds to the y-direction, and blue corresponds to the z-direction (out-of-plane). Due to an increased trace in the HF heart, the glyphs appear larger in the HF short axis slice than the CNTL slice. The images are scaled identically.

Bootstrapped histograms with 95%-CIs are depicted in Figure 3 for de-correlated invariant data from all hearts in CNTL and HF groups segmented transmurally into epicardial (Figures 3A-C), midwall (Figures 3D-F), and endocardial (Figures 3G-I) regions. Two-group comparison of the medians demonstrates a significant increase in trace for HF compared to CNTL myocardium in epicardial ($p = 0.006$), midwall ($p = 0.008$), and endocardial regions ($p = 0.039$). FA appears to decrease slightly in all transmural regions for HF hearts, however, the apparent decreases in FA are not statistically significant. Mode is not statistically different between CNTL and HF myocardium in epicardium, however, HF myocardium is characterized by a decrease in mode in the midwall ($p = 0.038$) and an increase in mode in the endocardium ($p = 0.041$). DT invariant medians and 95% CIs of the de-correlated invariant data for transmurally segmented CNTL and HF myocardium are listed in Table 2.

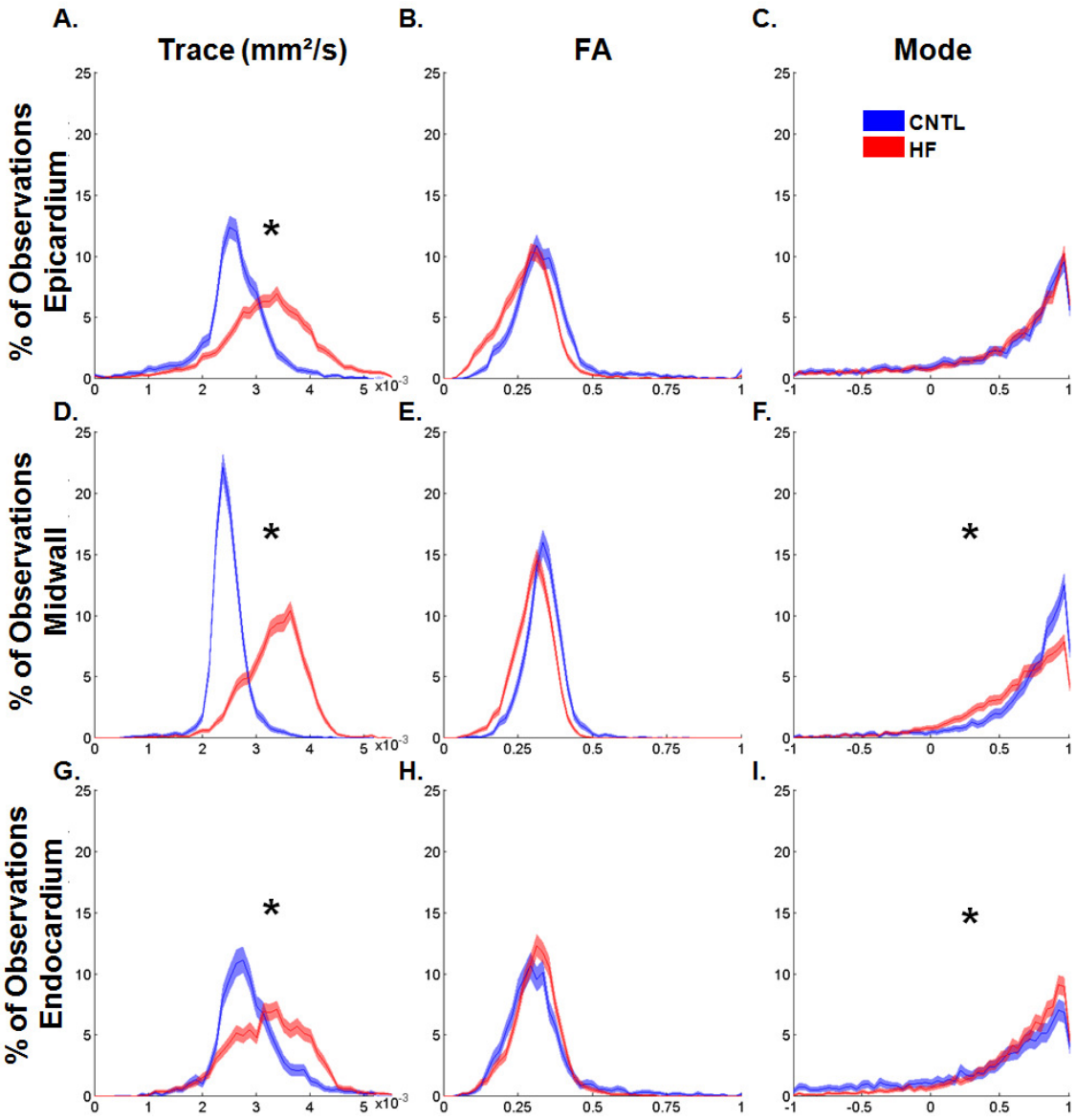

Figure 3: Bootstrapped histograms with 95%-CIs of CNTL (blue) and HF (red) groups using de-correlated data for trace (A, D, and G), FA (B, E, and H), and mode (C, F, and I) in epicardial (A-C), midwall (D-F), and endocardial (G-I) regions. Invariant histograms labeled with "*" signify a statistically significant shift in median value from CNTL to HF. An increase in trace is significant in all transmural regions (all $p < 0.04$) in HF compared to CNTL. A decrease in mode is significant ($p = 0.04$) in midwall HF compared to midwall CNTL. An increase in mode is significant ($p = 0.04$) in endocardial HF compared to endocardial CNTL.

Table 2: Tensor invariant medians, 95%-CIs of bootstrapped medians, and 95%-CIs of de-correlated invariant data for transmurally segmented CNTL and HF LV myocardium

	Trace (x10^{-3} mm^2/s)			FA			Mode		
	Epicardium	**Midwall**	**Endocardium**	**Epicardium**	**Midwall**	**Endocardium**	**Epicardium**	**Midwall**	**Endocardium**
CNTL:									
median	2.6	2.4	2.8	0.324	0.334	0.301	0.710	0.805	0.620
95% CI - median	[2.58, 2.61]	[2.43, 2.45]	[2.78, 2.82]	[0.321, 0.328]	[0.332, 0.336]	[0.297, 0.303]	[0.691, 0.726]	[0.796, 0.815]	[0.600, 0.640]
95% CI	[0.94, 3.92]	[1.81, 3.25]	[1.74, 4.53]	[0.159, 0.706]	[0.203, 0.467]	[0.145, 0.678]	[-0.812, 0.991]	[0.448, 0.993]	[-0.850, 0.988]
HF:									
median	3.3	3.4	3.3	0.287	0.305	0.313	0.714	0.685	0.719
95% CI - median	[3.24, 3.29]	[3.36, 3.40]	[3.23, 3.28]	[0.285, 0.289]	[0.303, 0.307]	[0.310, 0.315]	[0.703, 0.725]	[0.674, 0.694]	[0.708, 0.730]
95% CI	[1.29, 5.40]	[2.17, 4.26]	[1.73, 4.67]	[0.103, 0.484]	[0.158, 0.409]	[0.142, 0.465]	[-0.784, 0.992]	[-0.378, 0.987]	[-0.507, 0.984]

Figure 4 depicts bootstrapped histograms comparing tensor invariants across transmural regions in CNTL (Figure 4A-C) and HF (Figures 4D-F) myocardium. Results from the bootstrapped ANOVA testing reveal significant differences across epicardial, midwall, and endocardial regions for all hearts when comparing trace ($p<0.0001$), FA ($p<0.0001$), and mode (CNTL: $p<0.0001$, HF: $p=0.001$). Trace is significantly lower in the midwall of CNTL hearts than in the epicardium and endocardium (both $p<0.001$) according to two region bootstrapped ANOVAs. The trace is also lower in the epicardium than in the endocardium ($p<0.0001$). The distribution of trace from CNTL hearts is much narrower in the midwall signifying more consistent mean diffusivity. The lower trace in the midwall of CNTL hearts is not observed in the HF hearts. In fact, trace is higher in the midwall of HF hearts than in the epicardium and endocardium (both $p<0.001$) of HF hearts. Trace is not significantly different between endocardial and epicardial regions in HF hearts ($p=0.59$). The FA in the midwall of CNTL hearts is higher than in the epicardium and endocardium (both $p<0.0001$). FA is also lower in the endocardium than in the epicardium ($p<0.0001$). The distribution of FA from CNTL hearts is narrower in the midwall signifying more consistent diffusion anisotropy. In the HF group, FA is significantly lower in the epicardium than in the midwall and endocardium (both $p<0.0001$), while FA is slightly higher in the endocardium than in the midwall ($p=0.002$). The distribution of mode from CNTL hearts skews the most towards +1 (linear anisotropy or fiber-like structures) in the midwall, less so in epicardium, and least in the endocardium. Thus, mode in CNTL midwall is higher than in epicardial and endocardial regions (both $p<0.0001$), and mode in the epicardium is higher than in the endocardium ($p<0.001$). In the HF group, the mode in the midwall skews the least towards +1 and is thus lower than the mode in the epicardium ($p=0.0007$) and endocardium ($p=0.007$). There is no significant difference in mode between

epicardial and endocardial regions (p=0.71). Overall, this represents a significant loss of the transmural gradient in mode in HF compared to CNTL.

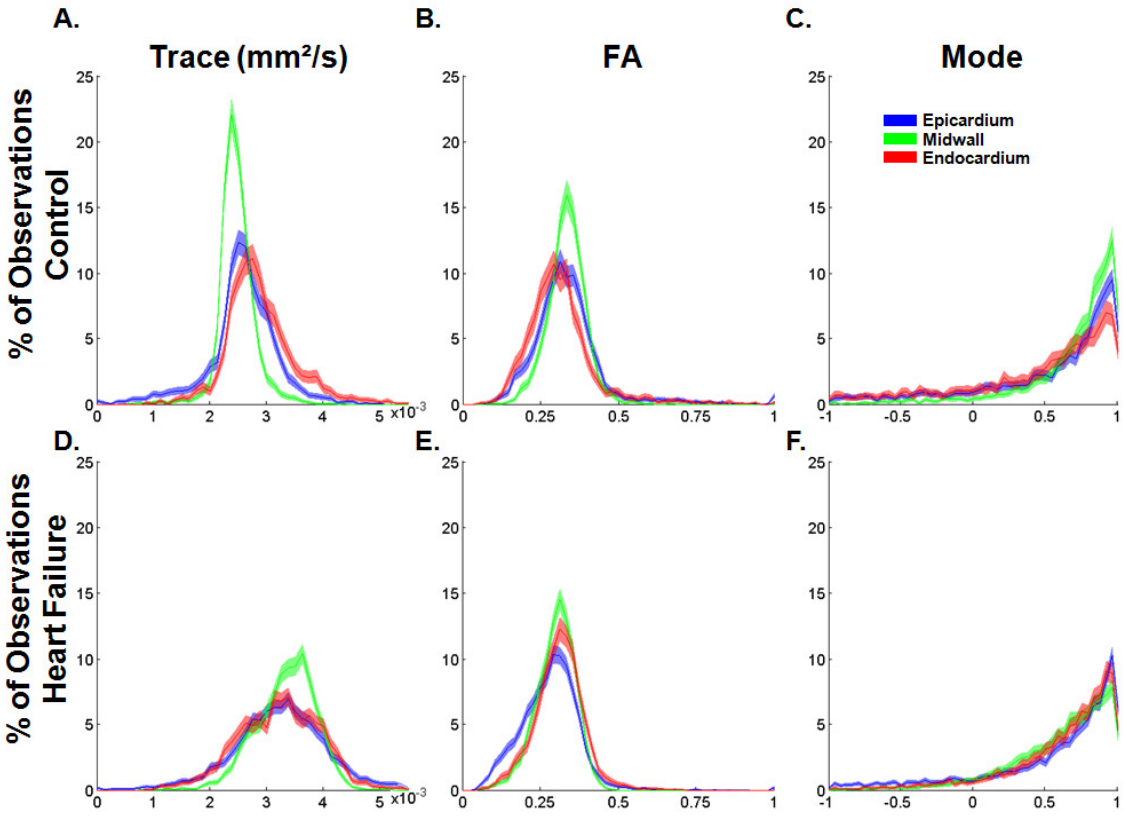

Figure 4: Bootstrapped histograms with 95%-CIs of CNTL (A-C) and HF (D-F) groups using de-correlated data for trace (A and D), FA (B and E), and mode (C and F) in epicardial (blue), midwall (green), and endocardial (red) regions. Transmural region effects were significant for all DT invariants in CNTL and HF groups according to repeated measures ANOVA (all $p \leq 0.001$).

Percent fibrosis measured with histology are listed in Table 3 and summarized as median±SD of the percent fibrosis in CNTL and HF groups for each transmural region and the composite LV myocardium. Percent fibrosis values are not significantly different between CNTL and HF groups in any transmural region or in the LV myocardium as a whole as confirmed by two-group

comparisons of the medians (all p>0.05). Figure 5 depicts histological slices viewed at 400x magnification from representative samples of the CNTL and HF groups.

Table 3: Percent fibrosis (median±SD) as a percentage of total myocardium in endocardial, midwall, and epicardial regions and the overall LV. † Indicates a lack of statistical significance between HF and CNTL.

	Endocardium	Midwall	Epicardium	Overall
CNTL	3.2±1.6%	3.5±1.4%	3.8±1.4%	3.5±1.5%
HF	4.5±3.9% †	4.8±4.2% †	4.9±6.1% †	4.8±4.8% †

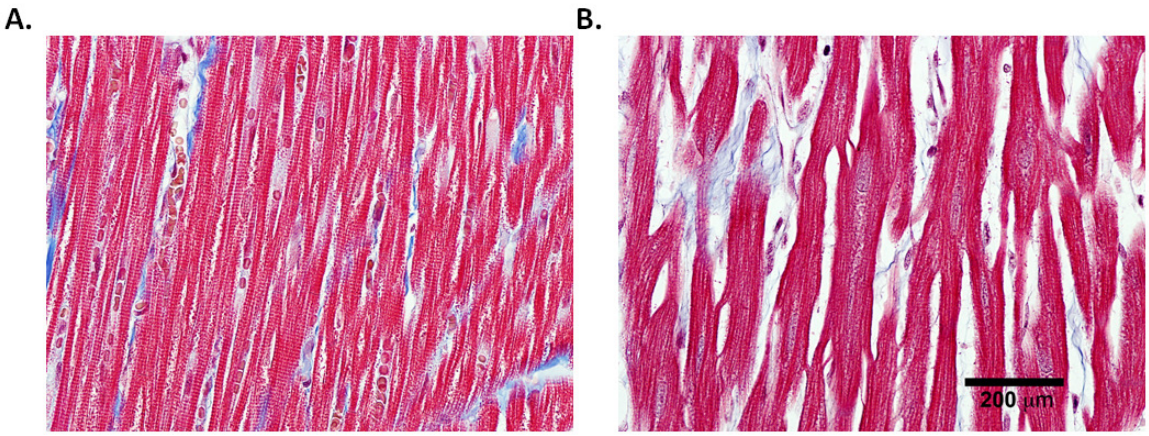

Figure 5: High magnification view (400x) of Masson's trichrome staining of 4 µm thick microtome cut slices from a single heart from the (A) CNTL and (B) HF groups. Percent fibrosis values are not statistically different in the HF group (5±5%) versus the CNTL group (4±2%).

Kärger Model Sensitivity Analysis

The results of the Kärger sensitivity analysis are depicted in Figure 6. The theoretical ratio of the non-diffusion weighted signal to the diffusion weighted signal (S/S_0) as defined by the Kärger model is plotted against myocyte radius (Figure 6A), myocyte membrane permeability (Figure 6B), extracellular volume fraction (Figure 6C), extracellular diffusivity (Figure 6D), and

intracellular diffusivity (Figure 6E). S/S_0 is plotted against the logarithmic scale of each physiological input except for extracellular volume fraction. The range of values chosen for each x-axis in Figure 6 represents an extreme range of physiological properties to encapsulate the widest range of remodeling possibilities. Myocyte radius is depicted at values from 0.0001 – 0.1 mm (Figure 6A), while literature reports a normal value of 0.01 mm; membrane permeability is depicted at values from 0.0001 – 1 mm/s (Figure 6B), while literature reports a normal value of 0.013 mm/s; extracellular volume fraction is depicted at values from 0 – 1 (Figure 6C), while literature reports a normal value of 0.25; extracellular diffusivity is depicted at values from 0 – 0.01 mm^2/s (Figure 6D), while literature reports a normal value of 0.0005 mm^2/s[109]; and intracellular diffusivity is depicted at values from 0 – 0.01 mm^2/s (Figure 6E), while literature reports a normal value of 0.0012 mm^2/s[109]. Diffusion tensor experiments performed using the parameters in our experiments are insensitive to remodeling due to myocyte radius and membrane permeability as S/S_0 does not change across the range of radii and permeability values (Figures 6A and 6B). S/S_0 decreases, signifying an increase in overall mean diffusivity and trace, as a function of an increasing extracellular volume fraction, extracellular diffusivity, and intracellular diffusivity (Figures 6C-D).

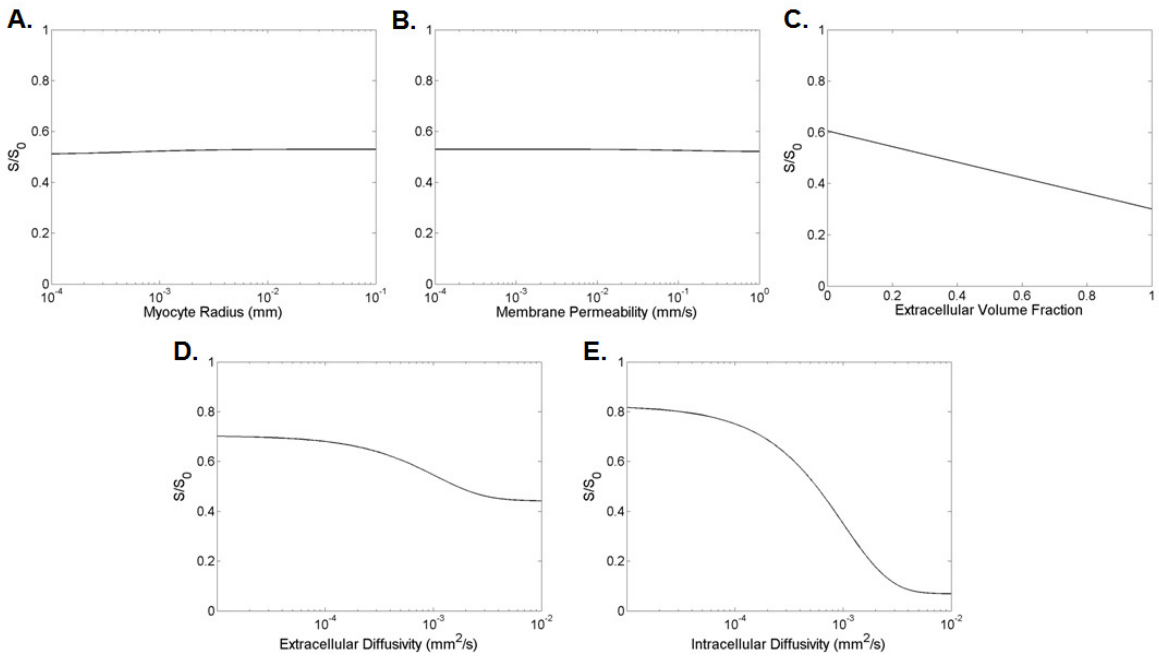

Figure 6: Theoretical ratio of diffusion weighted to non-diffusion weighted signal intensity (S/S_0) from the Kärger model as a function of physiological inputs: (A) myocyte radius, (B) membrane permeability, (C) extracellular volume fraction, (D) extracellular diffusivity, and (E) intracellular diffusivity. S/S_0 is plotted against the semi-logarithmic scale of each physiological property except for extracellular volume fraction.

DISCUSSION

In the pacing induced chronic compensated HF rabbit model, we have observed a significant increase in trace in all transmural regions, a significant decrease in tensor mode in the midwall, a significant increase in tensor mode in the endocardium, and a significant loss of transmural gradient in mode when compared to normal myocardium. Additionally, we have observed no significant changes in FA in HF myocardium, which is confirmed by no significant changes in percent fibrosis when compared to normal myocardium with histology.

Microstructural remodeling in HF has been extensively studied previously, primarily using histological methods to measure myocyte size and percent fibrosis. Myocyte lengthening and hypertrophy have been well documented in the different stages of HF[11, 111, 112]. Inferring any correlation to changes between trace from HF myocardium and changes in myocyte size would require further histological validation. Instead, we used the Kärger model to evaluate the microstructural changes that may account for the significant increase in trace in HF. Under the experimental parameters used in this DT-MRI study, changes in the ratio of the diffusion weighted signal to the non-diffusion weighted signal (S/S_0) are insensitive to changes in myocyte radius and membrane permeability (Figures 6A and 6B). It is apparent that changes to S/S_0 are most sensitive to changes in the intrinsic intracellular diffusivity, followed by the extracellular diffusivity and the cellular and extracellular volume fractions. However, due to the small changes in histologically observed levels in percent fibrosis between normal and pacing induced HF myocardium and the concomitant consistency in the extracellular volume, the component of microstructural remodeling that likely contributes to the observed changes in the diffusion weighted signal may arise from remodeling of the intracellular and extracellular constituents as opposed to changes in intracellular and extracellular volume fraction. Intracellular remodeling has been documented in the pathophysiology of HF, wherein mitochondria and nuclei enlarge and myofibril alignment changes within the myocytes[37]. Changes in the orientation of contractile proteins and cytoskeletal structures have also been observed in HF[113, 114]. Additionally, changes in extracellular composition, including the ratio of collagen types and loss of collagen struts, have been observed in cases of HF without changes in overall fibrosis percentage[18, 40]. The physiological implication of the observed transmural gradient in trace for

CNTL myocardium is unknown, but unlikely to arise as a direct result of changes in myocyte radius or membrane permeability.

The use of the Kärger model in this study provides a high level, first pass insight into possible components of microstructural remodeling that may lead to the observed increases in trace. The microstructural remodeling process is complicated and likely includes many simultaneous changes in various physiological properties (e.g. intracellular and extracellular remodeling, along with changes in myocyte diameter and membrane permeability). Direct histological measures of myocyte radius, membrane permeability, extracellular volume fraction, and intra- and extracellular characteristics would further elucidate the correlations between microstructural remodeling and changes in DT-MRI measures.

Volume overloading leading to compensated concentric hypertrophy has previously been shown to yield little change in fibrosis replacement[18, 40]. In another canine model of HF that used 12 weeks of rapid atrial pacing, Lin et al. reported an increase in fibrosis from 3% in normal myocardium to 8% in the lateral wall of paced myocardium and an increase of 3% to 4% in the septal wall[41]. Additionally, in the chronic de-compensated stage of HF in a canine model, Kajstura et al. reported a 6% fibrosis level in the LV wall[11]. Both studies yield results within one SD of the mean percent fibrosis results of this study. Myocardial fibrosis has been shown to be negatively correlated with FA because the collagen network in fibrotic tissue provides a more homogeneous and isotropic environment for diffusion compared to the highly organized myofiber and myolaminar structures in healthy myocardium[15, 72]. Thus, the subtle, albeit not significant, decrease in FA observed in the epicardium and midwall of the HF data is consistent with the subtle increase in median fibrosis level in HF (5±5%) compared to CNTL (4±2%) as measured by histology. Previous studies have also observed the transmural gradient of fibrosis

as measured by FA. Jiang et al. observed a transmural gradient of decreasing FA in the normal sheep LV traveling from epicardial to endocardial regions[115]. Wu et al. reported lowest FA values in the endocardium of normal porcine hearts relative to other transmural regions and a trend of decreasing FA from epicardium to endocardium in myocardium remote from the infarct, but did not report whether these transmural differences were statistically significant[73]. The results from our study reveal the lowest values of FA in CNTL endocardium, which agrees with previous observations from Jiang et al. and Wu et al., as well as histological observations of a higher fibrosis level in the endocardium[116]. However, we did not observe a transmural gradient of decreasing FA from epicardium to endocardium as the midwall of our normal rabbits yielded the highest values of FA.

HF revealed a shift in the histogram's skewness away from a mode value of +1 in the midwall and an increase in skewness towards +1 in the endocardium when compared to normal myocardium, while revealing no significant difference in mode in the epicardium. The shift in skewness away from a mode value of +1 indicates a loss of linear anisotropy, or fiber-like diffusion, and toward an increase in orthotropic (book-like) or planar anisotropic (pancake-like) diffusion. The physiological implication of this effect could be an increase in the presence of myofiber disarray, which has been observed in the hypertrophic heart[17]. An increase in the skewness of mode towards +1 would physiologically imply a deterioration of sheet-like structures into more isolated myofibers (linear anisotropic structures). Additionally, the loss of a transmural gradient in mode values in HF implies more homogeneous composition of fiber and sheet-like structures when compared to normal myocardium, which may contribute to dysfunction in HF. In fact, a loss of a transmural gradient in myofiber diameter has been observed in cases of hypertrophic cardiomyopathy[77]. However, correlations of mode to the fiber

and sheet microstructure of the heart measured with histology have not been made and further study is needed.

In conclusion, DT invariant data identify statistically significant microstructural remodeling in the pacing induced model of compensated HF within epicardial, midwall, and endocardial regions as well as the transmural heterogeneity of microstructure within both CNTL and HF myocardium. DT invariant data provides information on the specific form of pathophysiological microstructural remodeling and provides insight into the components of microstructural remodeling that may contribute to mechanical and electrical dysfunction in HF.

Appendix

Kärger Model Sensitivity Analysis

The assumptions of the Kärger model are two-fold: 1) there are two distinct molecular spin-carrying compartments (intracellular and extracellular) within the imaging voxel; and 2) the diffusion of the spin-carrying molecules follows a Gaussian distribution[79]. In this model, the signal from a diffusion weighted magnetic resonance experiment is dependent on the intrinsic physiological characteristics of the underlying microstructure, which include the intrinsic intracellular (D_i) and extracellular (D_e) diffusivities, membrane permeability (κ), cell radius (r), cellular volume fraction (p_i), and extracellular volume fraction (p_e). Other experimental factors that govern the magnitude of the diffusion signal include the b-value (b), diffusion gradient strength (g), diffusion gradient duration (δ), and the gyromagnetic ratio (γ). The Kärger model equates the ratio of the diffusion weighted signal (S) to the non-diffusion weighted signal (S_0) using a two-compartment model:

$$S / S_0 = p_A e^{(-bD_A)} + p_B e^{(-bD_B)} \quad (1)$$

Where p_A and p_B are the apparent cellular and extracellular volume fractions and D_A and D_B are the apparent intracellular and extracellular diffusivities. It is important to note that these apparent coefficients (p_A, p_B, D_A, D_B) are related to the actual parameters of intracellular volume fraction (p_i), extracellular volume fraction (p_e), intracellular diffusivity (D_i), and extracellular diffusivity (D_e) as governed by the Kärger equations:

$$D_{A,B} = \frac{1}{2}\left\{ D_i + D_e + \frac{1}{\gamma^2 \delta^2 g^2}\left(\frac{1}{\tau_i} + \frac{1}{\tau_e}\right) \pm \ldots \right.$$

$$\left. \left[\left[D_e - D_i + \frac{1}{\gamma^2 \delta^2 g^2}\left(\frac{1}{\tau_e} - \frac{1}{\tau_i}\right) \right]^2 + \frac{4}{\gamma^4 \delta^4 g^4 \tau_i \tau_e} \right]^{1/2} \right\}$$

$$p_A = 1 - p_B \ , \ p_B = \frac{p_i D_i + p_e D_e - D_A}{D_B - D_A} \tag{2}$$

Where τ_i and τ_e are intracellular and extracellular exchange times governed by [80]:

$$\tau_i = \frac{r^2}{8 D_i} + \frac{r}{2\kappa} \ , \ \tau_e = \frac{p_e}{p_i}\tau_i \tag{3}$$

The Kärger model thus allows for the inference of physiological properties of cells and tissues from the measured diffusion weighted signal.

CHAPTER 6

Conclusion

The complex, but highly organized arrangement of myocytes within the left ventricle (LV) underlies the anisotropic mechanical[21-23, 83] and electrical[27, 28] function of the heart. Cardiomyopathies, including heart failure and infarction, disrupt the myofiber and myolaminar structure as myocytes change shape or undergo fibrosis replacement, which disrupts function, leads to an increased incidence of arrhythmia[33, 34], and foments overt heart failure. Whole heart surveys of microstructural remodeling are critical to our basic science understanding of cardiac pathophysiology. Recently, diffusion tensor magnetic resonance imaging (DT-MRI) has emerged as a means for quantifying global and regional microstructural remodeling[16, 72, 74, 117].

Previous observations of myocardial microstructure have predominantly relied on histological methods[21, 22, 25, 26, 29, 67], which are exceedingly tedious and difficult to spatially register in three-dimensions (3D). DT-MRI enables the 3D evaluation of whole heart microstructure. The eigenvectors of the diffusion tensor contain the orientation information of diffusion within the tissue microstructure. It is well established that the local long axis of the myocytes corresponds to the direction of the primary eigenvector of the diffusion tensor[2, 4-6, 9]. The myolaminar sheet orientations have been shown to correspond to the secondary eigenvector direction[2-7]. Meanwhile, the eigenvalues quantify the magnitude of diffusion along each eigenvector and characterize the overall shape of diffusion. DT invariants (e.g. trace, fractional anisotropy, or mode), which are functions of the eigenvalues alone, saliently characterize specific attributes of tensor shape and can be used to evaluate microstructural remodeling by quantifying cellularity (increases with decreasing tensor trace), fibrosis (increases with

decreasing fractional anisotropy, FA), and tissue mode (increase in fiber disarray with decreasing tensor mode)[10]. The achievements of the work described in this dissertation have 1) established the correspondence between histological and DT-MRI estimates of myolaminar sheet orientation in healthy myocardium; 2) quantified microstructural remodeling in myocardial infarction and its border zone using DT-MRI; and 3) quantified myocardial microstructural remodeling in heart failure using DT-MRI.

Myocardial Sheet Orientations Measured by DT-MRI

We established the correspondence between the two histologically observable and DT-MRI measurements of myolaminae orientation for the first time and showed that single myolaminar orientations observed in local histology may result from histological artifact.

DT-MRI was performed on six sheep left ventricles (LV), then corresponding direct histological transmural measurements were made within the antero-basal and lateral-equatorial LV. Secondary and tertiary eigenvectors of the diffusion tensor were compared to each of the two locally observable sheet orientations from histology. Diffusion tensor invariants were calculated to compare differences in microstructural diffusive properties between histological locations with one observable sheet population and two observable sheet populations.

Mean difference ± one standard deviation between DT-MRI and histology measured sheet angles was 8°±27°. Diffusion tensor invariants showed no significant differences between histological locations with one observable sheet population and locations with two observable sheet populations.

DT-MRI measurements of myolaminae orientations derived from the secondary and tertiary eigenvectors correspond to each of the two local myolaminae orientations observed in histology.

Additionally, two local sheet populations may exist throughout LV myocardium and one local sheet population observed in histology may be a result of preparation artifact.

Microstructural Border Zone Remodeling in the Post-Infarct Porcine Heart Measured with DT-MRI

We used late gadolinium enhanced (LGE) MRI in post-infarct porcine hearts to segment remote, border zone (BZ), and infarcted myocardium, and then quantified microstructural remodeling in the BZ and infarcted regions using diffusion tensor MRI (DT-MRI).

Chronic porcine infarcts were created by balloon occlusion of the LCx. 6-8 weeks post infarction the hearts were excised after contrast administration and imaged with LGE MRI (0.33x0.33x0.33-0.50mm) and co-registered DT-MRI (1x1x3mm). Myocardium was segmented as remote, BZ, or infarct by LGE signal intensity thresholds. Diffusion tensor invariants were used to evaluate microstructural remodeling by quantifying trace, fractional anisotropy (FA), and tissue mode.

The BZ significantly remodeled compared to both infarct and remote myocardium; and demonstrated a decrease in cellularity (trace increase), decrease in tissue organization (FA decrease), and an increase in fiber disarray (mode decrease) relative to remote myocardium (all $p<0.05$). Microstructural remodeling in the infarct was significantly larger (all $p<0.05$).

LGE segmentation of DT-MRI data identifies regions of significant microstructural remodeling in both the BZ and infarct region relative to remote and normal myocardium. The large increase in trace and decrease in FA in the infarct indicates a significant increase in replacement fibrosis and a decrease in cellularity. The intermediate increase in trace and decrease in FA in the BZ suggest a unique intra-voxel mixture of fibrosis and viable myocytes. Hence, the

BZ is a unique microstructural environment, which may explain its importance in ventricular arrhythmogenesis.

Microstructure in Pacing Induced Heart Failure Measured by DT-MRI

We used DT-MRI to quantify transmural specific microstructural remodeling between myocardium from normal rabbits and rabbits with pacing induced heart failure (HF).

HF was induced in New Zealand White female rabbits with an epicardial pacing lead placed in the lateral LV wall for tachycardial pacing. Normal weight matched rabbits served as controls (CNTL). Hearts were excised, formalin fixed, and DT-MRI was performed at 0.50x0.50x0.75 mm^3. Diffusion tensor invariants were used to evaluate microstructural remodeling in epicardial, midwall, and endocardial regions by quantifying trace, fractional anisotropy (FA), and tissue mode.

Trace significantly increased from CNTL to HF in all transmural regions (all $p < 0.04$). FA differences from CNTL to HF were insignificant in all regions. Mode significantly decreased in midwall ($p = 0.04$) and increased in endocardium ($p = 0.04$) from CNTL to HF but did not significantly shift in epicardium. When testing for within CNTL or within HF group differences, all invariants exhibited significant region effects (all $p \leq 0.001$) signifying transmural heterogeneity of microstructure within each group.

DT invariant data indentify statistically significant microstructural remodeling in the pacing induced model of compensated HF within epicardial, midwall, and endocardial regions as well as transmural heterogeneity of microstructure within both CNTL and HF myocardium. DT invariant data provides information on the specific pathophysiological remodeling of the

microstructure which can provide insight into the disruption of mechanical and electrical function involved in HF.

CHAPTER 7

The Future Outlook of Myocardial Microstructural Evaluation Using Diffusion Based Imaging

The work in this dissertation has proven the value of DT-MRI for the evaluation of myocardial microstructure. DT-MRI is an especially attractive method to measure microstructural characteristics due to its simplicity in imaging preparation, tensor reconstruction, and tensor analysis. We have provided a practical toolset utilizing the diffusion tensor eigenvectors and eigenvalues in the form of tensor invariants to evaluate myocardial microstructure in health and disease.

Specific correspondence between DT-MRI data (e.g. trace, FA, and mode) and histological measures of myocardial microstructure (e.g. myocyte size, collagen volume fraction, and myofiber disarray) are still in nascent stages of research. Although the correlation between FA and collagen volume fraction or fibrosis percentage has been well documented in myocardium, exact correlations between trace and mode with histological measures of microstructure have not been fully investigated. Further research in this area is a natural extension of the work achieved in this dissertation and may include correlation between trace and histological measures of myocyte size, organelle size, composition of collagen types in the extracellular space; as well as correlation between mode and histological measures of myofiber disarray and sheet organization.

Additionally, standard diffusion tensor analysis restricts the eigensystem to three orthogonal eigenvectors thus limiting the directions of maximal diffusion. It is known that the direction of maximal diffusion lies in the myofiber axis and the direction of secondary diffusion lies in the myolaminar sheet direction, which lies transverse to the myofiber axis. We have shown that dual

sheet orientations exist in local myocardial microstructure thus the direction of secondary and tertiary levels of diffusion would lie in the dual sheet axes, however these directions have no physiological basis of orthogonality. In fact, we have measured bimodal sheet orientations histologically to be separated by 84°. More advanced methods of diffusion based MRI exist that have no such limitations in orthogonality of diffusion axes. Fourth order diffusion tensors, diffusion spectral imaging, q-ball imaging, high angular resolution diffusion imaging, and diffusion orientation transform methods all utilize the reconstruction of multiple axes of distinct diffusion beyond the three orthogonal directions of standard DT-MRI. Although more detailed and accurate characterizations of myocardial microstructure may be possible with these methods, they require prohibitively longer scan times and more complicated reconstruction methods. Such methods are in nascent stages of use in myocardial applications and would be a natural extension of the work presented in this dissertation.

Another natural extension of this work would be the pursuit of in vivo DT-MRI data to evaluate myocardial microstructure in live specimens. However, due to the bulk motion of the myocardium due to breathing and heartbeat, as well as bulk fluid motion within the myocardium due to blood flow, achieving reproducible DT-MRI data in the heart in vivo is extremely challenging. Breath-holding, synchronized breathing, and retrospective navigators have been implemented to account for respiratory motion in DT-MRI experiments. Another challenge in acquiring in vivo DT-MRI data is the constraint of acquisition time. High resolution ex vivo DT-MRI experiments often exceed 8 hours of acquisition time, but with in vivo experiments, acquisition time is limited to under an hour, significantly reducing the resolution of in vivo data.

These are the challenges currently being faced that require sufficient research to further the understanding of DT-MRI data in evaluating myocardial microstructure. Continued research in

this field will eventually maximize the capabilities of evaluating myocardial microstructure using DT-MRI and extend the achievements discussed in this dissertation.

REFERENCES

1. Edelman RR, Gaa J, Wedeen VJ, Loh E, Hare JM, Prasad P, Li W. In vivo measurement of water diffusion in the human heart. *Magn Reson Med*. 1994;32:423-428
2. Helm P, Beg MF, Miller MI, Winslow RL. Measuring and mapping cardiac fiber and laminar architecture using diffusion tensor mr imaging. *Ann N Y Acad Sci*. 2005;1047:296-307
3. Helm PA, Tseng HJ, Younes L, McVeigh ER, Winslow RL. Ex vivo 3d diffusion tensor imaging and quantification of cardiac laminar structure. *Magn Reson Med*. 2005;54:850-859
4. Holmes AA, Scollan DF, Winslow RL. Direct histological validation of diffusion tensor mri in formaldehyde-fixed myocardium. *Magn Reson Med*. 2000;44:157-161
5. Hsu EW, Muzikant AL, Matulevicius SA, Penland RC, Henriquez CS. Magnetic resonance myocardial fiber-orientation mapping with direct histological correlation. *Am J Physiol*. 1998;274:H1627-1634
6. Scollan DF, Holmes A, Winslow R, Forder J. Histological validation of myocardial microstructure obtained from diffusion tensor magnetic resonance imaging. *Am J Physiol*. 1998;275:H2308-2318
7. Scollan DF, Holmes A, Zhang J, Winslow RL. Reconstruction of cardiac ventricular geometry and fiber orientation using magnetic resonance imaging. *Ann Biomed Eng*. 2000;28:934-944
8. Kung G, Nguyen TC, Itoh A, Skare S, Ingels NB, Miller DC, Ennis DB. Diffusion tensor mri mapping of two local myocardial sheet orientations with histological validation. *Biomedical Engineering Society, Annual Meeting, Austin, TX [Abstract]*. 2010
9. Kung GL, Nguyen TC, Itoh A, Skare S, Ingels NB, Jr., Miller DC, Ennis DB. The presence of two local myocardial sheet populations confirmed by diffusion tensor mri and histological validation. *J Magn Reson Imaging*. 2011;34:1080-1091
10. Ennis DB, Kindlmann G. Orthogonal tensor invariants and the analysis of diffusion tensor magnetic resonance images. *Magn Reson Med*. 2006;55:136-146
11. Kajstura J, Zhang X, Liu Y, Szoke E, Cheng W, Olivetti G, Hintze TH, Anversa P. The cellular basis of pacing-induced dilated cardiomyopathy. Myocyte cell loss and myocyte cellular reactive hypertrophy. *Circulation*. 1995;92:2306-2317
12. Gerdes AM, Onodera T, Tamura T, Said S, Bohlmeyer TJ, Abraham WT, Bristow MR. New method to evaluate myocyte remodeling from formalin-fixed biopsy and autopsy material. *J Card Fail*. 1998;4:343-348
13. Moe GW, Armstrong P. Pacing-induced heart failure: A model to study the mechanism of disease progression and novel therapy in heart failure. *Cardiovasc Res*. 1999;42:591-599
14. Ellingson BM, Malkin MG, Rand SD, Connelly JM, Quinsey C, LaViolette PS, Bedekar DP, Schmainda KM. Validation of functional diffusion maps (fdms) as a biomarker for human glioma cellularity. *J Magn Reson Imaging*. 2010;31:538-548
15. Chen J, Song SK, Liu W, McLean M, Allen JS, Tan J, Wickline SA, Yu X. Remodeling of cardiac fiber structure after infarction in rats quantified with diffusion tensor mri. *Am J Physiol Heart Circ Physiol*. 2003;285:H946-954
16. Strijkers GJ, Bouts A, Blankesteijn WM, Peeters TH, Vilanova A, van Prooijen MC, Sanders HM, Heijman E, Nicolay K. Diffusion tensor imaging of left ventricular

remodeling in response to myocardial infarction in the mouse. *NMR Biomed*. 2009;22:182-190
17. Kanzaki Y, Yamauchi Y, Okabe M, Terasaki F, Ishizaka N. Three-dimensional architecture of cardiomyocytes and connective tissues in hypertrophic cardiomyopathy: A scanning electron microscopic observation. *Circulation*. 2012;125:738-739
18. Weber KT. Cardiac interstitium in health and disease: The fibrillar collagen network. *J Am Coll Cardiol*. 1989;13:1637-1652
19. Kellman P, Wilson JR, Xue H, Ugander M, Arai AE. Extracellular volume fraction mapping in the myocardium, part 1: Evaluation of an automated method. *J Cardiovasc Magn Reson*. 2012;14:63
20. Anderson RH, Smerup M, Sanchez-Quintana D, Loukas M, Lunkenheimer PP. The three-dimensional arrangement of the myocytes in the ventricular walls. *Clin Anat*. 2009;22:64-76
21. LeGrice IJ, Smaill BH, Chai LZ, Edgar SG, Gavin JB, Hunter PJ. Laminar structure of the heart: Ventricular myocyte arrangement and connective tissue architecture in the dog. *Am J Physiol*. 1995;269:H571-582
22. Costa KD, Takayama Y, McCulloch AD, Covell JW. Laminar fiber architecture and three-dimensional systolic mechanics in canine ventricular myocardium. *Am J Physiol*. 1999;276:H595-607
23. LeGrice IJ, Takayama Y, Covell JW. Transverse shear along myocardial cleavage planes provides a mechanism for normal systolic wall thickening. *Circ Res*. 1995;77:182-193
24. Cheng A, Nguyen TC, Malinowski M, Daughters GT, Miller DC, Ingels NB, Jr. Heterogeneity of left ventricular wall thickening mechanisms. *Circulation*. 2008;118:713-721
25. Harrington KB, Rodriguez F, Cheng A, Langer F, Ashikaga H, Daughters GT, Criscione JC, Ingels NB, Miller DC. Direct measurement of transmural laminar architecture in the anterolateral wall of the ovine left ventricle: New implications for wall thickening mechanics. *Am J Physiol Heart Circ Physiol*. 2005;288:H1324-1330
26. Arts T, Costa KD, Covell JW, McCulloch AD. Relating myocardial laminar architecture to shear strain and muscle fiber orientation. *Am J Physiol Heart Circ Physiol*. 2001;280:H2222-2229
27. Hooks DA, Trew ML, Caldwell BJ, Sands GB, LeGrice IJ, Smaill BH. Laminar arrangement of ventricular myocytes influences electrical behavior of the heart. *Circ Res*. 2007;101:e103-112
28. Hooks DA. Myocardial segment-specific model generation for simulating the electrical action of the heart. *Biomed Eng Online*. 2007;6:21
29. Pope AJ, Sands GB, Smaill BH, LeGrice IJ. Three-dimensional transmural organization of perimysial collagen in the heart. *Am J Physiol Heart Circ Physiol*. 2008;295:H1243-H1252
30. Cohn JN, Ferrari R, Sharpe N. Cardiac remodeling--concepts and clinical implications: A consensus paper from an international forum on cardiac remodeling. Behalf of an international forum on cardiac remodeling. *J Am Coll Cardiol*. 2000;35:569-582

31. Go AS, Mozaffarian D, Roger VL, Benjamin EJ, Berry JD, Borden WB, Bravata DM, Dai S, Ford ES, Fox CS, Franco S, Fullerton HJ, Gillespie C, Hailpern SM, Heit JA, Howard VJ, Huffman MD, Kissela BM, Kittner SJ, Lackland DT, Lichtman JH, Lisabeth LD, Magid D, Marcus GM, Marelli A, Matchar DB, McGuire DK, Mohler ER, Moy CS, Mussolino ME, Nichol G, Paynter NP, Schreiner PJ, Sorlie PD, Stein J, Turan TN, Virani SS, Wong ND, Woo D, Turner MB. Heart disease and stroke statistics--2013 update: A report from the american heart association. *Circulation*. 2013;127:e6-e245
32. Sutton MG, Sharpe N. Left ventricular remodeling after myocardial infarction: Pathophysiology and therapy. *Circulation*. 2000;101:2981-2988
33. Morita N, Sovari AA, Xie Y, Fishbein MC, Mandel WJ, Garfinkel A, Lin SF, Chen PS, Xie LH, Chen F, Qu Z, Weiss JN, Karagueuzian HS. Increased susceptibility of aged hearts to ventricular fibrillation during oxidative stress. *Am J Physiol Heart Circ Physiol*. 2009;297:H1594-1605
34. Tanaka K, Zlochiver S, Vikstrom KL, Yamazaki M, Moreno J, Klos M, Zaitsev AV, Vaidyanathan R, Auerbach DS, Landas S, Guiraudon G, Jalife J, Berenfeld O, Kalifa J. Spatial distribution of fibrosis governs fibrillation wave dynamics in the posterior left atrium during heart failure. *Circ Res*. 2007;101:839-847
35. Kang PM, Yue P, Izumo S. New insights into the role of apoptosis in cardiovascular disease. *Circ J*. 2002;66:1-9
36. Kehat I, Molkentin JD. Molecular pathways underlying cardiac remodeling during pathophysiological stimulation. *Circulation*. 2010;122:2727-2735
37. Ferrans VJ. Morphology of the heart in hypertrophy. *Hosp Pract (Off Ed)*. 1983;18:67-78
38. Anand IS, Liu D, Chugh SS, Prahash AJ, Gupta S, John R, Popescu F, Chandrashekhar Y. Isolated myocyte contractile function is normal in postinfarct remodeled rat heart with systolic dysfunction. *Circulation*. 1997;96:3974-3984
39. Burlew BS, Weber KT. Cardiac fibrosis as a cause of diastolic dysfunction. *Herz*. 2002;27:92-98
40. Hutchinson KR, Stewart JA, Jr., Lucchesi PA. Extracellular matrix remodeling during the progression of volume overload-induced heart failure. *J Mol Cell Cardiol*. 2010;48:564-569
41. Lin JM, Lai LP, Lin CS, Chou NK, Chiu CY, Lin JL. Left ventricular extracellular matrix remodeling in dogs with right ventricular apical pacing. *J Cardiovasc Electrophysiol*. 2010;21:1142-1149
42. Zhang S, Crow JA, Yang X, Chen J, Borazjani A, Mullins KB, Chen W, Cooper RC, McLaughlin RM, Liao J. The correlation of 3d dt-mri fiber disruption with structural and mechanical degeneration in porcine myocardium. *Ann Biomed Eng*. 2010;38:3084-3095
43. Anversa P, Loud AV, Levicky V, Guideri G. Left ventricular failure induced by myocardial infarction. I. Myocyte hypertrophy. *Am J Physiol*. 1985;248:H876-882
44. de Bakker JM, van Capelle FJ, Janse MJ, Wilde AA, Coronel R, Becker AE, Dingemans KP, van Hemel NM, Hauer RN. Reentry as a cause of ventricular tachycardia in patients with chronic ischemic heart disease: Electrophysiologic and anatomic correlation. *Circulation*. 1988;77:589-606

45. de Bakker JM, van Capelle FJ, Janse MJ, Tasseron S, Vermeulen JT, de Jonge N, Lahpor JR. Slow conduction in the infarcted human heart. 'Zigzag' course of activation. *Circulation*. 1993;88:915-926
46. Stork A, Lund GK, Muellerleile K, Bansmann PM, Nolte-Ernsting C, Kemper J, Begemann PG, Adam G. Characterization of the peri-infarction zone using t2-weighted mri and delayed-enhancement mri in patients with acute myocardial infarction. *Eur Radiol*. 2006;16:2350-2357
47. Bekkers SC, Yazdani SK, Virmani R, Waltenberger J. Microvascular obstruction: Underlying pathophysiology and clinical diagnosis. *J Am Coll Cardiol*. 2010;55:1649-1660
48. Anversa P, Beghi C, Kikkawa Y, Olivetti G. Myocardial infarction in rats. Infarct size, myocyte hypertrophy, and capillary growth. *Circ Res*. 1986;58:26-37
49. Marijianowski MM, Teeling P, Becker AE. Remodeling after myocardial infarction in humans is not associated with interstitial fibrosis of noninfarcted myocardium. *J Am Coll Cardiol*. 1997;30:76-82
50. Tournier JD, Mori S, Leemans A. Diffusion tensor imaging and beyond. *Magn Reson Med*. 2011;65:1532-1556
51. Stejskal EO, Tanner JE. Spin diffusion measurements: Spin echoes in the presence of a time-dependent field gradient. *Journal of Chemical Physics*. 1965;42:288-292
52. Moseley ME, Kucharczyk J, Mintorovitch J, Cohen Y, Kurhanewicz J, Derugin N, Asgari H, Norman D. Diffusion-weighted mr imaging of acute stroke: Correlation with t2-weighted and magnetic susceptibility-enhanced mr imaging in cats. *AJNR Am J Neuroradiol*. 1990;11:423-429
53. Ebisu T, Naruse S, Horikawa Y, Ueda S, Tanaka C, Uto M, Umeda M, Higuchi T. Discrimination between different types of white matter edema with diffusion-weighted mr imaging. *J Magn Reson Imaging*. 1993;3:863-868
54. Kono K, Inoue Y, Nakayama K, Shakudo M, Morino M, Ohata K, Wakasa K, Yamada R. The role of diffusion-weighted imaging in patients with brain tumors. *AJNR Am J Neuroradiol*. 2001;22:1081-1088
55. Sugahara T, Korogi Y, Kochi M, Ikushima I, Shigematu Y, Hirai T, Okuda T, Liang L, Ge Y, Komohara Y, Ushio Y, Takahashi M. Usefulness of diffusion-weighted mri with echo-planar technique in the evaluation of cellularity in gliomas. *J Magn Reson Imaging*. 1999;9:53-60
56. Basser PJ, Mattiello J, LeBihan D. Estimation of the effective self-diffusion tensor from the nmr spin echo. *J Magn Reson B*. 1994;103:247-254
57. Jones DK, Horsfield MA, Simmons A. Optimal strategies for measuring diffusion in anisotropic systems by magnetic resonance imaging. *Magn Reson Med*. 1999;42:515-525
58. Hasan KM, Parker DL, Alexander AL. Comparison of gradient encoding schemes for diffusion-tensor mri. *J Magn Reson Imaging*. 2001;13:769-780
59. Basser PJ, Mattiello J, LeBihan D. Mr diffusion tensor spectroscopy and imaging. *Biophys J*. 1994;66:259-267
60. Pierpaoli C, Basser PJ. Toward a quantitative assessment of diffusion anisotropy. *Magn Reson Med*. 1996;36:893-906
61. Basser PJ, Pajevic S, Pierpaoli C, Duda J, Aldroubi A. In vivo fiber tractography using dt-mri data. *Magn Reson Med*. 2000;44:625-632

62. Jones DK, Simmons A, Williams SC, Horsfield MA. Non-invasive assessment of axonal fiber connectivity in the human brain via diffusion tensor mri. *Magn Reson Med*. 1999;42:37-41
63. Poupon C, Mangin J, Clark CA, Frouin V, Regis J, Le Bihan D, Bloch I. Towards inference of human brain connectivity from mr diffusion tensor data. *Med Image Anal*. 2001;5:1-15
64. Mori S, Kaufmann WE, Pearlson GD, Crain BJ, Stieltjes B, Solaiyappan M, van Zijl PC. In vivo visualization of human neural pathways by magnetic resonance imaging. *Ann Neurol*. 2000;47:412-414
65. Kindlmann G. Superquadric tensor glyphs. *Proc IEEE TVCG/EG Symp Vis*. 2004:147-154
66. Ennis DB, Kindlman G, Rodriguez I, Helm PA, McVeigh ER. Visualization of tensor fields using superquadric glyphs. *Magn Reson Med*. 2005;53:169-176
67. Sands GB, Gerneke DA, Hooks DA, Green CR, Smaill BH, Legrice IJ. Automated imaging of extended tissue volumes using confocal microscopy. *Microsc Res Tech*. 2005;67:227-239
68. Roger VL, Go AS, Lloyd-Jones DM, Adams RJ, Berry JD, Brown TM, Carnethon MR, Dai S, de Simone G, Ford ES, Fox CS, Fullerton HJ, Gillespie C, Greenlund KJ, Hailpern SM, Heit JA, Ho PM, Howard VJ, Kissela BM, Kittner SJ, Lackland DT, Lichtman JH, Lisabeth LD, Makuc DM, Marcus GM, Marelli A, Matchar DB, McDermott MM, Meigs JB, Moy CS, Mozaffarian D, Mussolino ME, Nichol G, Paynter NP, Rosamond WD, Sorlie PD, Stafford RS, Turan TN, Turner MB, Wong ND, Wylie-Rosett J. Heart disease and stroke statistics--2011 update: A report from the american heart association. *Circulation*. 2011;123:e18-e209
69. Schelbert EB, Hsu LY, Anderson SA, Mohanty BD, Karim SM, Kellman P, Aletras AH, Arai AE. Late gadolinium-enhancement cardiac magnetic resonance identifies postinfarction myocardial fibrosis and the border zone at the near cellular level in ex vivo rat heart. *Circ Cardiovasc Imaging*. 2010;3:743-752
70. Karamitsos TD, Francis JM, Myerson S, Selvanayagam JB, Neubauer S. The role of cardiovascular magnetic resonance imaging in heart failure. *J Am Coll Cardiol*. 2009;54:1407-1424
71. Kim RJ, Wu E, Rafael A, Chen EL, Parker MA, Simonetti O, Klocke FJ, Bonow RO, Judd RM. The use of contrast-enhanced magnetic resonance imaging to identify reversible myocardial dysfunction. *N Engl J Med*. 2000;343:1445-1453
72. Wu EX, Wu Y, Nicholls JM, Wang J, Liao S, Zhu S, Lau CP, Tse HF. Mr diffusion tensor imaging study of postinfarct myocardium structural remodeling in a porcine model. *Magn Reson Med*. 2007;58:687-695
73. Wu Y, Zhang LJ, Zou C, Tse HF, Wu EX. Transmural heterogeneity of left ventricular myocardium remodeling in postinfarct porcine model revealed by mr diffusion tensor imaging. *J Magn Reson Imaging*. 2011;34:43-49
74. Li W, Lu M, Banerjee S, Zhong J, Ye A, Molter J, Yu X. Ex vivo diffusion tensor mri reflects microscopic structural remodeling associated with aging and disease progression in normal and cardiomyopathic syrian hamsters. *NMR Biomed*. 2009;22:819-825

75. O'Brien DW, Fu Y, Parker HR, Chan SY, Idikio H, Scott PG, Jugdutt BI. Differential morphometric and ultrastructural remodelling in the left atrium and left ventricle in rapid ventricular pacing-induced heart failure. *Can J Cardiol*. 2000;16:1411-1419
76. Gerdes AM, Moore JA, Hines JM, Kirkland PA, Bishop SP. Regional differences in myocyte size in normal rat heart. *Anat Rec*. 1986;215:420-426
77. Hoshino T, Fujiwara H, Kawai C, Hamashima Y. Myocardial fiber diameter and regional distribution in the ventricular wall of normal adult hearts, hypertensive hearts and hearts with hypertrophic cardiomyopathy. *Circulation*. 1983;67:1109-1116
78. Szafer A, Zhong J, Gore JC. Theoretical model for water diffusion in tissues. *Magn Reson Med*. 1995;33:697-712
79. Karger J. Nmr self-diffusion studies in heterogeneous systems. *Advances in Colloid and Interface Science*. 1985;23:129-148
80. Meier C, Dreher W, Leibfritz D. Diffusion in compartmental systems. I. A comparison of an analytical model with simulations. *Magn Reson Med*. 2003;50:500-509
81. Fieremans E, Novikov DS, Jensen JH, Helpern JA. Monte carlo study of a two-compartment exchange model of diffusion. *NMR Biomed*. 2010;23:711-724
82. Pfeuffer J, Flogel U, Dreher W, Leibfritz D. Restricted diffusion and exchange of intracellular water: Theoretical modelling and diffusion time dependence of 1h nmr measurements on perfused glial cells. *NMR Biomed*. 1998;11:19-31
83. Chen J, Liu W, Zhang H, Lacy L, Yang X, Song SK, Wickline SA, Yu X. Regional ventricular wall thickening reflects changes in cardiac fiber and sheet structure during contraction: Quantification with diffusion tensor mri. *Am J Physiol Heart Circ Physiol*. 2005;289:H1898-1907
84. Tseng WY, Wedeen VJ, Reese TG, Smith RN, Halpern EF. Diffusion tensor mri of myocardial fibers and sheets: Correspondence with visible cut-face texture. *J Magn Reson Imaging*. 2003;17:31-42
85. Ennis DB, Nguyen TC, Itoh A, Bothe W, Liang DH, Ingels NB, Miller DC. Reduced systolic torsion in chronic "pure" mitral regurgitation. *Circ Cardiovasc Imaging*. 2009;2:85-92
86. Nguyen TC, Itoh A, Carlhall CJ, Bothe W, Timek TA, Ennis DB, Oakes RA, Liang D, Daughters GT, Ingels NB, Jr., Miller DC. The effect of pure mitral regurgitation on mitral annular geometry and three-dimensional saddle shape. *J Thorac Cardiovasc Surg*. 2008;136:557-565
87. Skare S, Hedehus M, Moseley ME, Li TQ. Condition number as a measure of noise performance of diffusion tensor data acquisition schemes with mri. *J Magn Reson*. 2000;147:340-352
88. Ennis DB, Nguyen TC, Riboh JC, Wigstrom L, Harrington KB, Daughters GT, Ingels NB, Miller DC. Myofiber angle distributions in the ovine left ventricle do not conform to computationally optimized predictions. *J Biomech*. 2008;41:3219-3224
89. Ursell PC, Gardner PI, Albala A, Fenoglio JJ, Jr., Wit AL. Structural and electrophysiological changes in the epicardial border zone of canine myocardial infarcts during infarct healing. *Circ Res*. 1985;56:436-451
90. Miragoli M, Salvarani N, Rohr S. Myofibroblasts induce ectopic activity in cardiac tissue. *Circ Res*. 2007;101:755-758

91. Dillon SM, Allessie MA, Ursell PC, Wit AL. Influences of anisotropic tissue structure on reentrant circuits in the epicardial border zone of subacute canine infarcts. *Circ Res*. 1988;63:182-206
92. Kim RJ, Chen EL, Lima JA, Judd RM. Myocardial gd-dtpa kinetics determine mri contrast enhancement and reflect the extent and severity of myocardial injury after acute reperfused infarction. *Circulation*. 1996;94:3318-3326
93. Porter DA, Heidemann RM. High resolution diffusion-weighted imaging using readout-segmented echo-planar imaging, parallel imaging and a two-dimensional navigator-based reacquisition. *Magn Reson Imaging*. 2009;62:468-475
94. Ashikaga H, Sasano T, Dong J, Zviman MM, Evers R, Hopenfeld B, Castro V, Helm RH, Dickfeld T, Nazarian S, Donahue JK, Berger RD, Calkins H, Abraham MR, Marban E, Lardo AC, McVeigh ER, Halperin HR. Magnetic resonance-based anatomical analysis of scar-related ventricular tachycardia: Implications for catheter ablation. *Circ Res*. 2007;101:939-947
95. Tao Q, Milles J, Zeppenfeld K, Lamb HJ, Bax JJ, Reiber JHC, van der Geest RJ. Automated segmentation of myocardial scar in late enhancement mri using combined intensity and spatial information. *Magn Reson Imaging*. 2010;64:586-594
96. Gahm JG, Kung GL, Ennis DB. Weighted component-based tensor distance applied to graph-based segmentation of cardiac dt-mri. *International Symposium on Biomedical Imaging*. 2013;Accepted
97. Gahm JK, Wisniewski N, Kindlmann G, Kung GL, Klug WS, Garfinkel A, Ennis DB. Linear invariant tensor interpolation applied to cardiac diffusion tensor mri. *Med Image Comput Comput Assist Interv*. 2012;15:494-501
98. Lazic SE. The problem of pseudoreplication in neuroscientific studies: Is it affecting your analysis? *BMC Neurosci*. 2010;11:5
99. Marrouche NF, Verma A, Wazni O, Schweikert R, Martin DO, Saliba W, Kilicaslan F, Cummings J, Burkhardt JD, Bhargava M, Bash D, Brachmann J, Guenther J, Hao S, Beheiry S, Rossillo A, Raviele A, Themistoclakis S, Natale A. Mode of initiation and ablation of ventricular fibrillation storms in patients with ischemic cardiomyopathy. *J Am Coll Cardiol*. 2004;43:1715-1720
100. Marchlinski FE. Ventricular tachycardia ablation: Moving beyond treatment of last resort. *Circ Arrhythm Electrophysiol*. 2008;1:147-149
101. Verma A, Marrouche NF, Schweikert RA, Saliba W, Wazni O, Cummings J, Abdul-Karim A, Bhargava M, Burkhardt JD, Kilicaslan F, Martin DO, Natale A. Relationship between successful ablation sites and the scar border zone defined by substrate mapping for ventricular tachycardia post-myocardial infarction. *J Cardiovasc Electrophysiol*. 2005;16:465-471
102. Ashikaga H, Mickelsen SR, Ennis DB, Rodriguez I, Kellman P, Wen H, McVeigh ER. Electromechanical analysis of infarct border zone in chronic myocardial infarction. *Am J Physiol Heart Circ Physiol*. 2005;289:H1099-1105
103. Bogaert J, Bosmans H, Maes A, Suetens P, Marchal G, Rademakers FE. Remote myocardial dysfunction after acute anterior myocardial infarction: Impact of left ventricular shape on regional function: A magnetic resonance myocardial tagging study. *J Am Coll Cardiol*. 2000;35:1525-1534
104. Weisman HF, Bush DE, Mannisi JA, Bulkley BH. Global cardiac remodeling after acute myocardial infarction: A study in the rat model. *J Am Coll Cardiol*. 1985;5:1355-1362

105. Weisman HF, Bush DE, Mannisi JA, Weisfeldt ML, Healy B. Cellular mechanisms of myocardial infarct expansion. *Circulation*. 1988;78:186-201
106. Campbell SE, Gerdes AM, Smith TD. Comparison of regional differences in cardiac myocyte dimensions in rats, hamsters, and guinea pigs. *Anat Rec*. 1987;219:53-59
107. Kim S, Chi-Fishman G, Barnett AS, Pierpaoli C. Dependence on diffusion time of apparent diffusion tensor of ex vivo calf tongue and heart. *Magn Reson Med*. 2005;54:1387-1396
108. Hsu EW, Buckley DL, Bui JD, Blackband SJ, Forder JR. Two-component diffusion tensor mri of isolated perfused hearts. *Magn Reson Med*. 2001;45:1039-1045
109. Quirk JD, Bretthorst GL, Duong TQ, Snyder AZ, Springer CS, Jr., Ackerman JJ, Neil JJ. Equilibrium water exchange between the intra- and extracellular spaces of mammalian brain. *Magn Reson Med*. 2003;50:493-499
110. Vinnakota KC, Bassingthwaighte JB. Myocardial density and composition: A basis for calculating intracellular metabolite concentrations. *Am J Physiol Heart Circ Physiol*. 2004;286:H1742-1749
111. Gerdes AM. Cardiac myocyte remodeling in hypertrophy and progression to failure. *J Card Fail*. 2002;8:S264-268
112. Gerdes AM, Capasso JM. Structural remodeling and mechanical dysfunction of cardiac myocytes in heart failure. *J Mol Cell Cardiol*. 1995;27:849-856
113. Eble DM, Spinale FG. Contractile and cytoskeletal content, structure, and mrna levels with tachycardia-induced cardiomyopathy. *Am J Physiol*. 1995;268:H2426-2439
114. Tagawa H, Koide M, Sato H, Zile MR, Carabello BA, Cooper Gt. Cytoskeletal role in the transition from compensated to decompensated hypertrophy during adult canine left ventricular pressure overloading. *Circ Res*. 1998;82:751-761
115. Jiang Y, Guccione JM, Ratcliffe MB, Hsu EW. Transmural heterogeneity of diffusion anisotropy in the sheep myocardium characterized by mr diffusion tensor imaging. *Am J Physiol Heart Circ Physiol*. 2007;293:H2377-2384
116. Martinez DA, Guhl DJ, Stanley WC, Vailas AC. Extracellular matrix maturation in the left ventricle of normal and diabetic swine. *Diabetes Res Clin Pract*. 2003;59:1-9
117. Helm PA, Younes L, Beg MF, Ennis DB, Leclercq C, Faris OP, McVeigh E, Kass D, Miller MI, Winslow RL. Evidence of structural remodeling in the dyssynchronous failing heart. *Circ Res*. 2006;98:125-132